High energy x-ray implementation of phase contrast and dark field imaging

Ian Buchanan

Department of Medical Physics and Biomedical Engineering

UCL

A thesis submitted for the degree of

Doctor of Philosophy

October, 2019

I, Ian Buchanan, confirm that the work presented in this thesis is my own. Where information has been derived from other sources, I confirm that this has been indicated in the thesis.

Signed:

Abstract

X-ray phase contrast and dark field imaging are emerging imaging modalities which provide significantly enhanced visibility of details classically considered x-ray invisible and complementary information on a samples micro-structure, respectively. To date they have been successfully implemented in a series of applications at low x-ray energy, but their translation to higher x-ray energies is still, to some extent, problematic. Yet the ability to perform phase contrast and dark field imaging at high x-ray energy would have a series of significant implications in various applications, medical or otherwise. This thesis work investigates this option through a combination of modelling and experimental work. Particular attention has been dedicated to the behaviour of the optical elements (x-ray masks) that make phase contrast and dark field possible at high energy, which required the design of new methods of their implemention into simulation models. The modeling results have been validated first through a pilot experiment at a synchrotron facility, then in a series of lab experiments. Results clearly indicate that implementations of phase contrast and dark field imaging at high x-ray energy exist, however particular care must be taken in the design and fabrication of the masks; moreover, a series of parasitic effects which are absent at lower energies appear, which this thesis work describes and against which it suggests mitigation solutions.

Impact statement

Phase and dark field imaging reveal information about a sample's micro-structure, and thus have a variety of possible applications in clinical, pre-clinical and industrial settings. High energy x-rays are characterised by high penetration depths and by their low dose deposition to samples; phase and dark field imaging that utilise high energy x-rays would thus be an efficient tool for *in-vivo* experiments and applications, where dose is typically a concern. The x-ray phase contrast imaging (XPCi) technique of edge illumination (EI) is investigated here as a tool that may be operable in the high energy x-ray regime.

Results presented in this thesis demonstrate that possibilities for high energy implementations of XPCi using the EI technique exist; furthermore, if dose is a constraint, the energy may be tailored to produce the best possible signal to noise ratio. Parasitic effects, which become evident and in some ways problematic at high energy and for dark field imaging in particular, are described and verified through models of the experimental setup. The techniques for incorporating these effects into models are expected to be useful not only for EI, but also for grating interferometry, as the two methods make use of optical elements which are fabricated in similar ways. The results' implications are that new designs of optical components may be needed for these and for any similar techniques in the next generation of phase contrast methods.

Also, in collaboration with another scientist, a combination of models was also developed to rigorously model the dark field signal produced by different ensembles of spheres in an edge illumination system, which is expected to be especially useful for investigating the potential of the technique in more complex settings such as angiography, for example.

List of publications

I. Buchanan, A. Mittone, A. Bravin, P. C. Diemoz, M. Endrizzi, A. Olivo, Simplified retrieval method for Edge illumination X-ray phase contrast imaging allowing multi-modal imaging with fewer input frames, 2019, *Optics Express* (*in submission).*

I. Buchanan, M. Endrizzi, G. K. Kallon, J. Schulz, A. Olivo, Refinements for large field of view, high energy edge illumination X-ray phase contrast imaging models (*in preparation*)

Conference Papers

A. Olivo, F. A. Vittoria, P. Modregger, G. K. Kallon, L. Massimi, S. Savvidis, L. Brombal, G. Havariyoun, C. Maughan Jones, **I. Buchanan**, D. Shoukroun, P. R. T. Munro, C. K. Hagen, M. Endrizzi, Flexible solutions for lab-based phase contrast and dark field CT and micro-CT, *Industrial Computed Tomography 2019: New methods and optimisation*

Acknowledgements

My utmost respect and thanks go first to Professor Alessandro Olivo for the opportunity and support he has provided in this PhD project. His ability to teach while leading, lift spirits while laughing, and above all his unending patience with myself and the trials of academic research are inspiring and humbling in equal measure.

I would also like to thank my second and third supervisors, Dr. Marco Endrizzi, for sharing his practical genius in the lab and for many calming and enlightening discussions, and Dr Thomas Weber, for his support and continuous interest in the project. Drs. Fabio Vittoria and Thomas Millard, too, for introducing me to the simulation tools they created and always making themselves available to discuss the physics and code with enthusiasm.

For their time, expertise and generous engagement with my work, I send heartfelt thanks to Drs. Joachim Schulz, Peter Munro, Sally Irvine and Peter Modregger, the last of whom I hope is satisfied with my derivation of x-ray refraction angles.

Much of the work and conclusions of this thesis would not have been possible without the work of scientists at both the ESRF and Diamond synchrotrons, some of whom I have never met in person, but to whom I nevertheless send my appreciation. In the same vein, I am grateful to all the members of the Advanced X-ray Imaging group at UCL for the wide range of enjoyable and thought-provoking discussions, and for all the small collaborations that take place on a daily basis in our office.

As much as this PhD has been an academic work, these four years

have been marked by the makings of many precious friends. In particular, Dr. Gibril Kallon, who shared knowledge, encouragement, highs and lows, all in an endless loop: thank you and Mariama both for your teachings and friendship. Kaat De Corte, Dr. Ben Williamson, Matt Barker, Jörg Elmers and more, whom I met through song in the University of London Chamber Choir. Logan Forth and Dr. Charlotte Maughan-Jones, who shared in the PhD journey from the very beginning. The fun and friendly scientists in the Medical Physics Department, too numerous to name, who socialise morning, noon and night. My housemates and friends whom have consistently supported me and introduced me to the joys of good coffee. To you all, I send my love and gratitude.

Lastly, to my family. My brother, sister and I have spread far from home, but remain close together and with our parents; thanks to you, I am grounded in several lands, all at once.

Contents

List of Figures

List of Tables

Introduction

The use of x-rays in imaging is widespread, as the technology it requires is relatively cheap and the physics of their interactions with matter is well understood. A typical method of predicting image contrast, or the distinguishability of different features, is to compare differences in atomic number, as a proxy for electron density, for different materials - the greater the difference, the greater the contrast. High energy x-rays, or *hard* x-rays, are desirable in imaging for two reasons: they have a high penetration depth, and they interact more weakly with matter than low energy ones. These properties mean that hard x-rays can be used to examine internal structures of thick or dense samples, and that - per photon and depending on the application - they deposit a comparably lower amount of dose to a sample. As x-rays are a form of ionising radiation, capable of causing harm to living tissue such as cells, the latter implication is particularly desirable in clinical and pre-clinical imaging.

The difficulty in using hard x-rays is that, as a result of interacting only weakly with matter, the efficiency of x-ray detectors, and the contrast between materials, decreases. X-ray phase contrast imaging (XPCi) is an advanced imaging technique that generates contrast from x-ray refraction, not attenuation, in particular: the outlines of materials - even those that are weakly absorbing - are enhanced, thus increasing the overall visibility. Dark field imaging is an extension of this phase sensitivity and refers to multiple refractions on a scale smaller than the resolution of the imaging system. These signals are usually generated by micro-structures of a material, with the signal being detected either directly, or inferred through multiple measurements. As is the case for conventional x-ray imaging, the ability to distinguish different materials is affected by their difference in electron density. However in phase-enhanced images, this difference need not be as large as in absorption-based techniques.

In recent years, much research has been dedicated to combining phase-enhancement techniques with hard x-rays. The technical challenges of this apply to all of the components of the imaging system including the source, which is ideally small and bright, any optical elements in play and the detector. Some XPCi techniques rely on very small, coherent sources, with only synchrotrons - huge facilities with power consumption being measured in Mega Watts - being capable of supplying this in addition to high photon flux. Microfocal sources, which can be operated on smaller scales, exist, but exposure times can be long due to their inherently low flux. The optical elements used in some XPCi methods are also usually wavelength specific, hence if used in polychromatic settings, their performance may suffer as a result. Edge illumination (EI) is an XPCi technique that imposes low coherence requirements on the source and is achromatic, whereby the individual photon wavelengths used are not intrinsically "weighted" by the system.

The work of this thesis aims to discern what limitations, if any, apply to the EI system parameters when using increasingly hard x-rays in a laboratory setting. An overview of x-ray production, interaction with matter and ultimately detection, are given in chapter one, followed by a description of various XPCi methods in chapter two. The third chapter presents experimental data collected at the European Synchrotron Radiation Facility (ESRF), where high energy x-rays were used to investigate the dark field signals produced by different concentrations of microspheres. In the fourth chapter, I discuss similar experiments undertaken in a laboratory here at UCL, and describe the simulation tools that are used to understand the system outputs. The fifth chapter is focussed on understanding the significance of previously neglected physical processes in EI, which become non-negligible in high-energy settings, and how they may be incorporated into existing models. A combination of the refined model is then used in conjunction with a rigorous wave optics simulation tool for ensembles of spheres in order to demonstrate the flexibility and accuracy of the model for complex scattering samples.

1

Introduction to x-ray imaging

In this chapter x-rays are defined, their interactions with matter explained and the principles of x-ray imaging explored. While these concepts underpin all of x-ray imaging, particular attention is given to the physics underlying XPCi. Finally, a general overview of dose deposited by x-rays, and ways in which this can be quantified and discussed are given.

1.1 Discovery of x-rays

Physically, most humans are equipped with the ability to detect and differentiate parts of the electromagnetic spectrum, namely that of visible light. Photons in this range have a wavelength typically measured in hundreds of nanometres; sodium fluorescence light, the yellow historically seen in street lamps, have a wavelength around 589 nm. Radio waves exist at the low-energy end of the spectrum, having wavelengths measured in metres, while gamma rays, at the very top end, have wavelengths on the scale of atomic nuclei (femtometres, 10^{-15} m). The x-ray regime encapsulates photons of higher energy than visible and ultraviolet light, but lower than gamma rays; their wavelengths are comparable to the atomic *radius* and are thus typically measured in angstroms, Å$= 10^{-10}$ m. Since x-rays span a very wide range of wavelengths, it is often simpler to discuss them in terms of their energies, which range from 100 electron volts (eV) at the low end, to an upper limit of several hundreds of keV. The wavelength λ is related to the energy E, measured in electron Volts (eV), by the equation:

$$E = \frac{hc}{1.602 \times 10^{-19} \lambda}, \tag{1.1}$$

where $h = 6.626 \times 10^{-34}$ m^2 kg/s is the Planck constant, and $c = 3 \times 10^8$ m/s is the speed of light. As an example, a 10 keV photon has a wavelength of 1.24 Å.

Wilhelm Roentgen was working with a partially evacuated cathode ray tube in 1895, with a fortuitously placed fluorescent screen located some distance away, when he discovered x-rays. The glass tubing housed a negatively charged cathode - a heated filament - which spewed electrons toward the anode - a positively charged metallic target. Upon contact with the anode, electrons were rapidly decelerated, transferring a proportion of their kinetic energy into a burst of electromagnetic radiation: x-rays. This "braking" radiation, referred to as *Bremsstrahlung* radiation, has an energy range of $0 < E \leq E_{\text{electron}}$, where E_{electron} is the kinetic energy of the electron.

When Roentgen saw the screen fluorescing, he deduced the existence of x-rays as a form of penetrating radiation and, through experimentation, began to understand how this penetrative capability varied according to different objects being placed between the tube and screen. Paper, wood, aluminium and even copper failed to completely stop the radiation, while a lead coated sheet of glass succeeded. Eventually, Roentgen placed a photographic plate in place of the screen and made the first x-ray images of his wife's hand. This was the first, and to date the most common, implementation of attenuation based x-ray imaging.

Upon publication in late 1895, Roentgen and the scientific community in general launched a genre of research that would profoundly affect the field of medicine. The ability to non-invasively "see" inside a patient unlocked such a torrent of diagnostic potential that, within 5 years, it was widely considered to be "a useful tool", and by the 1930's, x-ray machines were key features of hospitals [1]. Beyond healthcare, however, x-rays have also found uses in a variety of scientific and engineering fields, ranging from bio-mechanical observations to security applications. To this end, the technology for producing and detecting x-rays has developed considerably from partially evacuated cathode ray tubes and photographic plates, though in many cases the principle remains the same.

1.2 X-ray production

Most parts of the electromagnetic spectrum result from electrons undergoing changes in velocity, with gamma rays, which are produced by atomic nuclei, being an obvious exception. There are several mechanisms we can use to accelerate or decelerate electrons, and the one we choose is generally a function of what is required of the x-rays. With an understanding of the different sources available, it is possible to choose one suited to a given purpose by identifying and comparing their respective strengths and weaknesses.

1.2.1 X-ray tubes

Bremsstrahlung radiation, as mentioned above, is the braking radiation of an electron being rapidly decelerated; it is the primary mechanism for x-ray production in x-ray tubes. Based on the cathode ray tube, electrons are emitted from a heated filament and are accelerated by the potential difference, or Voltage (typically in the kV range), from cathode to anode. The anode is a metal plate of high atomic number and melting point (e.g. tungsten, molybdenum, copper), and is

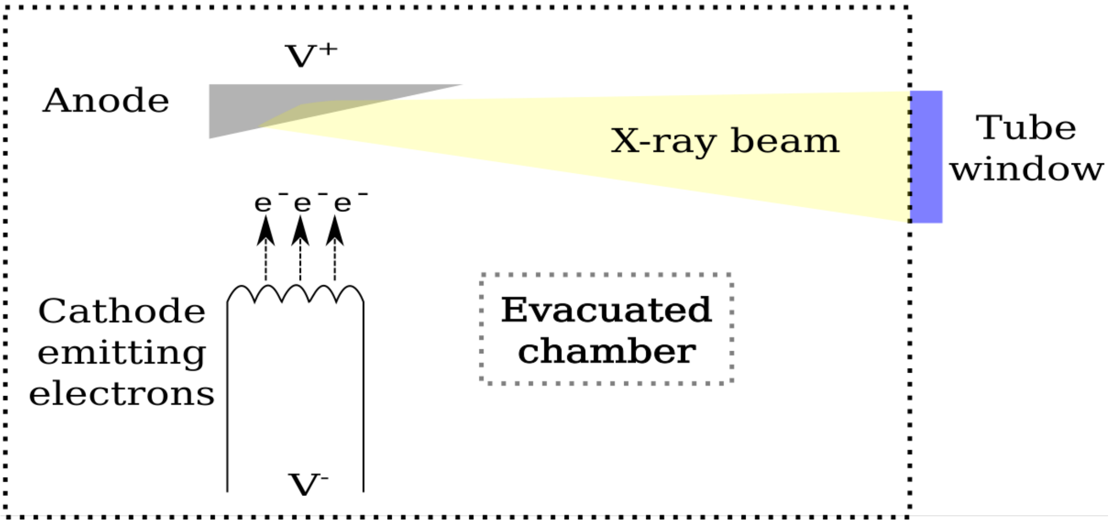

Figure 1.1: Schematic of an x-ray tube with rotating anode target.

the "source" of x-rays, as depicted in Fig. 1.1. Fewer than 1% of incident electrons actually emit x-ray photons, with most of their kinetic energy instead escaping as heat. Rotating anodes, which spread the waste heat energy generated by the electron beam over a larger area, are often used to allow higher intensity electron beams, and thus flux of photons, to be produced [2].

In addition to Bremsstrahlung radiation, which describes a continuous spread of photon energies up to the maximum electron energy, Fig. 1.2 shows how x-rays are also generated through characteristic line emission. In this case, an incident electron interacts with, and causes the ejection of, one of an atom's inner shell electrons. From the nucleus moving outwards, the orbitals are labelled as K, L, M, N (etc.) shells, with each one corresponding to increments of the principal quantum number of an electron in a potential well; these are further subdivided according to the azimuthal, magnetic and spin quantum numbers. In order to eject an electron from one of these orbitals, or to *ionise* the atom, the incident electron's energy must be greater than the *work function* or *binding energy* of the shell. Once ejected from the atom, an electron from one of the higher energy levels decays into the vacated orbital and emits an x-ray photon of energy $E_\gamma = E_{\mathrm{K,L,M:1}} - E_{\mathrm{K,L,M:2}}$

in the process. As energy levels are sub-divided by several quantum numbers, transitions may occur for a variety of different energy gaps which also contribute to characteristic emission lines, as illustrated in Fig. 1.2 (c). Energy level differences are characteristic of the atoms in which they occur, and are seen in x-ray spectra as sudden peaks of spectral intensity. In terms of the x-ray beam, these increases in intensity both increase the overall flux and change the mean energy that would otherwise be determined solely through the Bremsstrahlung mechanism.

A technical constraint of x-ray tubes is often the overall power input, whereby the product of tube voltage and current usually has an upper limit. The value of this limit depends primarily on the melting temperature of the anode, and is thus a “hard” limit on the flux that can be produced by an x-ray tube. The maximum photon energy is determined by the accelerating voltage, which can be very high if the current is sufficiently reduced, though in doing so, the flux decreases proportionally. A compromise between having a high *mean energy* in combination with appreciable flux is usually sought, and can be achieved indirectly via *filtering*. In the context of x-rays, filtering usually means placing some known material, which strongly attenuates the lower-energy sections of the beam, and only weakly the higher-energy sections, in the beam path. This reduces the overall flux, but can be useful for lowering the beam’s dose-rate and is routinely used in clinical practice.

A useful quantity to consider when measuring the output of an x-ray source is the *Brilliance*, as defined by:

$$\text{Brilliance} = \frac{N_{\text{ph}}}{\text{sec} \cdot \text{mrad}^2 \cdot \text{mm}^2 \cdot 0.1\%\text{BW}}, \tag{1.2}$$

which is an expression of the flux, or number of photons (N_{ph}), per units time (seconds), solid angle (mrad^2) source area (mm^2) and energy bandwidth of 0.1%. For Bremsstrahlung radiation in a fixed or rotating anode source, the peak bril-

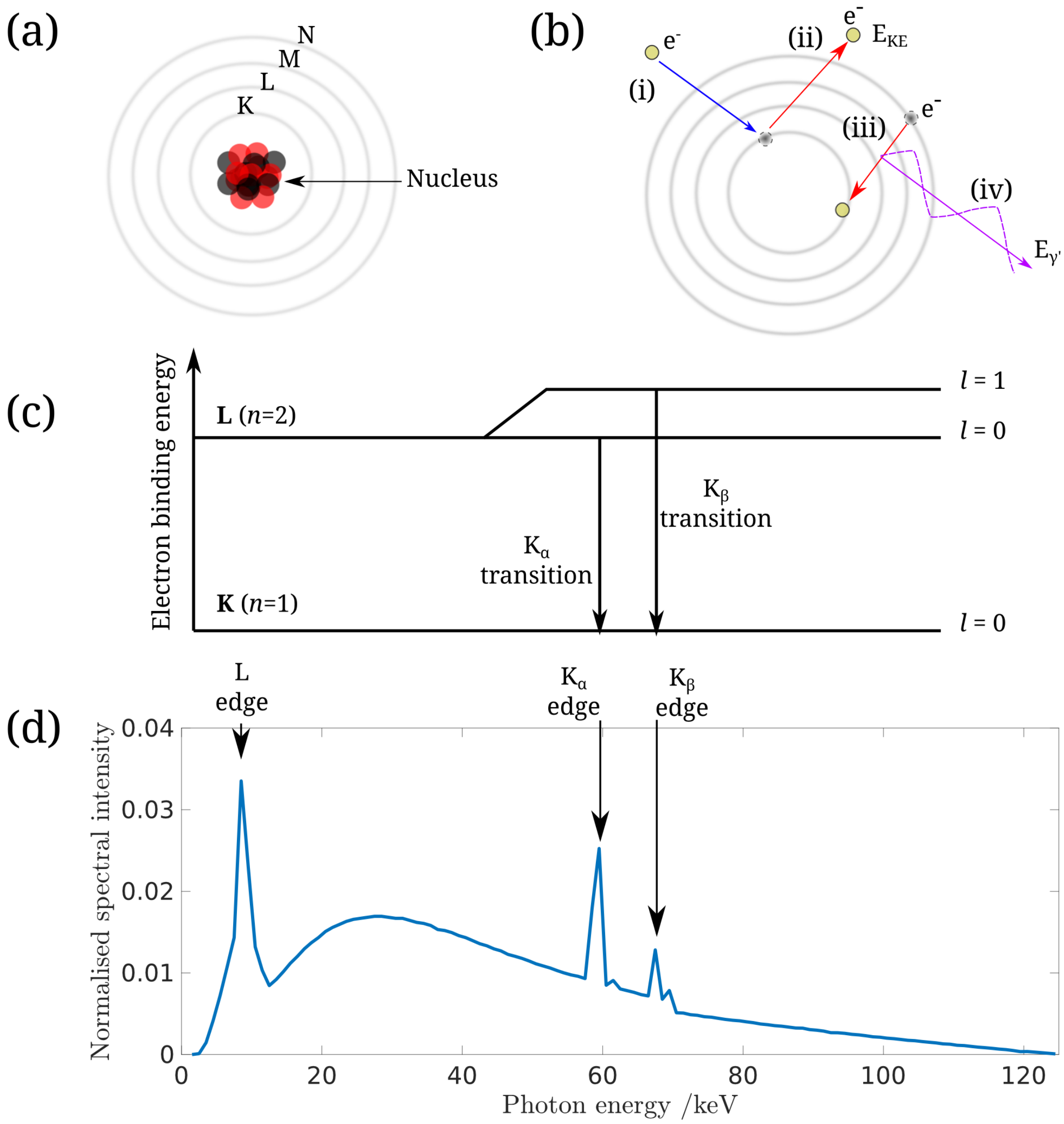

Figure 1.2: Illustration of electron-ionisation and characteristic line emission. (a) is a simplified model of an atom with labelled orbital shells; (b) shows the process of characteristic photon emission: (i) an electron is incident on the atom, (ii) an inner shell electron is emitted with some kinetic energy, (iii) an outer shell electron fills the vacant low-energy orbital, (iv) a characteristic x-ray photon is emitted. (c) shows an energy level diagram of an atom, with the possible transitions from the L to K shells marked; n and l refer to the principal and azimuthal quantum numbers, respectively. (d) shows an example tungsten spectrum for an accelerating tube voltage of 125 kVp, with the characteristic line emissions indicated.

liance achievable is on the order of 10^5-10^6 photons s^{-1} mm^{-2} mrad^{-2} per 0.1% bandwidth, while for characteristic lines, it is typically two to three orders of magnitude greater. If an experiment or measurement requires source brilliances much greater than this, synchrotrons are usually required.

1.2.2 Synchrotron sources

Synchrotrons are capable of delivering monochromatic and polychromatic x-ray beams with orders of magnitude more flux than x-ray tube sources [3]. These facilities are roughly circular with a radius measured in kilometres. Electrons are accelerated to relativistic speeds by high voltage electric fields, while bending electromagnets, interspersed along the circular path, are used to confine them within the storage ring. An electron traversing these magnetic fields experiences a force acting perpendicular to their direction of travel, as described by the Lorentz equation:

$$\mathbf{F} = e(\mathbf{E} + \boldsymbol{v} \wedge \mathbf{B}), \tag{1.3}$$

where $\mathbf{E}$, $\mathbf{B}$ are the electronic and magnetic fields, $\boldsymbol{v}$ is the electron velocity and $\wedge$ indicates the vector cross product. Magnetic fields do no work on charged particles, instead they cause the particles to change direction, during which photons are emitted into some solid angle. For relativistic electrons (E $\gg$ 511 keV) moving in a circular trajectory of radius R, Schwinger's formula expresses the radiated power as:

$$P = \frac{2}{3}\frac{e^2 c}{R^2}\gamma^4; \tag{1.4}$$

and the beam's angular distribution is strongly collimated in the direction of $\hat{\boldsymbol{v}}$, confined within a cone whose half-angle is given in radians by

$$\alpha \approx \frac{1}{\gamma}, \tag{1.5}$$

where $\gamma \equiv 1/\sqrt{1-\frac{v^2}{c^2}}$ is the Lorentz factor and c is the speed of light in vacuum. As an example, if electrons have been accelerated to energies in the GeV range, which is typical in synchrotrons, the cone angle is measured in milliradians, meaning the beam is narrow and, due to the very small area of emittance, highly spatially coherent, i.e. each point on the wavefront produced is moving in phase.

Bending magnets are useful both in terms of electron confinement and as x-ray sources, with peak brilliances of 10^{15} photons s^{-1} mm^{-2} mrad^{-2} per 0.1% bandwidth. A more efficient approach to generating x-rays, however, is to insert sets of magnetic dipoles or multipoles into the straight sections of a storage ring. These devices are known as wigglers or undulators, depending on the degree of overlap between the cones of radiation they produce, and are illustrated in Fig. 1.3.

Wigglers, a product of second generation synchrotrons, with peak brilliances one-to-two orders of magnitude greater than those of bending magnets, emit multiple cones of radiation at a range of angles. Dipole magnets cause the electron beam to be deviated back and forth, with cones of synchrotron radiation emitted during each “wiggle”. With N periods of magnetic dipoles / multipoles, the intensity output from a wiggler increases proportionally to $2N$, as individual emissions add together linearly and interference between beams is negligible. Undulators, which provide the greatest brilliance of the sources listed here - up to 10^{19} photons s^{-1} mm^{-2} mrad^{-2} per 0.1% bandwidth - are of third generation synchrotrons and produce confined x-ray beams within very narrow emission cones. The intensity of x-rays produced by an undulator varies according to N^2, as here, photons are emitted into solid angles being $\leq \alpha$ and furthermore, the beams are emitted in phase and thus interfere constructively when viewed at certain angles.

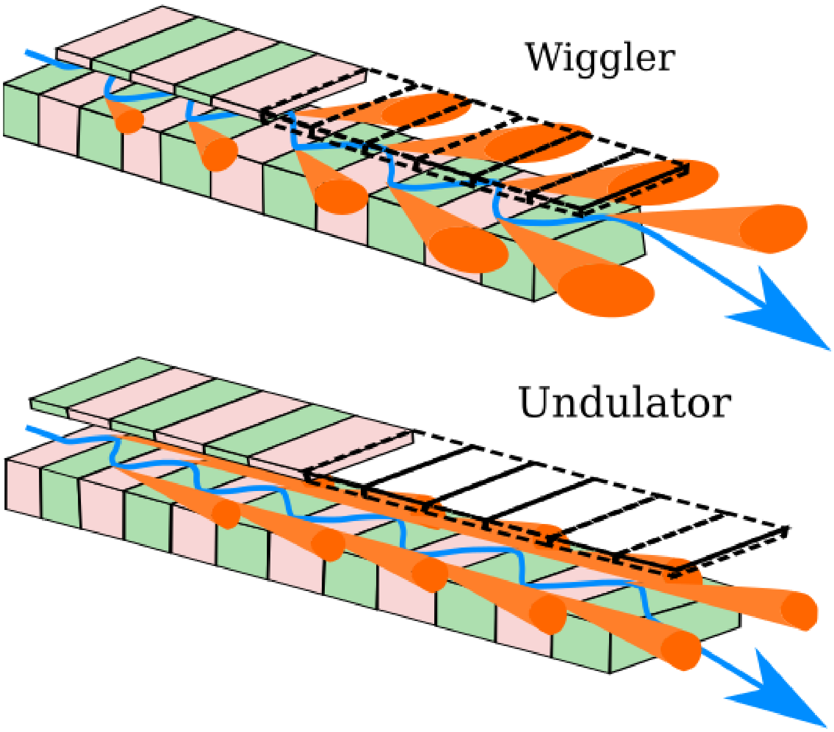

Figure 1.3: Conceptual structure of a the wiggler and undulator sources used in synchrotrons. Alternating magnetic dipoles cause the electron beam to deflect along sinusoidal trajectories, emitting synchrotron radiation during each acceleration.

1.3 X-ray propagation and interaction with electrons

As x-rays are electromagnetic waves, their evolution in free space is described by Maxwell's equations, listed below for the case of there being no local charges or currents:

$$\nabla \cdot \boldsymbol{E}(x, y, z, t) = 0; \tag{1.6}$$

$$\nabla \cdot \boldsymbol{B}(x, y, z, t) = 0; \tag{1.7}$$

$$\nabla \times \boldsymbol{E}(x, y, z, t) = -\frac{\partial}{\partial t}\boldsymbol{B}(x, y, z, t); \tag{1.8}$$

$$\nabla \times \boldsymbol{B}(x, y, z, t) = \epsilon_0 \mu_0 \frac{\partial}{\partial t}\boldsymbol{E}(x, y, z, t). \tag{1.9}$$

ϵ_0 is the electrical permittivity in vacuum, μ_0 the magnetic permeability in vacuum, (x, y, z) the Cartesian coordinates, t is time and $\frac{\partial}{\partial t}$ is the partial derivative with respect to time.

By applying the curl operator to Eq. 1.8, and simplifying the resulting expression with the identity $\nabla \times (\nabla \times \boldsymbol{A}) = \nabla(\nabla \cdot \boldsymbol{A}) - \nabla^2 \boldsymbol{A}$, and using substitutions from Eqs. 1.6 and 1.9, one obtains the well known wave equations for the electric and magnetic fields:

$$\big(\epsilon_0\mu_0\frac{\partial^2}{\partial t^2} - \nabla^2\big)\boldsymbol{E}(x, y, z, t) = 0; \tag{1.10}$$

$$\big(\epsilon_0\mu_0\frac{\partial^2}{\partial t^2} - \nabla^2\big)\boldsymbol{B}(x, y, z, t) = 0. \tag{1.11}$$

These are the d'Alembert equations, describing waves propagating at speed $c = 1/\sqrt{\epsilon_0\mu_0}$. From Eqs. 1.8 and 1.9, we can see that these two waves oscillate perpendicular to one another, and since $|\boldsymbol{B}| \ll |\boldsymbol{E}|$, we neglect it and only consider the $\mathbf{E}$ field.

A general plane wave solution for a wave denoted as ψ, of wavelength λ, is:

$$\psi = \psi_0 e^{-i(\mathbf{k}\cdot\mathbf{r} - \omega t + \phi)}, \tag{1.12}$$

where $|\mathbf{k}| = 2\pi/\lambda$ is the wavevector describing the propagation direction, $\mathbf{r}$ is the (x, y, z) coordinate system, $\omega = 2\pi c/\lambda$ is the angular frequency and ϕ is a constant phase term. By the principle of superposition, *any* waveform may also be described by a linear combination of plane waves that satisfy $k^2 = k_x^2 + k_y^2 + k_z^2$, where $k_{x,y,z}^2$ are the vector components of $\mathbf{k}$ and $k = \omega/c$ is the wavenumber.

In general, one assumes knowledge of a wavefront at a fixed starting position, $z = 0$, and seeks to understand how that wavefront behaves as the wave propagates in the z direction. There are two equivalent approaches to determine the outcome if the *paraxial approximation* ($\sqrt{k^2 - k_x^2 - k_y^2} \approx k - \frac{k_x^2+k_y^2}{2k}$) is valid, i.e. we assume that the wave propagates almost entirely in the z direction. The first is the Helmoltz propagator -

$$H_z(x,y) = \frac{e^{ikz}}{i\lambda z} \exp\big[\frac{ik}{2z}(x^2+y^2)\big], \tag{1.13}$$

which acts upon the known wavefront, $\psi_\omega(x,y,z=0)$ via the convolution operator, $*$, as:

$$\psi_\omega(x,y,z) = \psi_\omega(x,y,0) * H_z(x,y), \tag{1.14}$$

or, explicitly via the convolution theorem:

$$\psi_\omega(x,y,z) = e^{ikz}\mathcal{F}^{-1}\big\{[\mathcal{F}\psi_\omega(x,y,0)] \exp\big(-iz\frac{k_x^2+k_y^2}{2k}\big)\big\}, \tag{1.15}$$

with $\mathcal{F}$ and $\mathcal{F}^{-1}$ denoting the two-dimensional Fourier transform and its inverse, respectively. It can be demonstrated with the above equation that, given a plane wave in vacuum, this will remain a plane wave after propagating for some distance. The propagator itself is very useful, as it allows us to calculate wavefronts for any z (in the paraxial approximation) by a sequence of Fourier transforms which are computationally efficient functions.

The second way of determining an evolved wavefront is via the transport-of-intensity equation (TIE) [4]. As the name implies, this formulation is primarily concerned with the propagation of *intensity*, rather than the full wavefront description. As intensity is the property that is ultimately measured, however, this is a useful result. To derive the TIE, we begin by expressing $\psi_\omega(x,y,z)$ in terms of its intensity, $I(x,y,z) \equiv |\psi(x,y,z)|^2$ (we have dropped the explicit dependence

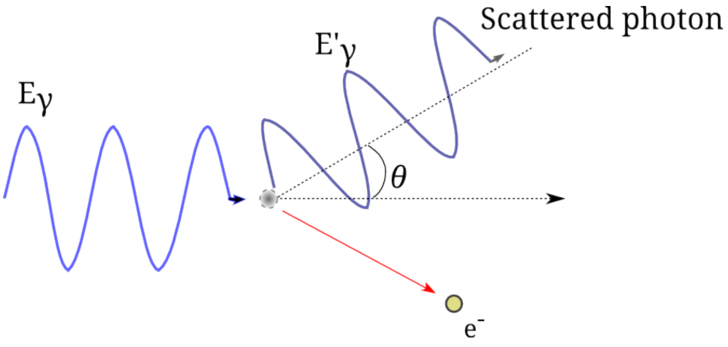

Figure 1.4: Compton scattering: the incident photon of energy E_γ interacts with a stationary electron and is scattered through an angle θ and has a reduced energy E'_γ.

on angular frequency ω), and the phase as $\phi(x, y, z) = \text{Im}(\psi(x, y, z))$, i.e.

$$\psi(x, y, z) = \sqrt{I(x, y, z)} \exp\left[i\phi(x, y, z)\right]. \tag{1.16}$$

By again making the paraxial approximation within Maxwell's equations, we can separate the real and imaginary components of these equations to arrive at the TIE:

$$\nabla_\perp \cdot [I(x, y, z)\nabla_\perp \phi(x, y, z)] = -k\frac{\partial I(x, y, z)}{\partial z}, \tag{1.17}$$

where $\nabla_\perp = (\frac{\partial}{\partial x}, \frac{\partial}{\partial y})$ is the two-dimensional gradient operator.

In this thesis, the Helmholtz propagator is the primary method used in determining the evolution of complex waveforms.

Let us now consider how an x-ray photon interacts with a free electron. The situation is expressed in Fig. 1.4, in which a photon of energy E_γ interacts with an approximately stationary electron, and is then scattered through an angle θ. By conservation of four-energy and four-momentum, we can determine the energy of the scattered photon, E'_γ, after this event as a function of θ. First, we isolate an expression for the electron momentum after the interaction in terms of photon energies:

$$P_e^2 = (P_\gamma - P'_\gamma)^2; \tag{1.18}$$

$$P_e^2 = P_\gamma^2 + P'^2_\gamma - 2P_\gamma P'_\gamma \cos\theta; \tag{1.19}$$

$$P_e^2 c^2 = E_\gamma^2 + E'^2_\gamma - 2E_\gamma E'_\gamma \cos\theta, \tag{1.20}$$

where we have begun by squaring the conservation of momentum expression and ended by multiplying both sides by c^2 in order to express momentum in terms of energy. Next, we consider the conservation of energy:

$$E_\gamma + m_0 c^2 = E'_\gamma + \sqrt{P_e^2 + (m_0 c^2)^2}; \tag{1.21}$$

$$P_e^2 c^2 = (E_\gamma - E'_\gamma + m_0 c^2)^2 - (m_0 c^2)^2, \tag{1.22}$$

where m_0 is the rest mass of the electron. Now, by substituting Eq. 1.22 into 1.20 and rearranging, we obtain

$$E'_\gamma = \frac{E_\gamma}{1 + \frac{E_\gamma}{m_0 c^2}(1 - \cos\theta)}, \tag{1.23}$$

or, in terms of wavelength:

$$\Delta\lambda = \frac{h}{m_0 c}\big(1 - \cos\theta\big). \tag{1.24}$$

This result is known as *Compton scattering*, and is applicable not only to free electrons, but also to weakly bound electrons in outer atomic shells, which are often considered to be “free” in the case where E_γ is much greater than the binding energy of the electron. In the special case of $\Delta\lambda \approx 0$, the electron oscillates in phase with the incident wave, absorbing and rapidly re-emitting the photon at the same frequency; this is coherent, or *Thomson*, scattering, which predominantly occurs for lower energy photons.

The cross section of scattering interactions for a given material may be obtained by measuring the ratios of incident and scattered radiation. For Compton scattering, this is a function of material density, ρ and photon energy:

$$\sigma_{\text{Compton}} \propto \frac{\rho}{E}. \tag{1.25}$$

If, instead of interacting with an atomic outer-shell electron, an x-ray photon interacts with an inner-shell electron, the *photoelectric effect* may occur. Referring to Fig. 1.2 (b), the photoelectric effect is a result of a photon, rather than an electron, ionising an atom by removal of an inner shell electron. This occurs if the energy of the photon is greater than the work function, and after ionisation, an electron from one of the outer shells transitions to fill the vacated orbital. As is the case for characteristic line emission, a photon whose energy is equal to the difference in atomic energy levels is emitted in the process. The photoelectric cross-section varies approximately with the atomic number, Z, and the photon energy as:

$$\sigma_{\text{pe}} \propto \frac{Z^3}{E^3}. \tag{1.26}$$

This breaks down, however, near the absorption edges, where the cross-section increases significantly due to the sudden expansion of the probability space.

In low-density materials such as soft tissues, the photoelectric effect is dominant for photons up to energies of about 30 keV, above which Compton scattering begins to dominate. For higher Z materials, the energy range where this transition occurs is higher.

1.4 X-ray interactions with bulk materials

With an understanding of how x-rays interact with isolated and partially-bound electrons, we may now expand to consider how they interact with an ensemble of atoms and molecules. For a homogeneous material with dielectric constant $\epsilon = \epsilon_r \epsilon_0$, and magnetic permeability $\mu = \mu_r \mu_0$, where ϵ_r and μ_r are the relative dielectric and magnetic permeability constants respectively, the wave equations 1.10 and 1.11 become:

$$(\epsilon\mu\frac{\partial^2}{\partial t^2} - \nabla^2)\mathbf{E}(x, y, z, t) = 0; \tag{1.27}$$

$$(\epsilon\mu\frac{\partial^2}{\partial t^2} - \nabla^2)\mathbf{B}(x, y, z, t) = 0. \tag{1.28}$$

Hereafter, we make the (usually valid) assumption that the wave is not propagating in a magnetic material, hence $\mu_r = 1$. In the above case, we see the wave speed has been reduced by $\sqrt{\epsilon_r}$, so the wave propagates at speed $v = c/\sqrt{\epsilon_r} = c/n$; n is the refractive index, or ratio of the speed of light in vacuum to that inside a dielectric medium. As photon-electron interactions are affected by the photon energy, the refractive index is a function of photon energy also. In terms of the wavenumber, k, it satisfies the *dispersion relation*:

$$k^2 = \frac{\omega^2 n^2}{c^2}. \tag{1.29}$$

With this, our plane wave solution from Eq. 1.12 must be updated to represent the new spatial dependence:

$$\psi = \psi_0 e^{-i\omega(\frac{n}{c}\hat{\boldsymbol{k}}\cdot\mathbf{r} - t)}, \tag{1.30}$$

where we have included the arbitrary phase factor within ψ_0.

In general, n is a complex quantity, with modulus very close to one, and is expressed by:

$$n(\omega) = 1 - \delta(\omega) + i\beta(\omega). \tag{1.31}$$

The significance of having a complex imaginary refractive index may not be immediately obvious, but if we expand Eq. 1.30:

$$\begin{aligned}\psi(x, y, z, t) &= \psi_0(x, y, z)e^{-i\omega\left(\frac{1-\delta+i\beta}{c}\hat{\boldsymbol{k}}\cdot\mathbf{r}-t\right)} \qquad (1.32)\\ &= \psi_0(x, y, z)e^{i\omega t}\underbrace{e^{\frac{-i\omega}{c}(1-\delta)\hat{\boldsymbol{k}}\cdot\mathbf{r}}}_{\text{Complex}}\underbrace{e^{\frac{\beta\omega}{c}\hat{\boldsymbol{k}}\cdot\mathbf{r}}}_{\text{Real}}, \qquad (1.33)\end{aligned}$$

where we have inserted the longhand version of n and then factored out the time-varying part exponential, we see that the real part, 1 - δ, affects the *phase* of the wave, while the imaginary part affects the *amplitude*. Considering that some of a photon's energy will be expended by inducing electron oscillators, we can deduce that the photon's amplitude must decrease as it propagates through the medium, thus β is negative in Eq. 1.33. Another useful way of seeing how the "complex" part of Eq. 1.33 affects the phase of a wave, is via the electric field:

$$\boldsymbol{E} = \boldsymbol{E_0}\underbrace{e^{i\omega(\frac{1-\delta}{c}\hat{\boldsymbol{k}}\cdot\boldsymbol{r}-t)}}_{\text{wave \& phase}}\underbrace{e^{-\frac{\omega\beta}{c}\hat{\boldsymbol{k}}\cdot\boldsymbol{r}}}_{\text{absorption}}. \tag{1.34}$$

If we consider the intensity, $I = |\boldsymbol{E}|^2$, in this medium, we have in fact arrived at the Beer-Lambert law for attenuation:

$$\begin{aligned}I &= |\boldsymbol{E_0}|^2 \exp\left(-\frac{2\omega\beta}{c}l\right); \qquad (1.35)\\ I &= I_0 e^{-\mu l}, \qquad (1.36)\end{aligned}$$

where we have defined the attenuation coefficient as $\mu = 4\pi\beta/\lambda$, and denoted the wave's path length through the medium as $l = \hat{\boldsymbol{k}} \cdot \boldsymbol{r}$. If we make the further assumptions that, as a wave passes through an object, the variations in its z component are small and that *the object is sufficiently thin*[1], we may forgo the

---

[1] The so-called "thin object approximation" [5]

step of propagating the wave via Eq. 1.13, and instead model the object as a complex planar transmission function:

$$T(\omega, x, y) = \exp\left[-k\int_{\text{object}} \beta(\omega, x, y, z)dz - ik\int_{\text{object}} \delta(\omega, x, y, z)dz\right], \tag{1.37}$$

which can be applied directly to the waveform via multiplication.

This framing of the situation is powerful, and we can use it to derive the effects of refraction of a wave due to a change in phase. We begin by denoting the phase to be $\phi(x, y) = -k\int_{\text{object}} \delta(z)\mathrm{d}z$ and consider the effects of this due to the Helmholtz propagator (Eq. 1.14). For simplicity, I consider the one-dimensional version of the equation and make two approximations: first, that ϕ may be expressed by a Taylor expansion around $x = 0$:

$$\phi(x) = \phi_0 + x\partial_x\phi, \tag{1.38}$$

and secondly, that the decrease in amplitude, denoted by

$$M(x) = e^{-k\int_{\text{object}}\beta\mathrm{d}z}, \tag{1.39}$$

is constant over a small region.
Consider also a property of the Fourier transform:

$$\mathcal{F}[e^{ik_0x}f(x)] = \tilde{f}(k - k_0), \tag{1.40}$$

where $\tilde{f}(k)$ is the Fourier transform of $f(x)$, and the Helmholtz propagator as expressed in terms of Fourier transforms in Eq. 1.15. Appling these to a wavefront that has been modified by the presence of a sample, $M\psi_0 e^{\phi_0 + x\partial_x\phi}$, and neglecting the constant phase from ϕ_0, we find:

$$\psi_z/(Me^{ikz}) = \mathcal{F}^{-1}\{\mathcal{F}[\psi_0 e^{x\partial_x\phi}]\exp[\frac{-iz}{2k}k_x^2]\}, \tag{1.41}$$

$$= \mathcal{F}^{-1}\{\tilde{\psi}_0(k_x - \partial_x\phi)e^{\frac{-iz}{2k}k_x^2}\}, \tag{1.42}$$

and now changing variable: $g = k_x - \partial_x\phi$

$$= \mathcal{F}^{-1}\{\tilde{\psi}_0(g)\exp(\frac{-iz}{2k}[g^2 + 2g\partial_x\phi + (\partial_x\phi)^2])\}, \tag{1.43}$$

$$= \exp(\frac{-iz}{2k}(\partial_x\phi)^2)\times \mathcal{F}^{-1}\{\underbrace{\tilde{\psi}_0(g)\exp(\frac{-iz}{2k}g^2)}_{\text{Original format}}\underbrace{\exp(\frac{-izg\partial_x\phi}{k})}_{\text{Shift function}}\}. \tag{1.44}$$

The exponential term in $(\partial_x\phi)^2$ in front of the inverse Fourier transform accounts for the extra path length of a deflected field by some object compared to the field in the absence of that object. The terms marked "Original format" are essentially the same expression as seen in Eq. 1.15, but again, from Eq. 1.40, we see the exponential marked "Shift function" in Eq. 1.44 is in fact a lateral shift, in real space, of the waveform by an amount $z\partial_x\phi/k$; for a small angle, this corresponds to an angular deflection given by

$$\alpha = \partial_x\phi/k. \tag{1.45}$$

In ray-optics terms, this is the refraction angle of a photon.

1.5 Planar x-ray imaging

From Eq. 1.37, it is apparent that if $|\nabla\beta| > 0$, then at different points in space immediately after an object, the waveform will have differing intensities. In other words: if an object is made up of materials that attenuate x-rays by different

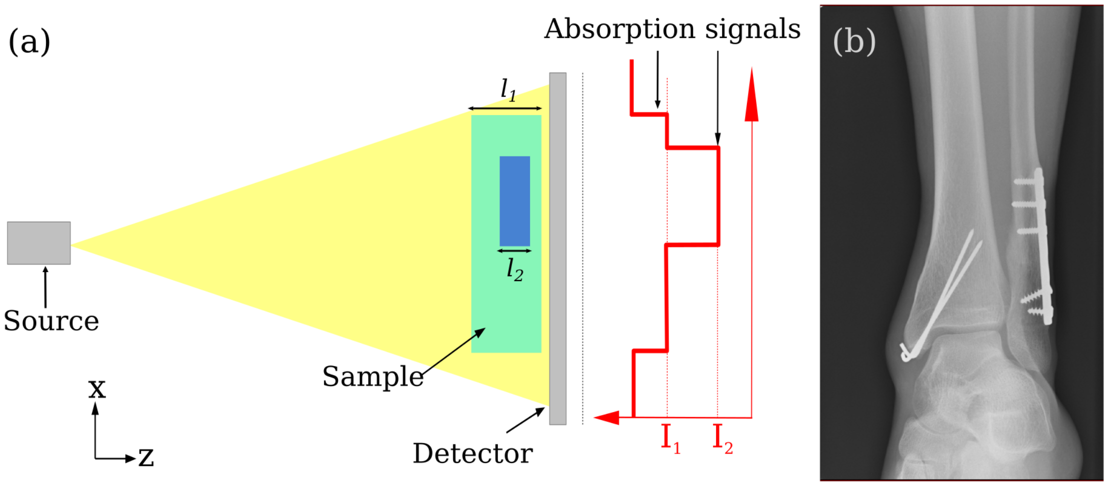

Figure 1.5: Absorption imaging (a) schematic and (b) example - of my ankle - showing the intensity variations between soft tissue, bone and metal.

amounts (they have different attenuation coefficients), such as bone and soft tissue, then those materials may be distinguished by the intensities of any transmitted x-rays. This is *x-ray attenuation imaging* and is illustrated schematically and by example image in Fig. 1.5 (a). The contrast between two materials is defined as:

$$C = \frac{|I_1 - I_2|}{I_1} = 1 - e^{(\mu_1 - \mu_2) l_2}, \tag{1.46}$$

where the subscripts 1 and 2 refer to the distinct materials encountered by the beam.

1.5.1 X-ray dose

As photons propagate through a material, some are absorbed; this is quantified as the dose received by an object. For biological samples, with the possibility of cell degradation or destruction, possibly leading to cancerous mutations [6], dose becomes an important controllable quantity. It is quantified in different ways, with the metric of choice usually chosen depending on the context of exposure [7]. The following is a brief summary of the terminology in use.

- **Exposure**
  - The ability of an x-ray beam to ionise a mass of air, it expresses the amount of electron charge, Q, liberated per unit mass of air, measured in kg.
  - SI unit: $\mathrm{C/kg_{air}}$
  - Conventional unit: Roentgen; $R = 2.58 \times 10^{-4}$ C/kg.
  - Use: measuring radiation received at a defined plane of interaction, such as a patient's skin.
- **K**inetic **E**nergy **R**eleased per unit **M**ass in ionised **A**ir - Air KERMA
  - Equivalent to exposure, but utilises different units.
  - Unit: Gray / Gy (usually measured in mGy): the kinetic energy released per unit mass, or Joules per kilogram, J/kg.
  - Use: Often more convenient to use than exposure when one wishes to calculate an absorbed dose.
- **Absorbed dose**
  - A measure of energy absorbed per unit mass of a specific material.
  - SI unit: Gy.
- **Equivalent dose**
  - A quantification of biological damage, depending on the *type of radiation*. This quantity introduces a weighting factor depending on the radiation type, which multiplies the absorbed dose.
  - SI unit: Sievert (Sv) = weighting × absorbed dose.
  - Example: x-rays have a weighting factor of 1, while alpha particles have a weighting factor of 20.

- **Effective dose** [8]
    - A generic quantification of biological damage depending on both the type of radiation and the tissue being irradiated, as different organs have distinct radiosensitivities.
    - Each organ or tissue is given a weighting in percent, such that the total weight is 100%.
    - Use: guides imaging and radiotherapy practices for protection of operators and patients.

In this thesis, I make use of the Air KERMA description of dose, as it is a measurable quantity that scales with the number of photons in a beam. Once measured, the dose rate gives us the ability to deliver a consistent level of dose across a variety of situations.

2

X-ray phase contrast imaging

In attenuation imaging, the contrast is generated by differences in $k \int_{\text{object}} \beta(E, \mathbf{r}) d\mathbf{r}$ as a function of $\mathbf{r}$. X-ray *phase* contrast imaging (XPCi) refers to generating contrast by exploiting differences in $k \int_{\text{object}} \delta(E, \boldsymbol{r}) d\mathbf{r}$. To illustrate why this method of imaging is appealing, the ratio δ/β for various elements is shown in Fig. 2.1 - depending on the photon energy, and material being considered, δ can be up to three orders of magnitude greater than β. As $\delta \propto E^{-2}$ and $\beta \propto E^{-\zeta}$, where $3 < \zeta < 4$ depending on the proximity to absorption edges, this potential for increased contrast generation often persists into the regime of hard x-rays, which is ideal if one of the imaging goals is to minimise radiation dose.

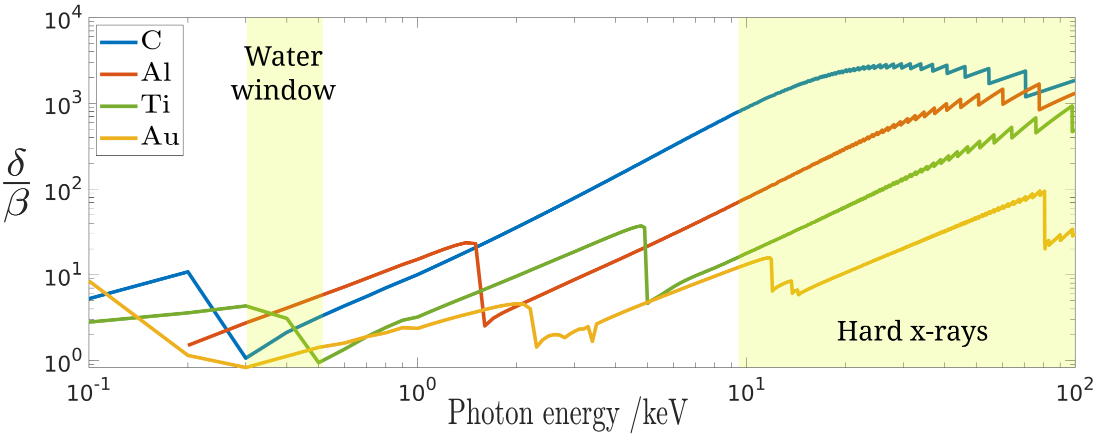

Figure 2.1: The ratio of δ/β for carbon, aluminium, titanium and gold. The "water window" is the part of the EM spectrum for which water is effectively transparent.

While δ is indeed usually larger than β, direct detection of the change in a wavefront's phase is impossible, as detectors measure only the wave's intensity. Instead, different imaging schemes and, in most cases, optics are introduced to the system that enable phase changes to be converted into changes of intensity. This chapter aims to explain how such systems may work and is split into three sections: a discussion of the different XPCi technologies, mentioning their advantages and disadvantages where appropriate; a description of x-ray detectors - how they function and their technical constraints - and finally, a brief summary of how the x-ray masks and gratings mentioned in the imaging systems are manufactured.

2.1 Free space propagation (FSP) / In-line holography

FSP is the simplest XPCi method in terms of its experimental set-up, as no optical elements are required. The scheme, illustrated in Fig. 2.2, is very similar to that of absorption based imaging, the only difference being the introduction of some propagation distance between the sample and detector planes.

FSP was first studied using synchrotron radiation and a photo-sensitive film that allowed for high spatial resolution [9, 10]. The extra propagation distance allowed for the evolution of an interference pattern between the phase-shifted and unperturbed wavefronts, observed as a series of fringes within and around the object's shadow. Later, Wilkins *et al.* used a micro-focal x-ray source, which had a high spatial but low temporal coherence (i.e. the beam was polychromatic and had a source size measured in microns), and was still able to produce FSP images [11].

A phase map of a sample may be retrieved if the interference pattern is sampled

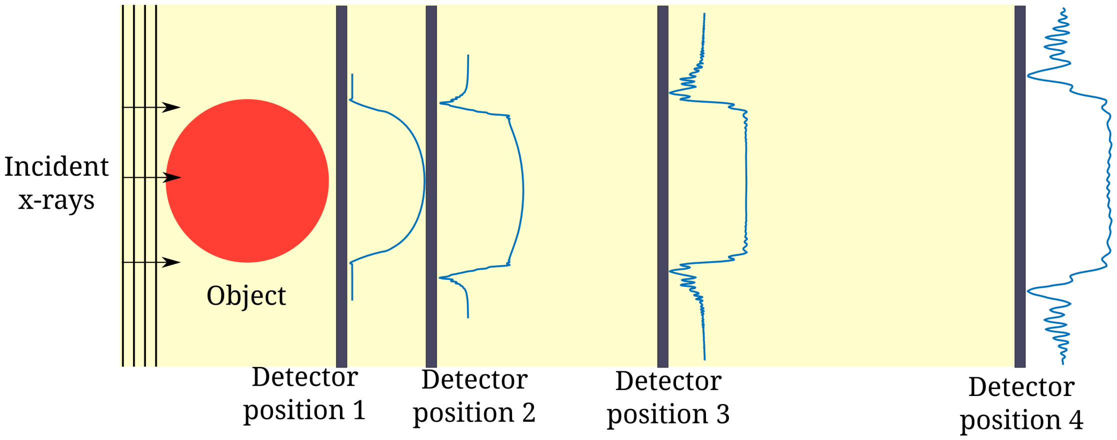

Figure 2.2: Plane wave implementation of a FSP system acquiring images at multiple propagation distances.

at several propagation distances [12], as shown in Fig. 2.2, without any assumptions of sample homogeneity, via the transport of intensity equations [13]. If a sample can be approximated as being homogeneous, however, it is only necessary to acquire one interference image [14]. In general, FSP imaging systems operate in the Fresnel regime, where the Fresnel number, $\frac{a^2}{L\lambda}$, is much greater than one, with a being the characteristic size of the image detail and L the propagation distance. An educational discussion on the meaning of the Fresnel number is made by Gureyev *et al.* [15]. There are several reasons for acquiring images in this regime, namely that to have a long propagation distance, which increases the intensity of fringes, must be balanced against the loss of flux due to the inverse square law. In particular, implementing FSP with micro-focal sources, which have an inherently low flux, typically requires a long exposure time. In order to resolve the fringes for small values of L, however, detector pixels are required to be very small, which also places limitations on the field of view (FoV), as detectors rarely have more than 2048 pixels per side.

2.2 Bonse-Hart interferometry

Bonse-Hart interferometry was the first form of XPCi to be implemented. In the very first experiments, the K_α emission line in copper ($\approx$ 8 keV) and a small

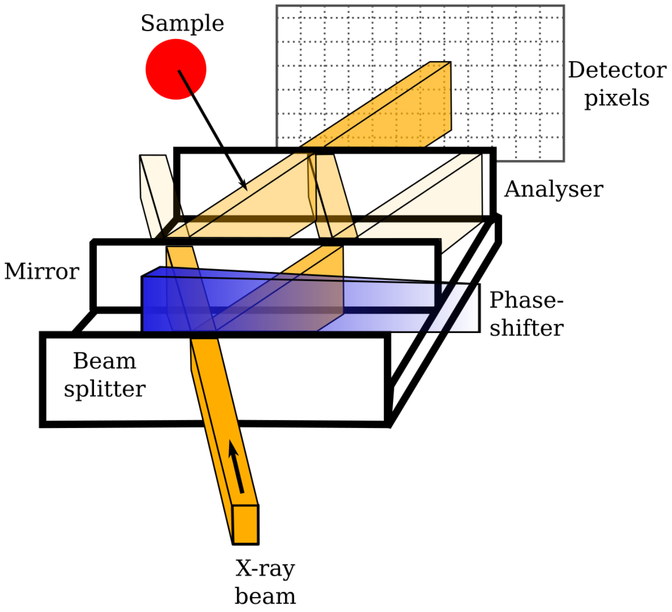

Figure 2.3: Schematic of a Bonse/Hart interferometer. A single crystal cut with two large grooves allows for creation of two mutually coherent x-ray beams.

block of a perfect crystal - usually silicon - with two sections removed in order to obtain three thin blades, were used to create x-ray interference patterns [16]. Single crystals are used in order to ensure that the crystal lattice parameter, which affects the x-ray diffraction pattern, is consistent in all sections.

An incident x-ray beam is split by transmission-diffraction at the first crystal plane into two mutually coherent beams. The beams are symmetrically reflected at the second plane towards each other, as in Fig. 2.3, and upon reaching the analyser crystal, the beams recombine in the detector plane. A phase shifter can be introduced such that, when the beams ultimately recombine, they produce a well defined interference pattern. The presence of a sample in one of the beam arms then shifts and attenuates this pattern by some measurable amount. Quantitative phase information can be extracted, even for complex biological samples, via a fringe scanning procedure, as described by Momose *et al.* [17].

The method is highly sensitive to changes in phase [18], however it requires high stability and incredibly precise alignment of the crystals. The original authors noted distortions in their interference pattern as being due to non-uniform stresses within the bulk crystal, equivalent to a misalignment of 2 Å. This illustrates the difficulty in cutting well-aligned grooves even in single crystals with the result being that interference conditions are usually only valid in small areas, and that the FoV is inherently limited. Additionally, with some flux being discarded due to transmission from crystal planes two and three, the method does not make the most efficient use of photons. The use of Bonse-Hart interferometry is mostly confined to synchrotrons.

2.3 Grating / Talbot-Lau interferometry

Another interference based form of XPCi is grating interferometry (GI) [19, 20] and is based on the Talbot self-imaging effect [21]. The effect is: at certain distances, the diffraction pattern created by a periodic object is an exact replica of the object itself. These certain distances are located at integer multiples of the Talbot distance, z_{Talbot}, downstream of the object:

$$nz_{\text{Talbot}} = \frac{2np^2}{\lambda}, \tag{2.1}$$

where p is the period of the object and n is the integer. These "self-images" also appear at fractional Talbot distances, either with a change in phase or period.

The scheme for using this effect in an imaging system is shown in Fig. 2.4, where two gratings are placed downstream of an object. The phase grating imposes a known modulation of the wavefront; the absorption, or analyser, grating is placed in a self-imaging plane and consists of periodic absorbing septa, such as gold, and transmitting apertures. The periods of both these gratings are typically on the scale of a few microns, with the absorption grating usually being half the pitch of the phase grating (a fractional Talbot order is typically used to maximise modulations [22]). The detector is placed immediately behind the analyser grating

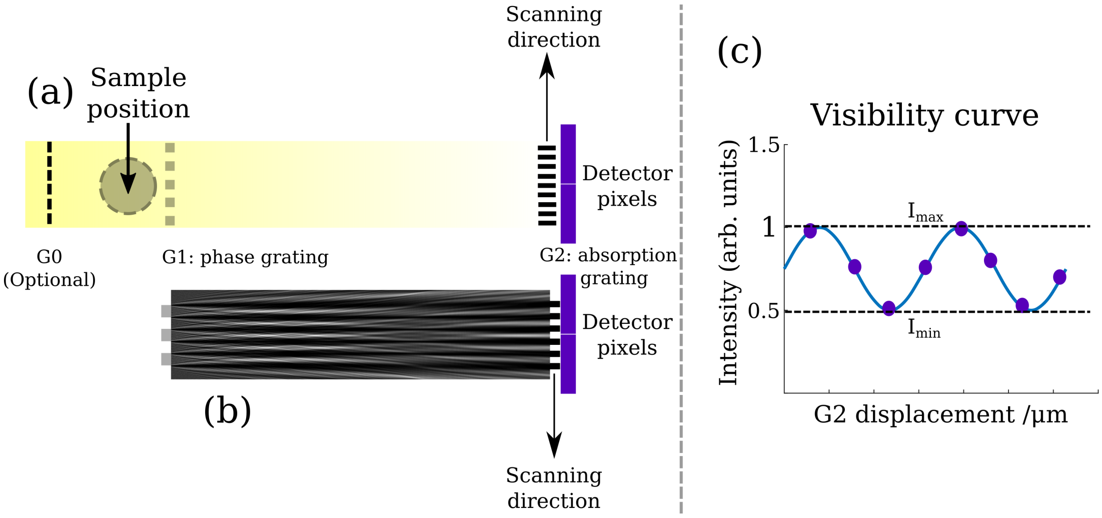

Figure 2.4: TLI imaging system. (a) includes the optional source grating, G0 and indicates the sample position; (b) demonstrates the self-imaging phenomenon as a plane wave propagates beyond a phase grating, G1, to the analyser grating, G2; (c) displays an example Visibility Curve that may be measured as either grating is stepped in either of the indicated directions.

such that, by translating the analyser perpendicularly to the grating lines, the self-image pattern may be finely sampled. The visibility of the system, V, which ultimately determines the system performance, is defined as

$$V = \frac{I_{\text{max}} - I_{\text{min}}}{I_{\text{max}} + I_{\text{min}}}, \tag{2.2}$$

where I_{max} and I_{min} are measured from the visibility curve, as shown in Fig. 2.4 (c). This curve is acquired in the absence of any samples, with a high V indicating good system performance.

In the presence of a sample, the visibility curve acquired may be compared to the reference pattern in order to retrieve the absorption, the first derivative of the sample's projected phase, and the dark field, or ultra-small-angle-x-ray-scattering (USAXS) signal. Absorption causes the average intensity to decrease, refraction causes a shift in the pattern and dark-field signals reduce the overall visibility.

In principle, GI is a coherent and chromatic method, though these limitations can be somewhat mitigated by the following extensions to the technique:

- Extended sources: a spatially incoherent source may be split into an array of coherent, but *mutually incoherent* sources through use of an absorption grating placed before the sample (see G0 in Fig. 2.4 (a)); this is the Talbot-**Lau** configuration for the interferometer [23], which allows for larger source focal-spots to be used and in turn, may increase the amount of flux available.

- Polychromatic sources: the distribution of frequency components within a polychromatic beam will not all produce self-images of the phase grating *in the same plane*; however it has been shown that while this reduces the visibility, it does not wash it out entirely [24]. In fact, the effective wavelength range over which the system can be considered to perform satisfactorily is given by:

$$\Delta\lambda = \frac{\lambda_0}{2n-1}, \tag{2.3}$$

which in essence means that for high Talbot orders, the system tolerance to polychromaticity decreases. A more thorough analysis is made by Engelhardt *et al.* [25].

The restrictions on GI are both technical and practical. The first experiments were conducted using synchrotron radiation with energies of 10 - 20 keV [19, 24], with experiments today progressing to energies of up to 100 keV (though with greatly reduced visibility compared to those low-energy experiments). A prime difficulty in working with high x-ray energies is grating fabrication; the thickness of a gold absorption grating for 100 keV photons would need to be 1mm. This means that, for a 2 μm pitch grating, the absorbing septa would have an aspect ratio of 1000, and while the fabrication of gratings is examined later in this chapter, generally speaking, creating structures with an aspect ratio of $\approx$100 is considered highly challenging. An alternative to making high-aspect ratio structures is to simply turn the absorption grating on its side, which, while effective, greatly reduces the FoV [26]. Finally, a general rule is that the smaller the pitch of an optical element, the more difficult it is to align within the system, and the more sensitive it is to vibrations or thermal variations - this applies to the optical elements in many XPCi systems.

An advantage of the GI system is that it is relatively flux-efficient in terms of system length; i.e. a phase grating pitch of 4 μm, with $\lambda = 0.5$ Å, leads to the first Talbot distance being 4 cm from the phase grating, meaning that very little flux is lost due to the inverse-square law. However, if the absorption grating is effective, this imaging modality results in half of the dose delivered to the sample being wasted, as it does not contribute to image formation. If a source grating is in place as well, much of the flux from the source is necessarily discarded, thus increasing the exposure time required for measurements.

2.4 Analyser based imaging (ABI)

ABI systems are sensitive to attenuation, refraction and USAXS. They employ monochromatic radiation via perfect crystals, which selectively reflect x-rays of certain energies towards a detector; the schematic is illustrated in Fig. 2.5. *Before* the introduction of a sample to the beam, the analyser crystal is rotated, as shown, and the intensity is monitored. The crystal's reflectivity is due to Bragg diffraction, where scattering from ordered atomic planes within crystals results in constructive interference *at certain angles*, as shown in Fig. 2.6 (a). The measurement of reflectivity as the crystal is rotated is known as the *Rocking Curve* (RC) and is shown in part (b) of the figure.

A sample inserted into the beam refracts it by some angle, typically by a number of micro-radians, which changes the angle of incidence on the crystal. If the crystal is rotated to either of the 50% intensity regions of the RC, where the slopes are approximately linear, this change of incident angle results in an

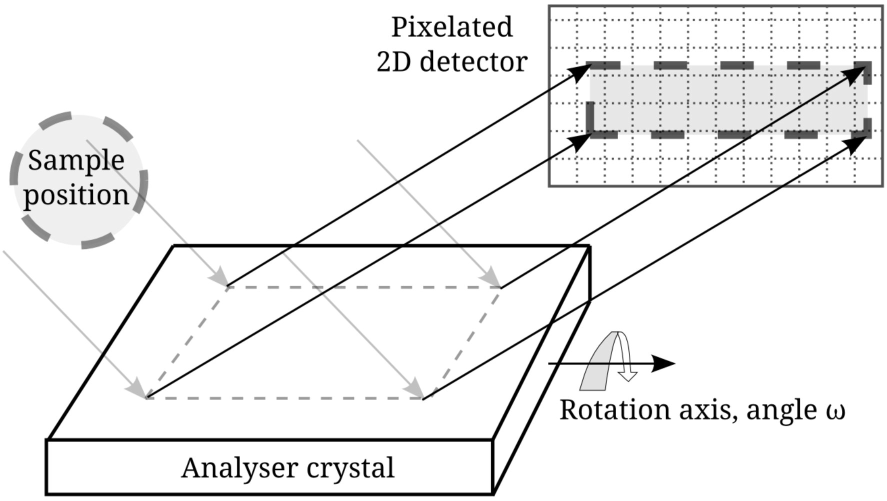

Figure 2.5: Analyser based imaging setup: monochromatic x-rays are incident upon the analyser crystal, which is rotated to measure the crystal reflectivity as a function of ω. X-ray refraction due to a sample results in a change in measured intensity.

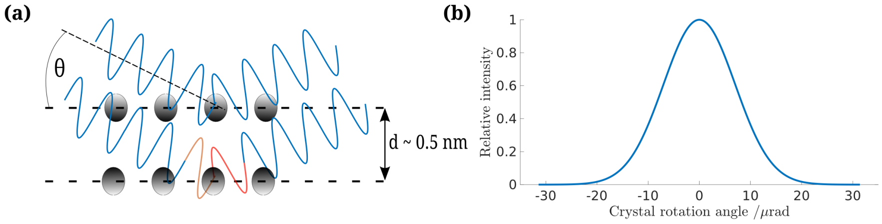

Figure 2.6: (a) Bragg diffraction occurs at certain angles where the optical path length from different scattering layers is an integer multiple of the wavelength λ. (b) An example rocking curve measured by rotation of the analyser crystal.

approximately linear change of measured intensity. The angle of refraction, which is a measure of the gradient of integrated phase, is greatest at the interfaces between details inside the sample and at the sample's edges, leading to "edge enhancement". The refraction contrast - whether refraction leads to an increase or decrease in intensity - can be inverted by rotating the crystal to the opposite side of the RC.

The refraction angle, α, may be recovered by following the steps laid out by Chapman *et al.* [27]: acquire sample images symmetrically at the angles of steepest slopes, where $R''(\theta_{1,2}) = 0$, where each $'$ indicates a derivative with respect to θ.

Then consider the Taylor expansion of R, such that

$$I_1 = e^{-\mu l}[R(\theta_1) + R'(\theta_1)\alpha]; \tag{2.4}$$

$$I_2 = e^{-\mu l}[R(\theta_2) + R'(\theta_2)\alpha], \tag{2.5}$$

where $I_{1,2}$ are the measured intensities. These two simultaneous equations can be re-arranged to solve for the transmission and refraction angle:

$$t = e^{-\mu l} = \frac{I_1 R'(\theta_1) - I_2 R'(\theta_2)}{R(\theta_1)R'(\theta_1) - R(\theta_2)R'(\theta_2)}; \tag{2.6}$$

$$\alpha = \frac{I_2 R(\theta_1) - I_1 R(\theta_2)}{I_1 R'(\theta_2) - I_2 R'(\theta_1)}. \tag{2.7}$$

ABI requires precise alignment of the analyser crystal and a monochromatic source, and its use is thus normally confined to synchrotron facilities. As the crystal also acts as a monochromator, polychromatic sources can be used, but much of the flux produced would then be discarded.

2.5 Edge Illumination

Edge Illumination, with which the experimental data in this thesis have been obtained, was developed by Olivo *et al.* at the Elettra synchrotron [28]. In the synchrotron setting, a narrow x-ray beam is partially incident on an absorbing edge, which obscures some fraction of a pixel. A sample is translated perpendicularly through the beam, with the intensity recorded throughout; attenuation decreases the intensity, while refraction shifts some of the beam either further onto the absorbing edge or further onto the pixel, leading to a reduction or increase in intensity, respectively. For refraction, we generally assume that the beam is refracted by some average amount; if there is instead a *distribution of refraction angles* within the beamlet, then the measured refraction is this distribution's centre of mass, and its width is the dark field, or USAXS, signal. Scattering broadens

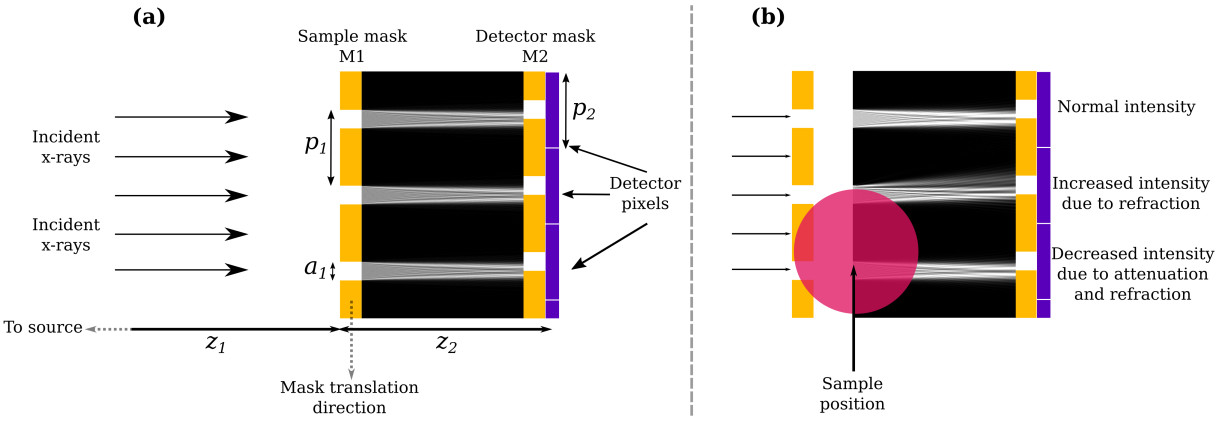

Figure 2.7: The schematic representation of edge-illumination, with dark areas between the masks indicating low intensity regions. (a) Shows the system in the absence of a sample for a plane wave incident on the sample mask, while (b) indicates the position of a sample and its effect on beamlets.

the beam and usually leads to a reduction of measured intensity, though when the beam is incident wholly on the absorbing edge, scattering may be measured as an increase in intensity.

In the case of a divergent beam, as is typical in a lab setting, the beam is first split into an array of beamlets by a periodically absorbing structure, or *mask*. The absorbing edge in front of the detector is replaced by a second mask whose pitch is the same as the detector, with the transmitting sections aligned with pixel centres. To account for beam divergence, the masks are made with the system's geometry in mind, whereby the first mask's pitch is the de-magnified pitch of the second mask. This two-mask scheme was developed by Olivo and Speller [29, 30] at UCL, and is displayed in Fig. 2.7.

At synchrotrons, EI has been demonstrated to be very sensitive to phase effects, with nanoradian refraction angles being resolvable at photon energies as high as 85 keV at the European Synchrotron Radiation Facility (ESRF) in Grenoble [31]. In such settings, the intermediate Fresnel regime - $F \approx 1$ - may be employed, while in the lab setting, $F << 1$.

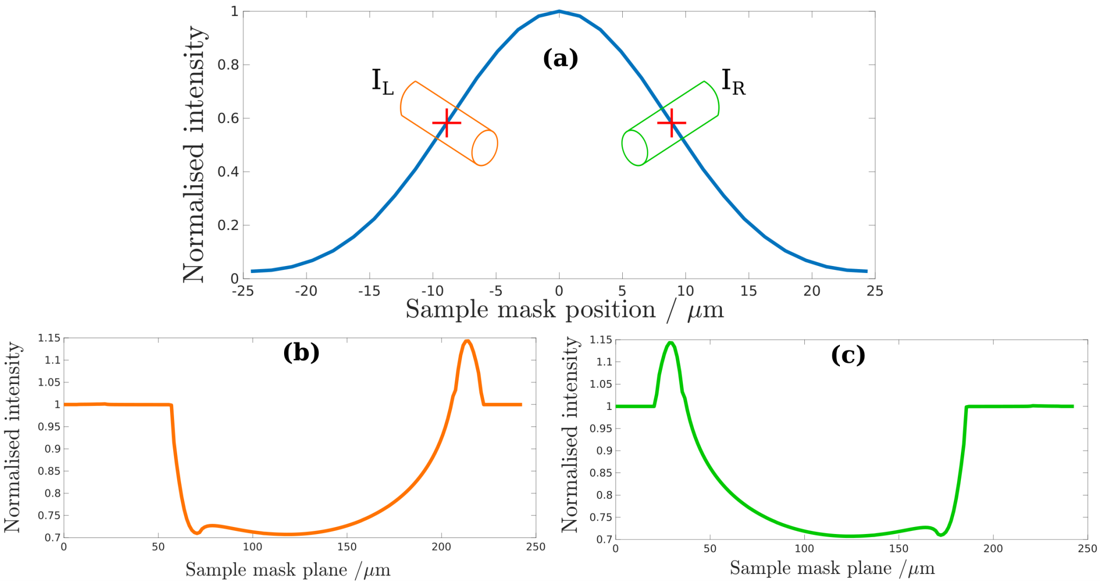

Figure 2.8: (a) Example illumination curve, with (b) and (c) showing wire profiles acquired while the sample mask is located in each of the positions marked; the profiles show a mixture of phase and absorption effects, with the positive and negative phase contrast peaks being inverted between (b) and (c).

When translating the pre-sample mask, M1, perpendicularly to the beam direction over one period, the array of x-ray beamlets are also, in effect, shifted with the mask. The intensity recorded will be a maximum when the beamlets are aligned with the apertures of the detector mask, M2, and a minimum when they are perfectly misaligned. This dependence of intensity as a function of M1's position is the Illumination Curve (IC), which is conceptually similar to the rocking curve used in ABI, and an example is shown in Fig. 2.8 (a). Parts (b) and (c) of this figure show intensity profiles of a wire measured on each of the IC slopes to demonstrate the inversion of positive and negative phase peaks.

A retrieval process similar to that used in ABI may be employed to extract the differential phase and projected transmission of the sample, with the formula developed by Munro *et al.* [32] also accounting for the finite source size, σ_s, and the divergent beam:

$$\frac{\partial \phi}{\partial x} = \frac{\sigma_s \sqrt{\pi}}{2 z_1} \frac{I_R - I_L}{I_R + I_L}. \tag{2.8}$$

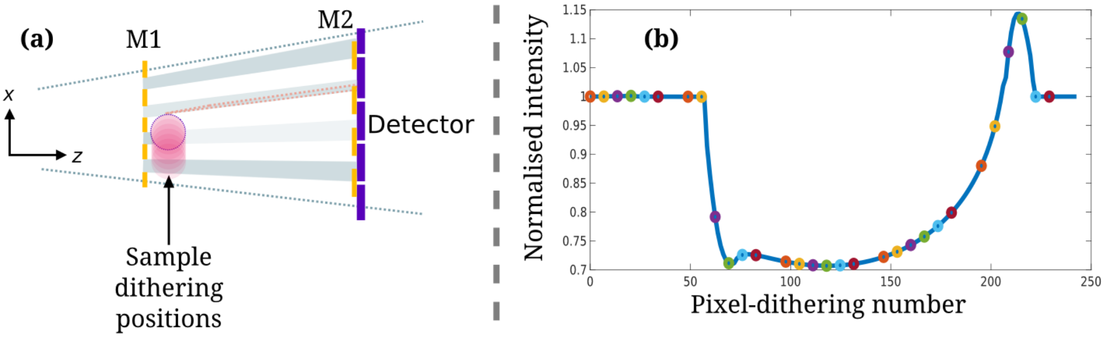

Figure 2.9: An illustration of dithering; in (a), the sample is moved in sub-pixel steps, while the different coloured dots in (b) represent the different pixel intensities is recorded during each step.

Dark-field signals may also be retrieved by acquiring one more image at a separate position of the IC, such as the IC peak, as demonstrated by Endrizzi *et al.* [33]

In the scheme shown in Fig. 2.7, the sampling of the object is equal to the pitch of M1, however, this may be increased by *dithering* the sample. Dithering refers to translating the sample in sub-pixel steps, as shown in Fig. 2.9, acquiring images for each position and then "stitching" the images together. This increased sampling of the object leads to clearer definition of resolvable features. In the direction parallel to the apertures - not shown - the resolution is determined by blurring due to the source, detector cross-talk and the pixel size [34].

While EI bears physical similarities to GI and processes data in much the same way as in ABI, it is distinct from them for the following reasons:

- The gratings employed are both absorption gratings with pitches more often close to 50 μm than 5 μm; they do not produce interfering x-ray beamlets [35], so the technique is non-interferometric [36] *and* achromatic [37, 38];
- The rocking curve equivalent - the IC - has lower spatial and temporal coherence requirements from the x-ray source [39].

Another technical advantage of EI masks over the gratings of GI is that the required aspect ratio is significantly lower. This makes them easier to fabricate,

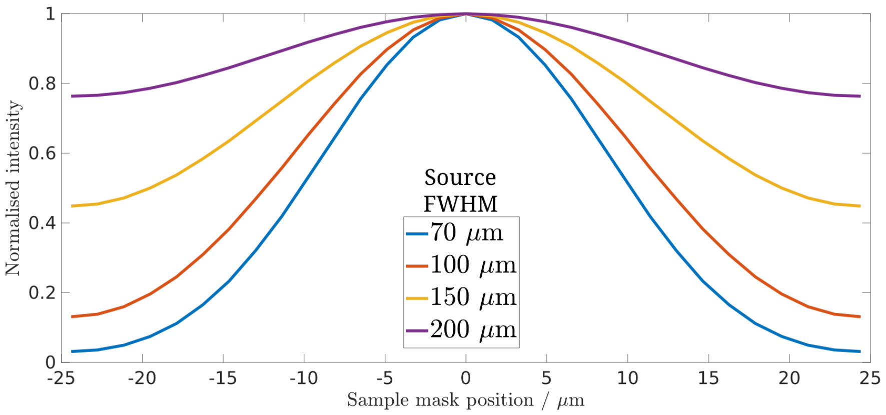

Figure 2.10: Illustration of the source size's effect on the IC: larger sources, if used with the same EI system, lead to a reduction of sensitivity to phase effects.

more stable over time and, with their larger pitches, less sensitive to vibrations during experiments.

In terms of dose delivered to the sample, the system is efficient, as most of the photons that interact with the sample are used in image formation. The total dose varies according to how much resolution is required (how many dithering steps) and the levels of noise that can be considered acceptable (exposure time). As an example of dose efficiency, the dose accumulated while imaging an ex-vivo tissue sample has been shown to be comparable to that delivered in clinical mammography environments [40].

2.5.1 Extensions to EI

As EI is the main focus of this thesis, developments that extend the method beyond its core principles are listed here for completeness, though not all are used in the thesis.

Concerning source sizes, which contribute to image blurring and are a factor in determining a source's brilliance, contrast for a given sample has been shown to remain fairly constant for sizes of up to 100 μm, despite the near complete loss of spatial coherence [30]. However, conventional x-ray tubes found in hospitals, such as ones used in angiography, can have source sizes considerably bigger than this - by several times - in order to produce the required flux. If EI systems were employed directly in these cases, contrast may be significantly affected; as beamlets begin to overlap, the IC is significantly broadened - see Fig. 2.10. A “flattened” IC means that refraction due to a sample causes little-to-no appreciable change in intensity arriving at the detector, thus vastly reducing the sensitivity of the system to phase effects. A solution to this issue is to either collimate the beam, which removes the benefits of high-flux, or to employ a source-mask, which only partially reduces the source flux; in either case the exposure time can be tailored such that the total dose delivered to the sample, or alternatively the background noise in the images acquired, is constant. If a source-mask is employed, it is possible to deconvolve the multiple sample images produced by the mini-sources and retrieve a sharp image of the sample [41].

Considering the mask structures themselves, we find that the 1-dimensional phase sensitivity is not an unavoidable limitation. As shown by Kallon *et al.* [42], two-directional masks may be employed in order to achieve phase sensitivity in both the x and y directions. The disadvantage of this system is in the scan time requirements being squared if dithering in both directions is employed, i.e. scan time $\propto N_{dither}^2$. Further, in order to maximise the dose-efficiency of the system, in some cases it is possible to remove the detector mask and instead align the beamlets such that they fall between two (or more, in the 2D implementation) pixels [43]. This requires that the detector in use has a sharp point-spread function (PSF), which is most commonly the case in direct-conversion detectors. Such an implementation reduces the resolution by a factor of 2, but the simplified setup and increase in detected statistics for a given exposure time may occasionally be preferable in terms of system implementation. As the dose rate for a single-mask setup is the same as in the two-mask setup, there are also potential benefits in

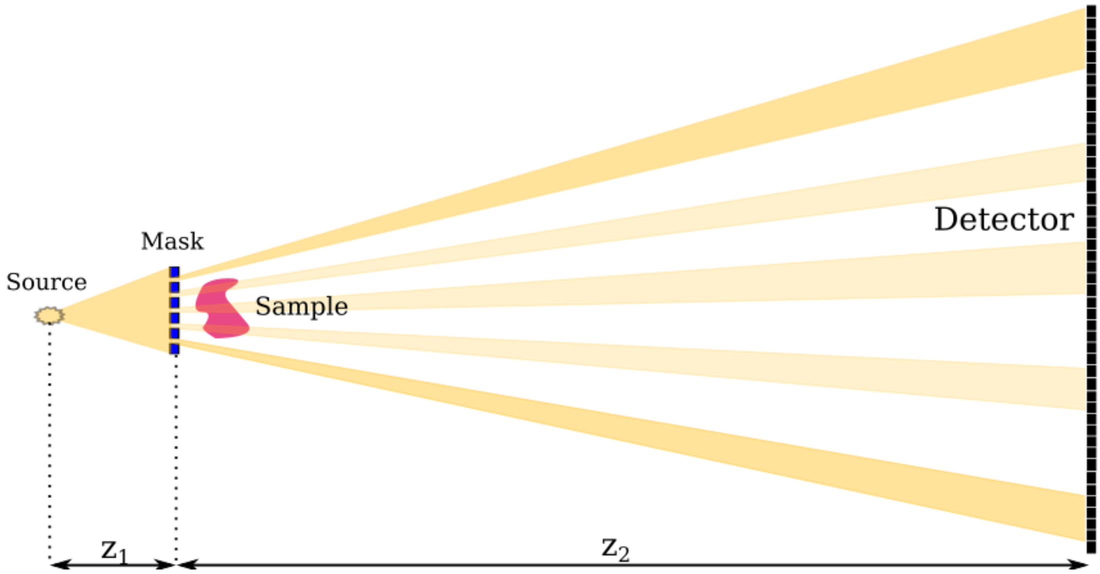

Figure 2.11: Beam tracking scheme. Only the pre-sample mask is needed, with each beamlet arriving at the detector and detected by multiple pixels.

terms of total dose reduction.

If a single-mask setup is desired, but the detector PSF is large or the pixels are smaller than the beam, beam-tracking may be an appropriate adaptation of the EI technique [44]. In this configuration, shown in Fig. 2.11, the sample mask has a relatively large period, or the magnification may be defined such that the projected pitch on the detector is over multiple pixels. For example, if a beamlet is centered on a given pixel, and n neighbouring pixels in all directions register some signal due to this beamlet, then the next beamlet might be centered $2n+1$ pixels away. By translating the sample mask perpendicular to the beamlets over one pixel width, the intensity profiles of each beamlet may be finely sampled. Introducing a sample immediately after the mask in this case, and considering each set of $2n$ pixels, the reduced intensity, shifted centre-of-mass and increased width of the beamlets, corresponding to absorption, refraction and dark-field signals, respectively, may be measured with a single acquisition.

Given the uncertainty in positioning of the sample mask during long acqui-

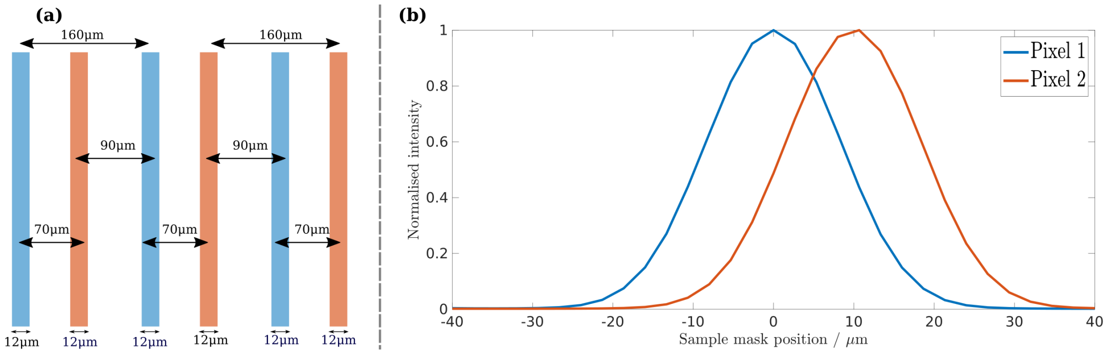

Figure 2.12: Schematic of asymmetric (pre-sample) mask implementation of EI. (a) Shows a possible mask design in terms of aperture positions and (b) shows the corresponding ICs measured by the even and odd pixels respectively.

sitions, a system which requires only one positioning step and that still enables multiple IC sampling, is sometimes needed. This demand is answered in the form of asymmetric mask designs [45] - see Fig. 2.12 for an example. Here, the sample mask is sub-divided into a number of different periods, where adjacent apertures are shifted by a known amount such that, for the number of sub-divisions, there are shifted ICs in each pixel. The advantage here is that, in a single sample-scan, parts of a sample are imaged for different IC positions simultaneously, enabling fast retrieval of attenuation, phase and dark-field signals.

Finally, while planar images of an object can be sufficient for many applications, for some, it is beneficial to have a fully 3-dimensional representation of a sample. This can be achieved through computed tomography (CT) in conventional x-ray imaging, and work has been done to enable extensions of this to many XPCi methods, with those regarding EI being made by Hagen *et al.* [46, 47], among others. Further developments by Zamir *et al.* [48] enabled relatively short CT scans to produce detailed phase and attenuation maps of the internal structure of biological specimens.

2.6 X-ray detectors

There is a wide variety of detector technologies, of which this section aims to describe a few. As I mainly made use of two detectors here at UCL - the Hamamatsu flat-panel and the photon-counter, Pixirad - I shall provide a broad overview of detector characteristics, but focus mainly on those relevant to these two detectors.

Roentgen's original experiments made use of a barium platinocyanide scintillator, which fluoresces in the presence of x-rays, producing a shower of visible light photons that then interacted with photographic film [49]. In the case of a screen, the granularity of photo-sensitive compounds determines its ability to create images in terms of resolution and uniformity. Ideally, all the grains are of similar size and distributed evenly throughout the imaging plane of the screen and the smaller they are, the better the resolution [50]. In the discussion that follows, much of the information and illustrations are inspired by the paper by Allè *et al.* [51]

2.6.1 Indirect detectors

Indirect photon detection, where x-rays are detected through secondary effects, uses a scintillator and collector, with pixels instead of film. Scintillators themselves can be made of a variety of materials, such as CsI:Tl or Gd_2O_2S:Tb, which can be coupled to photodiodes through direct deposition, optical fibres or lenses. The fibres are connected either to a charge-coupled device (CCD), or a complementary metal oxide semiconductor (CMOS) sensor. The signal diffusion due to scintillation lowers their intrinsic resolution, however these systems are usually capable of performing with sufficient efficiency at high energies thanks to the high-Z elements in the scintillator. [52]

CCDs are photon detectors that, after a scintillator converts x-rays to visible

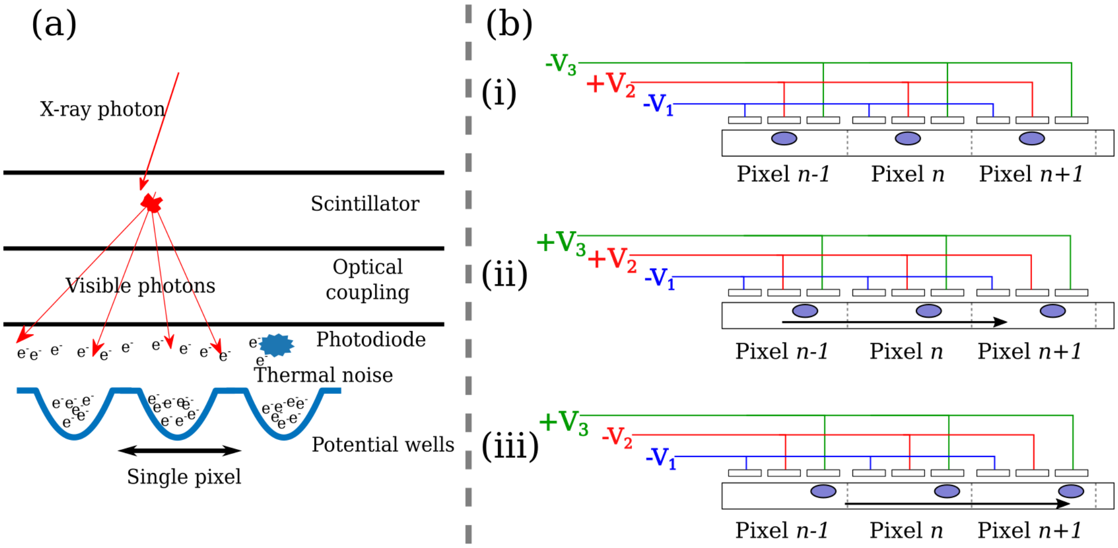

Figure 2.13: (a) Principle of indirect detection: xrays are converted to visible light which excites electrons and these are stored in potential wells. (b) The clocking out mechanism of a CCD: three electrodes execute a sequence of high and low potentials to shunt charge clouds towards a readout terminal. Thermal excitation of electrons contributes to the overall measurement as “dark noise,” which can be reduced by cooling.

light, capture electrons excited by that light in a small region - a pixel. Electrons then accumulate in potential wells, defined locally by one of three electrodes on the pixel surface, until the integration time is reached - see Fig. 2.13 (a). To readout the pixel intensities, or the size of each pixel’s charge cloud, the three electrode potentials are increased and decreased in sequence, as shown in (b), (i) - (iii). V_3 is increased from the negative to positive voltage value until the charge cloud is moved between the second and third electrodes, after which V_2 decreases from positive to negative until the charge cloud is coupled only to the third electrode (this is what is meant by *charge-coupled* device). Repeating this shifting sequence of potentials many times results in electrons flowing from pixel to pixel until reaching an amplifier, which measures the value of each charge cloud and converts it to a voltage - the “output” - corresponding to each pixel. The upper measurement limit of a CCD is determined by a pixel’s maximum charge cloud capacity. Some other limitations of CCD-based detectors are:

- Long readout times (on the order of a second per frame) due to each pixel in a given column being read out by the voltage shifting sequence, one at a time, as described above.

- Charges that have been excited by ambient thermal energy contribute to the measured current. This “dark noise” increases with integration time, so the only preventative measure is to lower the system temperature as much as possible.
- The potential wells become saturated and then “overflow”, leading to incorrect measurements in adjacent pixels.
- During transfer of charges between pixels, electronic noise accumulates. This can be due to some electrons not being transferred with the full cloud during the voltage shifting sequence and eventually contributing, erroneously, to the intensity measured in other pixels.

CMOS detectors are distinct from CCDs in that, instead of clocking-out the charge clouds, they are read out directly by a transistor embedded within each pixel [53], meaning they have reduced readout times compared to CCDs. If pixels are also coupled with amplifiers, the sensor is said to be an *active* CMOS detector.

Flat panel detectors, which can be either indirect or direct detectors, are arrays of detector material coupled to thin film transistors (or CMOS sensors). Similar to the CMOS readout mechanism, these are read directly at the site of excitation. The indirect flat panel detectors are typically based on amorphous silicon [54] and direct detectors on amorphous selenium [55]. The Hamamatsu flat panel detector, used in this thesis, is a single CMOS tile with a directly deposited CsI scintillator.

2.6.2 Direct detectors

Direct detectors do not make use of scintillators, rather, they use a sensor layer which directly converts x-ray photons into electron-hole pairs which is accelerated

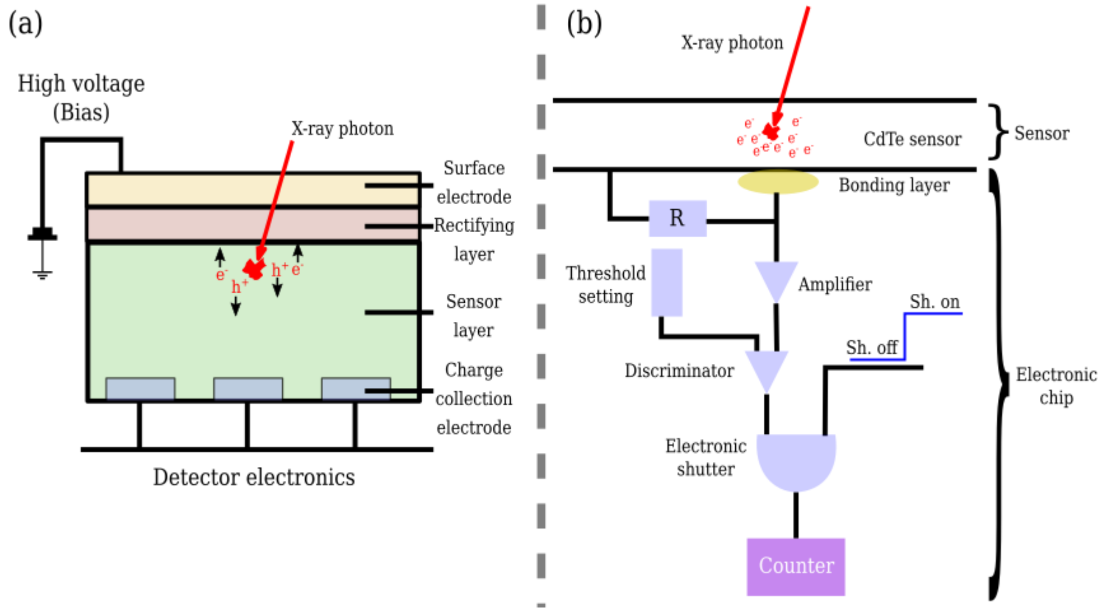

Figure 2.14: (a) Direct detector scheme: x-rays create electron-hole pairs in the sensor layer which are attracted to opposite electrodes. (b) Simplified electronics diagram for x-ray photon counting: an applied voltage accelerates charge clouds to an electrode and the resulting signal is amplified; the discriminator attempts to distinguish individual photon events by noting how frequently a certain threshold is exceeded. The electronic shutter controls for how long the counter increments - it is a logic gate.

towards an electrode by an applied voltage, or bias, as shown in Fig. 2.14 (a). To absorb x-ray photons, the sensor layer needs to be a high-Z material; CdZnTe, CdTe, GaAs are some commonly used examples. A thicker sensor layer increases the chance of stopping a given photon, however the likelihood of electron-hole recombination increases with the sensor thickness, and in addition, the bias voltage must be increased to maintain a high electric field within the photoconductor, which can occasionally be a limiting factor. Direct detection sensors can be integrators or photon counters.

In the case of a photon counter, such as the Pixirad used in this thesis, the signal due to a photon event is processed according to the (simplified) diagram in Fig. 2.14 (b):

- Amplification of the signal by charge-amplifier,

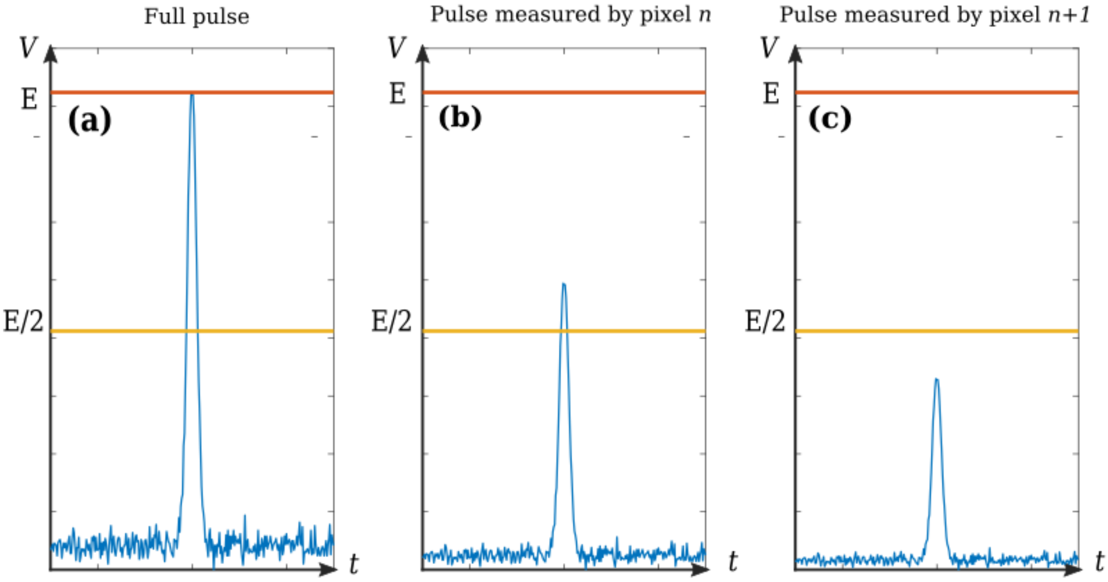

Figure 2.15: Prevention of double counting of monochromatic x-rays by the discriminator in photon counting electronics. A photon incident near the boundary between pixel n and $n+1$ of energy E is amplified to the corresponding signal shown in (a). Pixel n and $n+1$ "see" the signals in shown in (b) and (c) and if the threshold is set to $E/2$ as shown, then only one event is counted, in pixel n.

- The signal is compared against a threshold which, if exceeded, is then transmitted.
- Temporal discrimination of photon events by the electronic shutter which, if "ON",
- The logic counter increments by one.

Photon counters do not rely on potential wells, so each pixel has a counting capacity limited only by their logical rank, or number of bits, e.g. a 16-bit counter can theoretically record up to $2^{16}-1$ photon events. While this means that the detector *can* be saturated, in practice this can be avoided by a sensible choice of photon-integration time, and if statistics greater than the saturation limit are needed, acquiring multiple frames. The discriminator, whose operation is shown in Fig. 2.15, plays an important role in preventing double-counting of photons due to the charge-sharing effect. Charge sharing, which depends on where a photon arrives within a pixel and its energy, refers to when electron clouds produced by a single photon are distributed between, and possibly detected, by two pixels, when only one event should be counted. When considering a monochromatic photon, if the discriminator threshold is half of the photon's energy, only one of the pixels can possibly measure a signal. In a polychromatic beam, however, it is usually not worth setting the threshold to half of the maximum energy, which could result in losing *more* than half of the photons, so a compromise of using lower threshold values must be employed, with the acknowledgment that this will lead to some amount of multi-counting.

2.6.3 Sources of image blurring

2.6.3.1 The source

As mentioned previously, an increasing source size leads to overlapping beamlets and thus to wider, flatter ICs. We can examine this effect analytically via the same framework laid out in Chapter 1. Here I follow the reasoning of Vittoria *et al.* [56] for the one-dimensional case of a wave emitted from a point source located at $x_s = 0$, i.e. $\psi_0(x) = A_0\delta_D(x)$, where δ_D is the Dirac delta function. In the absence of *any* optical system, the field reaching the detector plane, z_2, after traversing a sample located at z_1, may be written as:

$$\psi_{det}(x) = A_0[H_{z_1}T_{obj}(x)] * H_{z_2}(x), \tag{2.9}$$

where $H_{z_1}(x)$ and $H_{z_2}(x)$ are the propagators from source to sample, then sample to detector respectively, and T_{obj} is the complex transmission function of a sample. For a source not located at $x_s = 0$, the first propagator must be replaced by $H_{z_1}(x - x_s)$. Expanding this propagator, we find:

$$\psi_{det}(x, x_s) = \frac{e^{ikz_1}}{i\lambda z_1} e^{\frac{ik}{2z_1}x^2} e^{\frac{ik}{2z_1}x_s^2} e^{\frac{-ikxx_s}{z_1}}, \tag{2.10}$$

$$\psi_{det}(x, x_s) = \frac{i\lambda z}{e^{ikz}} H_{z_1}(x) H_{z_1}(x_s) e^{-ikxx_s/z}, \tag{2.11}$$

which, once substituted into Eq. 2.9, means we may express the field at the detector due to this *moved* point source as:

$$\psi_{det}(x,x_s) = \underbrace{\exp\big[i\frac{k}{2z_z}(1-\frac{z_2}{z_1})x_s^2 - i\frac{k}{z_1}xx_s\big]}_{\text{Phase factor}}\,\psi_{det}(x+\frac{z_2}{z_1}x_s). \tag{2.12}$$

Thus, for an incoherent source of finite width and spatial intensity distribution $A(x)$, the intensity measured at the detector plane is merely the sum over all points of emittance, weighted by $A(x)$, i.e.

$$I_D(x) = \int_{-\infty}^{\infty} A(x_s)|\psi_{det}(x,x_s)|^2 \mathrm{d}x_s. \tag{2.13}$$

If we rescale the source distribution, such that $A_r(x) = \frac{z_1}{z_2}A(-xz_1/z_2)$, we can simplify the above expression by writing it as a convolution:

$$I_D(x) = A_r(x) * |\psi_{det}(x,x_s)|^2, \tag{2.14}$$

with the intensity being measured in a pixel n being given by

$$\begin{aligned} I_n &= \int_{x_n}^{x_n+p} I_D(x)\mathrm{d}x, && (2.15)\\ &= \int_{-\infty}^{\infty} \mathrm{rect}\big(\frac{x-(n+1/2)p}{p}\big) I_D(x)\mathrm{d}x, && (2.16)\\ &= \int_{-\infty}^{\infty} \mathrm{rect}\big(\frac{x-(n+1/2)p}{p}\big) \int_{-\infty}^{\infty} A(x_s)|\psi_{det}(x,x_s)|^2\mathrm{d}x_s\mathrm{d}x, && (2.17) \end{aligned}$$

where $\mathrm{rect}(\frac{x-(n+1/2)p}{p})$ is used to define the pixel region and is the rectangular, or top-hat function:

$$rect(t) = \begin{cases} 0 & |t| > 0.5 \\ \frac{1}{2} & |t| = \frac{1}{2} \\ 1 & |t| < \frac{1}{2}. \end{cases} \tag{2.18}$$

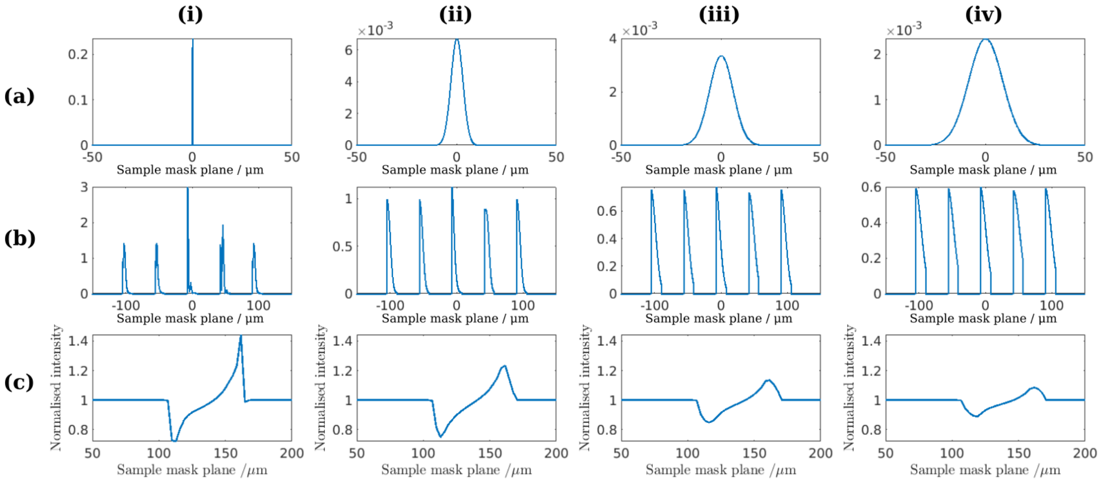

Figure 2.16: Illustration of source-induced blurring. (a) (i) - (iv) show the increasing width of source profiles, with the x axis in μm for the source plane; (b) shows the resulting intensity profiles incident on the detector, before pixel discretisation of the signal occurs, in a five-period EI system. (c) (i) - (iv) shows the resulting profiles, measured by the detector, of a highly sampled and weakly absorbing wire obtained in each case, using the same y axis in each subplot to emphasise how the edge-enhancement effect diminishes with source size.

In terms of how this affects the signal due to a sample, consider the case of a monochromatic EI system of standard geometry: $z_1 = 1.6$ m, $z_2 = 0.4$ m, and detector pixels 62 μm wide, with masks M1 and M2 having demagnified and equal pitches of 49 μm and 62 μm, respectively. A small (49 μm diameter) wire is placed in the sample mask plane and the source is assumed to be a Gaussian of some variable width. We can see the effects of increasing the source size on the intensity profile arriving at the detector in Fig. 2.16 (b): the high frequency spatial components are diminished as the source size increases. Considering the fully sampled wire profiles in (c), (i) - (iv), we see that this reflects a decreasing phase contrast signal. If the source is so large that the beamlets following M1 are strongly overlapping, the assumptions of EI are no longer valid and it possible that all contrast of such objects or samples may be reduced to zero.

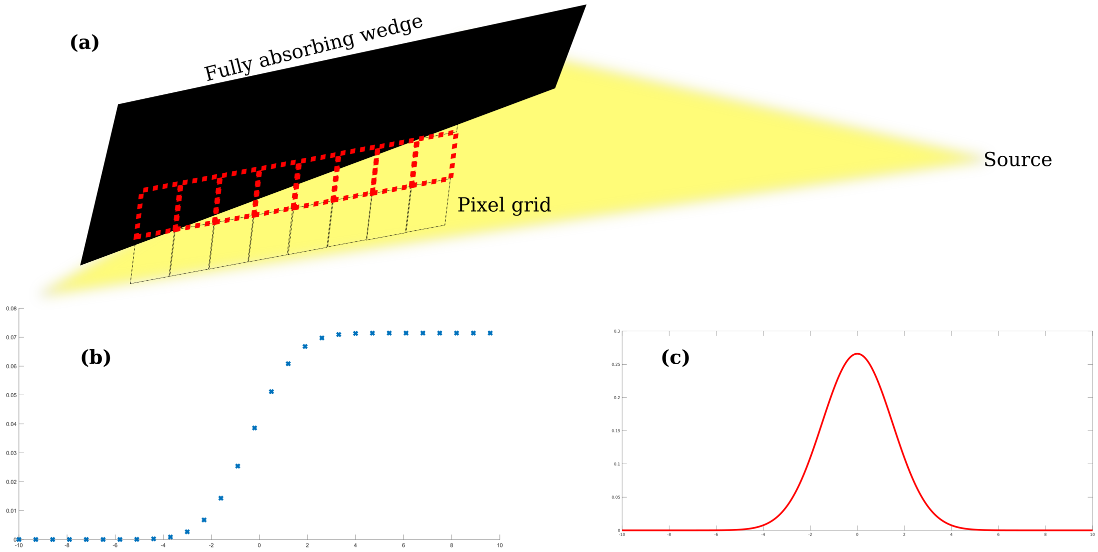

Figure 2.17: Illustration of a point-spread function measurement. (a) shows the data acquisition procedure, (b) an example of the data acquired along a row of pixels, and (c) shows the PSF, which is the derivative of the plot in (b).

2.6.3.2 The point spread function due to scintillation or charge sharing

Depending on where an x-ray photon arrives in a pixel, not all of the resulting signal may be recorded by that same pixel, as the photon (scintillator) or electron (photoconductor) clouds may diffuse across pixel boundaries and be detected in neighbouring pixels as well. This phenomenon is quantified by the point spread function (PSF), which is a description of how a point-focussed signal is diffused in space within a detector. An ideal PSF would be a Dirac delta function such that, when convolved with the pixel function, the latter remains a top-hat as in Eq. 2.18. In reality, however, the PSF will always have some width, which is typically smaller, but may be larger, than the pixel itself; ultimately, the PSF defines the resolution of the detector.

The PSF is not usually measured directly - instead, the effective pixel function, which is the convolution of a top hat and the PSF, is measured. The measurement may be undertaken either by employing a pencil beam and scanning it across a pixel, or, if one assumes that the PSF is uniform for all pixels, the scheme shown in Fig. 2.17 may be used. In this case, a non-transmitting wedge is placed in front of the detector and each pixel's intensity may be plotted as in (b). This is the edge response function and its derivative, shown in (c), is the PSF.

This distribution of signal is due to the scintillator, charge sharing, or a combination of both. A scintillator converts x-rays to optical photons, usually in the ratio of 1:1000, which are emitted with a range of angles. Photons propagate through the scintillator towards the array of photodiodes, where they are collected. If the shower of visible light photons is both large and broad, multiple photodiodes may register the signal from single events.

Charge sharing in photon counters has been already described in Sec 2.6.2, so here we consider the diffusion of an electron cloud created by an x-ray in the photoconductor layer. In relation to pixel electrodes, *where* this cloud is created affects the likelihood of charge sharing between pixels, both in relation to pixel boundaries and the depth at which the event occurs. The likelihood is intuitively greater the closer a photon event occurs to a pixel's edge, while the mean free path of electrons in the material is the governing factor for how depth changes the likelihood; it is also a function of the photon energy, pixel size and bias. Generally, then, the effective pixel function will be slightly greater than the physical pixel size, but less so than in the case of an indirect conversion detector. Thresholding can prevent double-counting, as previously shown, but if not in use, the PSF for a detector will be dependent on the photon energy.

2.6.4 Spectral sensitivities and multi-counting

Detector performance varies according to the photon energies involved; scintillators, for example, make use of x-ray attenuation as described in Ch. 1, with

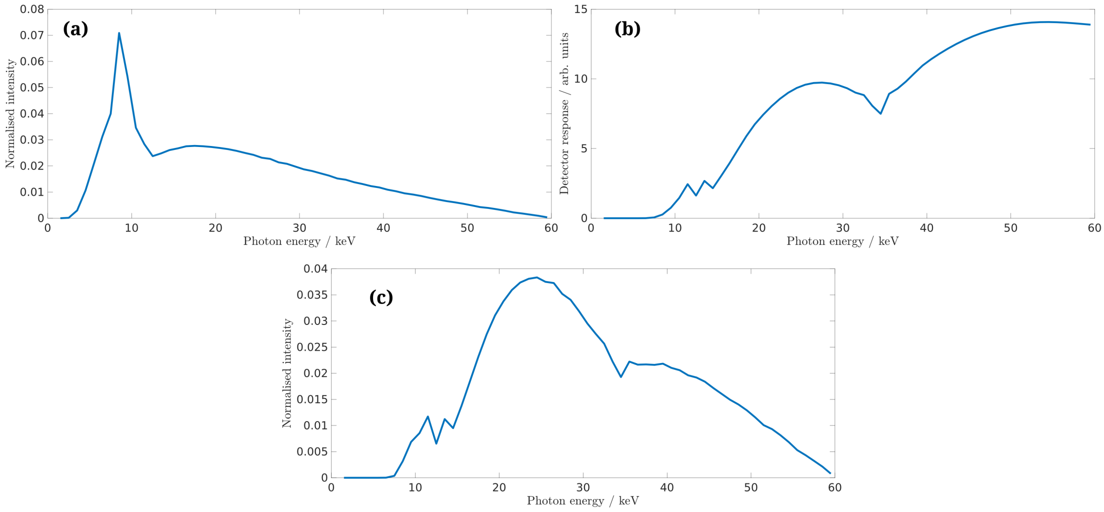

Figure 2.18: Illustration of a detector's energy response being accounted for. (a) shows an example spectrum, (b) shows the measured energy response of the detector and (c) shows their product, which is the effective spectrum.

hard x-rays producing large numbers of optical photons, but being less likely to interact with the scintillator to begin with. For an integrating detector, the first approximation is often one of a linear energy response, which assumes proportionality between energy of the absorbed x-ray and detected signal. In the hard x-ray regime, this breaks down, especially if the scintillator contains elements with sharp absorption edges. Therefore, in polychromatic experiments, the full energy response should be measured and taken into account. The effective spectrum, $\sigma(E)$, is obtained by multiplying the real spectrum by the energy response function, as shown in Fig. 2.18, then normalising the result such that the integral over energy of the resulting spectrum, $\sigma(E)$, is equal to one: $\int_0^{E_{\max}} \sigma(E)dE = 1$.

In photon counting detectors, high energy photons create large clouds of electrons which can lead to charge-sharing. For example, if a photon of energy $E > 4E_{\text{Threshold}}$ is incident near the corner of a pixel, it may be counted up to four times - once by each pixel in the vicinity - as shown in Fig. 2.19. As electronic components continue to shrink in physical size as time progresses, ways of overcoming this effect become open to us; one example is to bundle pixel corners with

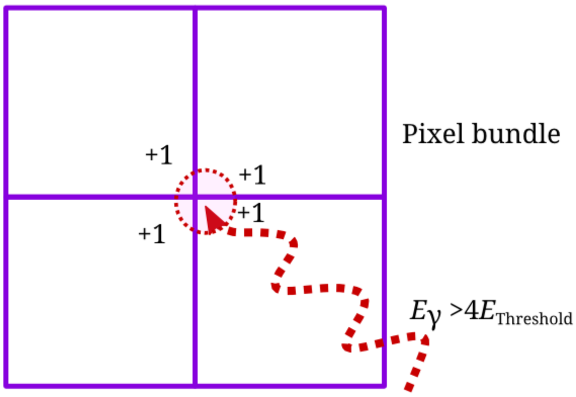

Figure 2.19: Illustration of multi-counting in a direct detector. A photon of energy greater than four times the threshold is incident near a pixel bounday and the electron cloud produced is detected by each of the pixels, leading to over-counting.

photon-coincidence electronics that discriminate against events occuring nearly simultaneously, thus attempting to increase specificity for individual photon events.

2.7 Fabrication of masks or gratings

In this section, a manufacturing method of masks or gratings used in x-ray experiments is discussed [57, 58], with a focus on the technical challenges in making them suitable for high-energy applications. Three reasons why it is difficult to make optical components for x-ray systems are as follows:

- Such components are inherently wavelength specific, which works well in the optical light regime, where lasers are available, but high brilliance monochromatic x-ray sources are usually only available in synchrotrons, outside of which, in polychromatic settings, their performance suffers somewhat.
- The scale on which x-rays interact with matter is so much smaller than the optical regime: refraction angles in focussing optics are on the order of microradians and phase-shifters must be made to a high precision, while the structures themselves require careful engineering to construct. [58]
- Beam-splitters and flat mirrors, which enable 45° and 90° reflections, do not

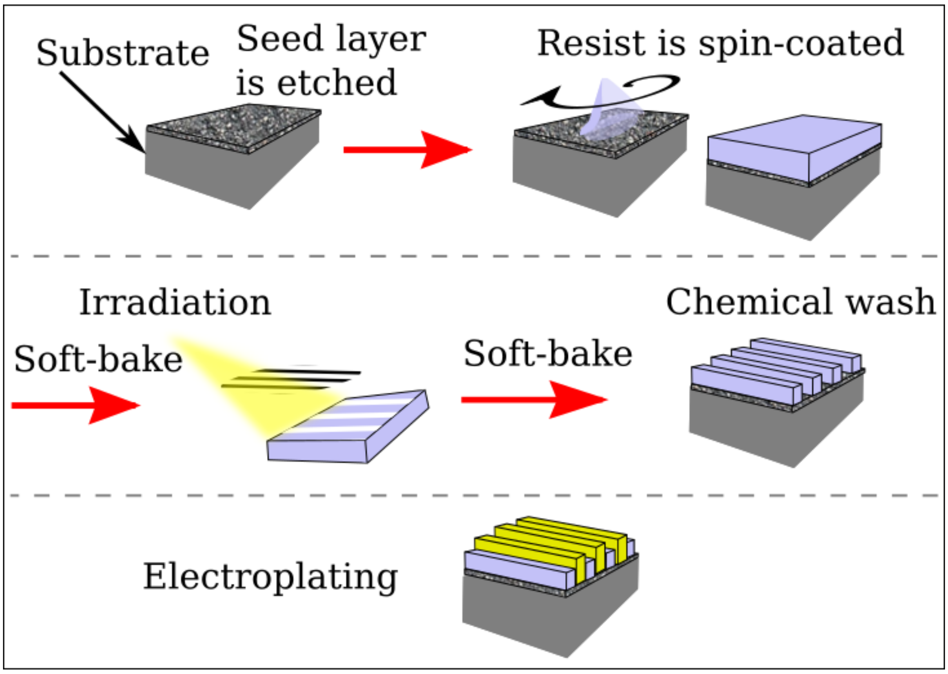

Figure 2.20: A simplified workflow diagram for fabrication of masks or gratings.

exist in the x-ray regime, meaning that the x-ray beam cannot be guided or confined in the same way as in optical systems.

A simplified workflow of the most up to date mask fabrication process is shown in Fig. 2.20. First, a substrate upon which the mask or grating is to be constructed is chosen: silicon or graphite wafers are typical choices, though graphite is known to cause x-ray scattering, particularly at lower energies. The substrate is required to be a sufficiently strong material in order to prevent bending of the mask, have low rates of thermal expansion and be thick enough to support the eventual structures. A thin metallic seed layer (e.g. 3 μm of titanium) is then attached to the substrate by atomic layer deposition. In order to provide a suitable site for adhesion, the seed layer is randomly etched with shallow grooves whose depth is <1 μm; the roughness provides grip for the materials that will be deposited.

Next, a photoresist, either positive or negative, is deposited onto the substrate. A positive photoresist (e.g. PMMA) is one that is damaged by radiation such that the molecular weight is reduced (bonds between molecules are broken): irradiated sections then become soluble in a developer solution. A negative resist (e.g. the epoxy-resin based SU-8) becomes *insoluble* in a developer after being irradiated, the damage in this case causing an increase of molecular weights by inducing the cross-linking of molecules. The amount of radiation required is different for each resist, with SU-8 having a greater sensitivity and thus requiring shorter exposure times (on the order of minutes if using a synchrotron undulator). Deposition of resists can be achieved through spin-coating, seen in Fig. 2.20, which ensures a uniform height and low levels of porosity. Another method, more appropriate for positive resists, involves gluing or casting sheets of the polymer, immersed in an ionic solution, onto the substrate. After the polymer coat has been applied, the solution is removed by baking.

Deep x-ray lithography is the next step, where a mask template is used to selectively irradiate parts of the resist. In the desired sections, the resist is irradiated; for a negative resist, such as SU-8, an embedded chemical salt produces an acid upon exposure to x-rays. The acid acts as a catalyst for cross-linking of the polymer molecules, changing their physical properties such that they do not dissolve when treated by the developer solution, which occurs during the next bake. In order for the lithography to be accurate, highly collimated synchrotron radiation is required in order to ensure a 1:1 shadow is cast by the template mask, with the precision of the technique being ultimately limited by Fresnel diffraction. In general, resists that respond quickly to an applied dose will have sheerer side-walls, which benefit mask and grating performances.

In the case of a phase grating, the steps up to this point may be sufficient, with the tops of the resin merely being treated to ensure a uniform height. For masks and absorbing gratings, however, the final step is one of micro-electroplating. This process varies between manufacturers, and there are many possible variations in terms of details, but in general it involves the following elements:

- The metal to be electroplated is in an electrolyte solution along with the mask structure;
- A voltage is applied such that the metal ions are attracted to the seed layer.
- The overall amount of electroplated material can be monitored by tracking the current between cathode and anode.

Gold is a good choice of plating material, as this does not induce any hydrogen evolution at the mask cathode, unlike other metals such as copper [59].

Micro-electroplating on a lithographic sample is a mechanically complex process. The high aspect ratio of the resists are responsible for disrupting convection currents and determining the size of metal-ion diffusion zones, which is the preferred (stable) mechanism for gold growth, in addition to causing inhomogeneities in the current density across the mask. The voltage applied must also be chosen carefully: too low and the electrodeposition is slowed, limited by surface kinematics, too high and the process is ion-diffusion limited, with the possibility of depleting ions completely at the cathode site.

3

High energy dark field imaging with simplified retrieval and Monte Carlo modelling

In EI, dark field contrast can either be seen directly at the cost of dose-efficiency [60], where most of the primary beam is discarded, or can be retrieved through the processing of multiple image acquisitions [33]. With an assumption of sample homogeneity [14, 61], quantitative parameters of the sample (typically thickness) may be retrieved with a single sample image. If pixel sizes are small enough to allow individual beams to be resolved, beam-tracking (BT) can also be used to retrieve multiple contrasts from a single image. GI and ABI are also capable of extracting the different contrast maps [11, 62, 63], though with differing conditions on system length or detector resolution, optical elements and processing methods [64, 65, 66, 67]; in general, these methods are reliant upon spatially coherent or monochromatic x-rays, respectively. A more thorough discussion of the systems' requirements is made by Diemoz *et al* [68].

This chapter describes high-energy XPCi that utilises multi-modal retrieval of transmission, refraction and USAXS with fewer than normal input frames (and no assumptions on sample homogeneity). Further, a model based on this experiment is used to examine how the position of the pre-sample mask, in general terms, affects the accuracy of the retrieved signal in both EI and BT modalities, in the special case of a beam having widths approximately equal to the pixel size.

Fewer exposures of the sample to radiation can result in lower dose, and the ability to access different contrasts leads to a more complete understanding of a sample's internal structures. Conducting the experiment using synchrotron radiation has the benefit of having relatively few unknowns: highly collimated monochromatic radiation means there are no issues with beam hardening or detector energy response, so benchmarking a model using the data collected here is reasonably straightforward. With a model established, it could be used to test system performance in different settings that would be difficult to achieve in practice, e.g. clinical environments.

3.1 System parameters and method

A weakly absorbing Nylon-6 wire of radius 500 μm and three different concentrations of microbubbles, of known size distribution, were imaged with a modified EI system at the European Synchrotron Radiation Facility (ESRF) using the ID17 beamline. A double-bent Laue crystal [69] was used to select 50 keV photons, which were emitted approximately 150 m upstream of the detector; this was a CMOS detector that utilised a PCO.Edge (type 5.5) camera [70], coupled with a 20% optics and a 50 μm thick GADOX scintillator; the effective pixel size was 21.6 μm.

The EI system is illustrated in Fig. 3.1 (a), with M1 being 2 m from M2, itself 0.5 m from the detector. As the beam was almost parallel, M1 and M2 were made

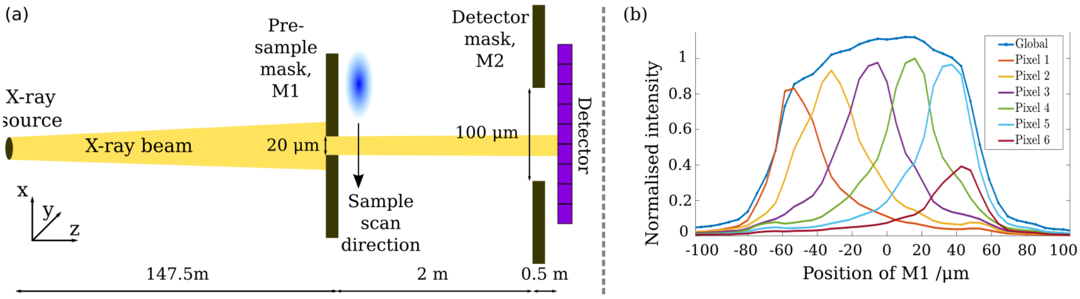

Figure 3.1: (a) Diagram of the EI implementation used at the ESRF (not to scale); the small gap between M2 and the detector is a practical necessity. (b) shows the global and pixel-specific ICs, normalised to appear on the same scale, which are acquired by scanning the pre-sample mask, M1, across an aperture of the detector mask, M2. Pixel 6 has a lower peak intensity as it is almost entirely generated through pixel crosstalk.

with the same pitch of 450 μm, but with five apertures each of 20 μm and 100 μm respectively; the thickness of the absorbing tungsten septa in both masks was 1 mm. The detector mask apertures were designed to be much larger than the sample mask apertures in order to ensure that, in the EI modality, all refracted x-rays were collected, thus achieving a high dynamic range for the system. This setup allowed for a direct comparison between conventional edge illumination and beam tracking, which was conducted with some experimental data and more thoroughly through Monte Carlo modelling of a single-shot acquisition being used for a retrieval of all three contrasts.

To achieve the required thickness of absorbing septa, the masks were made by interlocking three separate components, rather than as a single absorbing piece - see Fig. 3.2. For the experiment described in this chapter, only three apertures were aligned, as it was practically difficult to align all five due to the small beam divergence. ICs were acquired by scanning M1 perpendicularly to the beam, with individual pixel intensities being summed to create the global IC seen in Fig. 3.1 (b); both the local and global ICs were finely sampled and fitted with smoothing splines. When considering the EI modality of the system, the global IC is usually referred to, while the alternative implementation considers the individual pixel

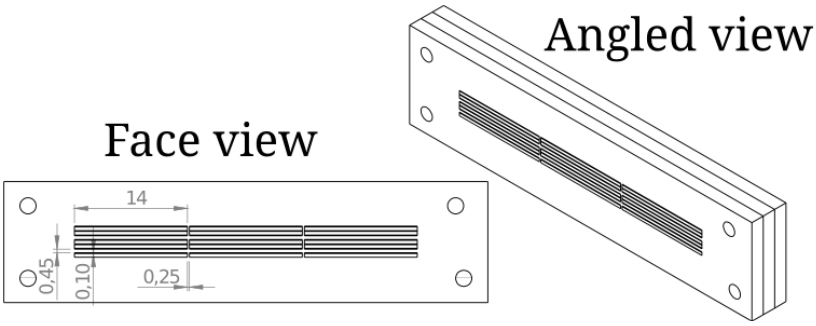

Figure 3.2: Schematic drawing of the masks used during the ESRF experiment, the numbers marked in the face-view diagram are measured in mm.

intensities, similar to the format employed in BT. Samples were also scanned perpendicularly to the beam in discrete steps, with the measured intensities from each step being stitched together to form images. The dose rate of the experiment was monitored by scanning a calibrated ion chamber (0.125 cm^3 semiflex tube chamber, Model 31002; PTW-Freiburg, Freiburg im Breisgau, Germany) across the sample position to measure the air kerma; the measurement protocol followed the procedure described by Mittone *et al.* [71].

3.1.1 Microsphere samples

Expancel$^{\mathrm{TM}}$ microspheres are polymer shells filled with isobutane gas. The shell is rigid unless subjected to large changes in temperature or pressure and has negligible thickness compared to the sphere radius. Following the preparation method described by Millard *et al.* [60], the microspheres were added to a volume of ultrasound gel and stirred carefully to avoid the introduction of air bubbles. Ultrasound gel is used for two reasons: the high viscosity ensures that microspheres do not float and, as the gel is mostly (>98%) water, the refractive index properties can be assumed to be those of water also. This *stock concentration* of microspheres was optically imaged at 20× magnification, using more than 200 images to determine the average concentration ($\approx$ 2.3% by volume) and size distribution, with the results being shown in Fig. 3.3 (b). Lower concentrations of microspheres were prepared by taking controlled amounts of the stock concentration and diluting

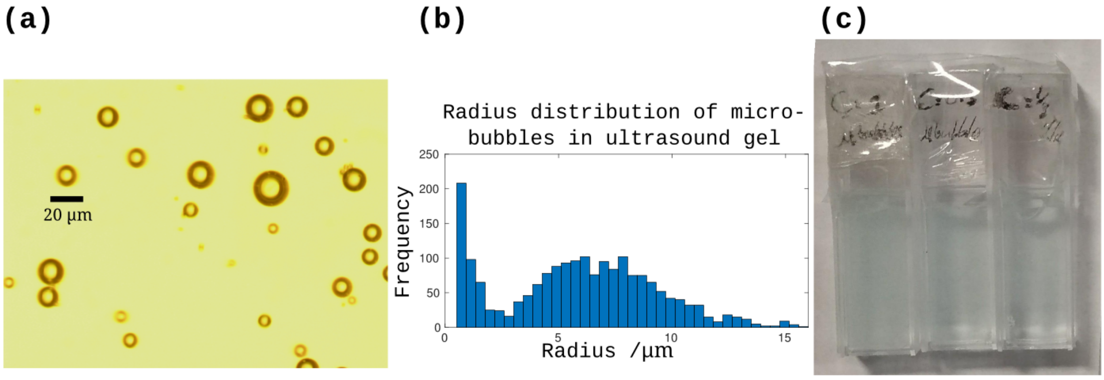

Figure 3.3: (a) Example image displaying 20× optical magnification of Expancel$^{\mathrm{TM}}$ microspheres; (b) measured size distribution; (c) the three concentrations of microspheres used for imaging: left = 100%, middle ≈ 50% and right ≈ 33%.

them with water, making relative concentrations of 1/2 and 1/3. The stock and diluted concentrations were pipetted into 10 mm wide and 4.1 mm deep cuvettes, then sealed and stuck together with tape to prevent spillage and enable imaging of all three concentrations in a single scan.

In the conventional EI modality, the retrieval procedure described by Endrizzi *et al.* [33] was used to retrieve the sample parameters of both the wire and microsphere concentrations, using two and three input frames respectively. When using the individual pixel ICs to perform retrievals, a least-squares minimisation approach was implemented. The difference to be minimised was that between interpolated values of local ICs convolved with a sample function - $f(x_i, t, r, s) = IC(x_i) * O(t, r, s)$, where $O(t, r, s)$ is the sample function - and the experimental data points, i.e.

$$\chi \xrightarrow{\text{Minimise}} \sum_{i=1}^{N} \big(y_i - f(x_i, t, r, s)\big)^2; \tag{3.1}$$

here i refers to pixel numbers within the aperture window, y_i corresponds to each pixel value with the sample in the beam and $f(x_i, t, r, s)$ the interpolated values for sample transmission, t, refraction, r, and scattering, s. As the wire was assumed to be non-scattering, the sample function was modelled simply as an

$O(t, r) = t\delta_D(r)$, where δ_D is the Dirac delta function; for the scattering samples, $O(t, r, s)$ was modelled as a non-zero centered Gaussian distribution, with t being incorporated into its amplitude.

M1 was positioned at ± 49.5 μm for the wire sample, as marked in Fig. 3.4 (a); the image scan was performed at a rate of 10μm per step and the exposure time was 190ms ($\approx$10mGy entrance dose). For the scattering sample, M1 was positioned at -53.0 μm; -34.5 μm and 41.0 μm; with the samples being scanned in 20 μm steps at an exposure rate of 100ms ($\approx$5mGy) per step.

3.1.2 Optimal sampling positions in Edge Illumination and beam tracking modalities

In order to retrieve multiple contrasts in a standard implementation of EI, it is usually necessary to acquire multiple images of a sample corresponding to different displacements of the pre-sample mask. More formally, the sample must be imaged at linearly independent (usually symmetric) positions on the IC, with each new position enabling the retrieval of a higher order contrast or *moment*, as defined by Modregger *et al.* [72]. Determining which sampling positions on the IC are best for accurate retrieval of sample parameters is a non-trivial exercise, and depends also upon the sample parameters. However, for quantitative single-shot methods, it is possible to examine, on a case-by-case basis, a retrieval algorithm's accuracy and precision numerically (where noise is present and controllable).

The individual pixel ICs - one for each of the pixels within the aperture of M2 and further, one pixel on each side of the aperture, so seven pixels in total - obtained using McXtrace were modified to account for the presence of various samples. The sample parameters were randomly generated such that transmission, t, was between 97% and 100%; refraction, r, from -5 μrad to 5 μrad and scattering signal, s, from 0 to 5 μm^2 - similar to the range of parameters encountered in the real experiment. This modification was enacted by a convolution of the ICs with a Gaussian defined as

$$O(x) = t \exp\big(\frac{-(x-r)^2}{2s^2}\big)/\sqrt{2\pi s^2}. \tag{3.2}$$

Noise was incorporated by multiplying the convolution output by a matrix that took the form of

$$((1-a) + 2a \times \texttt{rand}(7,10)), \tag{3.3}$$

where a was close to zero, and $\texttt{rand}(x,y)$ creates an $x \times y$ matrix of uniformly distributed values between 0 and 1. For each position of M1, the retrieval was called 10 times - once for each of the columns in the noise matrix - in order to obtain a spread of retrieved sample parameters whose “measurements” were affected by similar levels of noise. The aim of this procedure was to reduce the likelihood of encountering false positive or negative sampling positions in terms of retrieval performance. The retrieval algorithm used was identical to Eq. 3.1, with the accuracy of retrieved parameters being tracked for each position of M1, and was performed for both the EI and BT cases.

3.1.3 Monte Carlo model for comparison with beam tracking and single-shot retrieval

The experiment was recreated in a Monte Carlo environment called McXtrace [73]. McXtrace was originally developed as a ray-tracing software for x-ray optics, beamlines and interactions; it is interfaced with via a psuedo-C programming language, written by the code’s authors. The software is freely available with documentation for use through other platforms, such as MATLAB, and was adapted for EI use by Millard *et al.* [74]. The advantages of using a ray-tracing programme in this case are that it automatically includes Poissonian noise in the data and that it does not inherently rely on the projection approximation, which is important when considering scattering objects distributed over relatively large regions in three-dimensional space such as the cuvettes described above. If necessary, McXtrace can reproduce interference effects, however in this case and for EI in general, which is a non-interferometric technique, this faculty is not needed. One disadvantage is that, as a statistical model, if noise is to be minimised, the number of photons in the simulation must be increased, which increases the computational workload.

The masks were modelled one aperture at a time as pairs of three dimensional absorbing blocks, 1mm in depth and separated by 20 μm and 100 μm for M1 and M2, respectively. The monochromatic source was placed 147.5 m from M1 and photons were confined to travel in the 3D space bound by source and detector. The detector was modelled as a two-dimensional grid whose pixels were of equivalent size to those of the PCO.Edge. Local ICs were simulated by finely scanning M1 over a single period using a large number of photons; for the comparison with beam-tracking, the detector mask was removed and M1 scanned again, only over one pixel width instead of the mask period. Only one pixel was necessary in this simulated case as it is guaranteed that each pixel will respond in the same way, thus the beam profile can simply be extrapolated (if the simulated pixels are required to behave in the same manner as in the experiment, simple adjusting factors may be used for each of them until the measured response is equal to the simulated one). The point-spread function was included in all simulated data by convolving the raw output data with a Lorentzian curve of width parameter 0.8 pixels. This value was determined by considering a raw experimental image of the beam in the absence of a sample - the intensity profile across an edge of M2 was used to determine the line-spread function, which was then assumed to be symmetric in both directions. The best fit resulted from use of a Lorentzian of width parameter 0.8 pixels, which was also found to produce a good match between the simulated and measured ICs.

The Nylon-6 wire was modelled as a cylinder and photons that encountered it were adjusted for attenuation and refraction via the Beer-Lambert law and Snell laws, respectively. A step size of 10 μm was used for the wire scan and 5×10^6 photons of energy 50 keV were simulated, corresponding to an integration time of roughly 50 ms in the real beam.

The microspheres in gel were modelled as being inside a cylinder of water. Sphere centres were determined by a random co-ordinate map which was generated in MATLAB, and exported to a text file for reading by McXtrace. For simplicity, the volume density was set to 2.5% (approximately 10^8 microspheres / ml), with microbubbles randomly filling the volume and with the same size distribution as the measured one shown in Fig. 3.3 (b). Likewise for the wire, photons that interacted with spheres were refracted according to Snell's law. A scan step-size of 10.8 μm across the aperture of M1 was employed for the spheres, with each step simulating 1.5×10^7 50 keV photons (roughly 3300 photons per pixel), equating to an integration time of approximately 150ms. The refractive index data for the wire, water and the shell boundaries (acrylonitride) were acquired through the `xraylib` library programme [75].

3.2 Results and discussion

Figures 3.4 and 3.5 show the ICs, raw Nylon-6 wire intensity profiles and retrieved transmission and refraction for the two-frame (standard EI) and one-frame acquisition modalities (respectively) enabled by this setup. Both approaches result in a good image quality and agreement with theory, as seen by the match between the retrieved and theoretical profiles in parts (c) and (d) of both figures. Of note

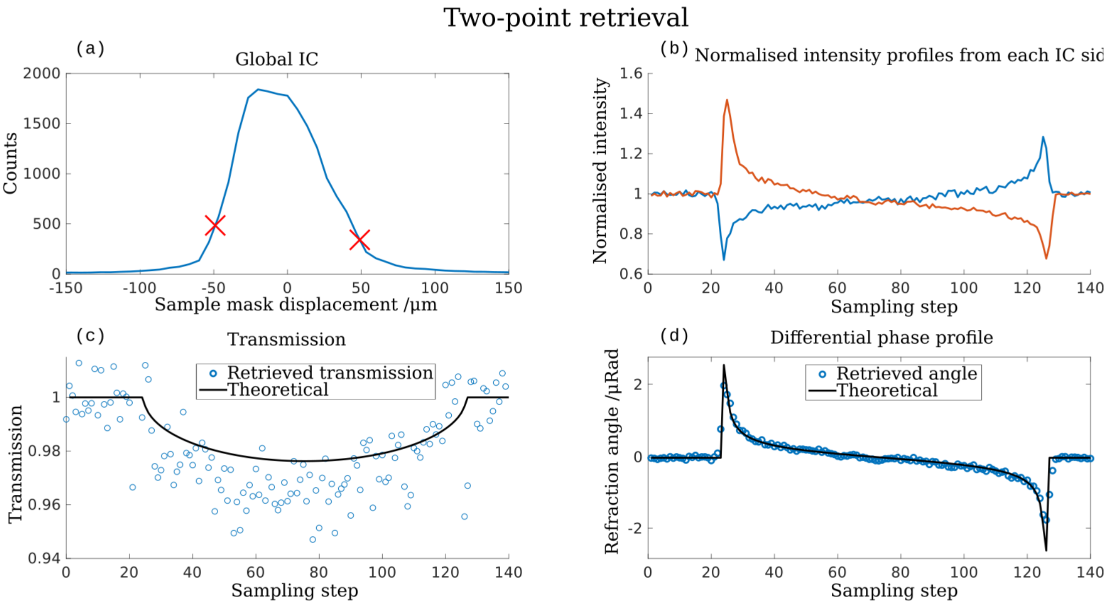

Figure 3.4: EI implementation for retrieval of the Nylon-6 wire using two input frames. (a) is the average IC, marked with the sampling points used; (b) displays the raw data profiles obtained by summing all pixels in the vicinity of an aperture; (c) and (d) show the retrieved and theoretical profiles for transmission and refraction, respectively.

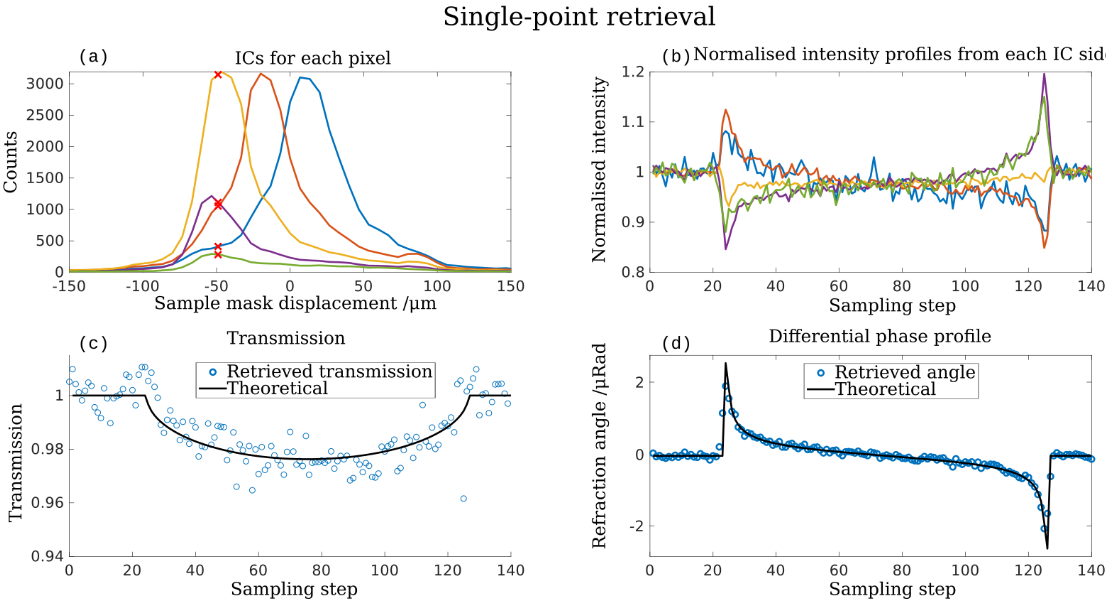

Figure 3.5: Single-shot EI implementation for retrieval of the Nylon-6 wire. (a) The individual pixel ICs, marked with the single sampling point used; (b) the normalised raw data profiles as recorded by each pixel within the aperture of M2; (c) and (d) show the retrieved and theoretical profiles for transmission and refraction, respectively.

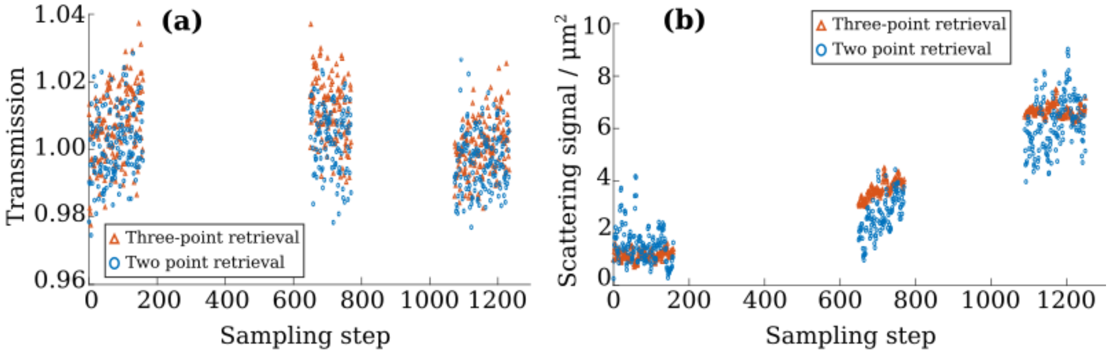

Figure 3.6: Retrieved transmission (a) and scattering (b) parameters of the different microsphere concentrations, as acquired via the individual pixel approach, which used two input frames, and the average IC approach, which used three frames. Relative microbubble concentrations are 1/3, 1/2 and 1 from left to right. Gaps between data groups skip the edges of the cuvettes.

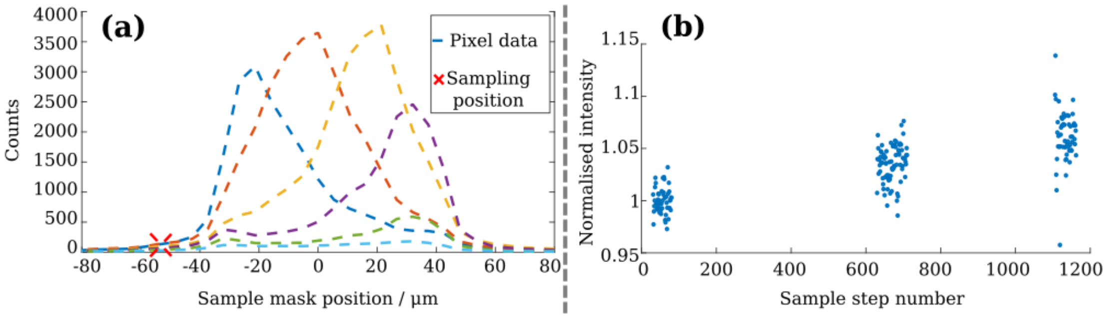

Figure 3.7: Alternative measurement of the dark field signal due to the different microsphere concentrations. (a) Shows the individual pixel ICs and the sampling position (red cross), indicating that the primary beam is almost fully obscured. (b) Shows the intensity measurements corresponding to each concentration, normalised to the mean of the lowest microsphere concentration.

is that, in the single-shot case, transmission has been retrieved with an improved accuracy, despite using only half the data set used in the two-frame case. This could be due to small displacements of M1 compared to it's nominal position, which may have affected the two-frame retrieval more than the one-frame case. Additionally, this retrieval provides direct access to the quantitative transmission and refraction angle, despite making no assumptions on sample homogeneity.

Three M1 acquisition points were used in the retrieval of the scattering microspheres using the global IC, with only two of these (inner) positions being used in the individual pixel case. The results are shown for each of the different microsphere concentrations in Fig. 3.6. The plots show good discrimination between the different concentrations in the dark field and poor discrimination in transmission. With each set of apertures having shifted ICs with respect to one another, it is possible to compare these retrieved signals with a dark field image of the microspheres that was acquired by pixels in an adjacent aperture - see Fig.3.7, where the primary beam falls completely on an absorbing section of M2. This method of measuring dark field signal is the same as described by Olivo *et al.* [76] and relies on the scattering "tail" being detected, i.e. only part of the scattering signal is integrated. For this reason, the dark field signals from increasing concentrations are seen to increase, though with less obvious distinction between the samples than in the previous figures (note the different y axis scales).

The results of the optimal sampling position study are displayed in Figures 3.8 and 3.9 for EI and BT modalities respectively. Both figures show that while transmission and refraction are consistently retrieved well for most sampling positions, the accuracy and precision of retrieved *scattering* values vary greatly according to where the beam is sampled. The variation in precision, or height of the error bars, as M1's position is varied, highlights how a given level of noise (Eq. 3.3: $a = 0.09$) impacts the retrieval performance in a non-uniform way; in both the EI and BT settings, the optimal sampling windows are found near $x = 2.3$ μm, where the beam is mostly centered on the pixel and far from the edges of M2. For various lower noise levels (not shown in the these figures), it was also found that the retrieval of scattering was most accurate at the IC peak positions. If the beam is positioned in the middle of the aperture, the EI system is effectively the same as BT (albeit in the specific case of the beam width being the same size as the pixel), as M2 has no impact on the measured intensity, thus the same levels of accuracy and precision is expected and indeed is shown in Figures 3.8 and 3.9 for transmission and dark field signals, though retrieval of refraction appears to

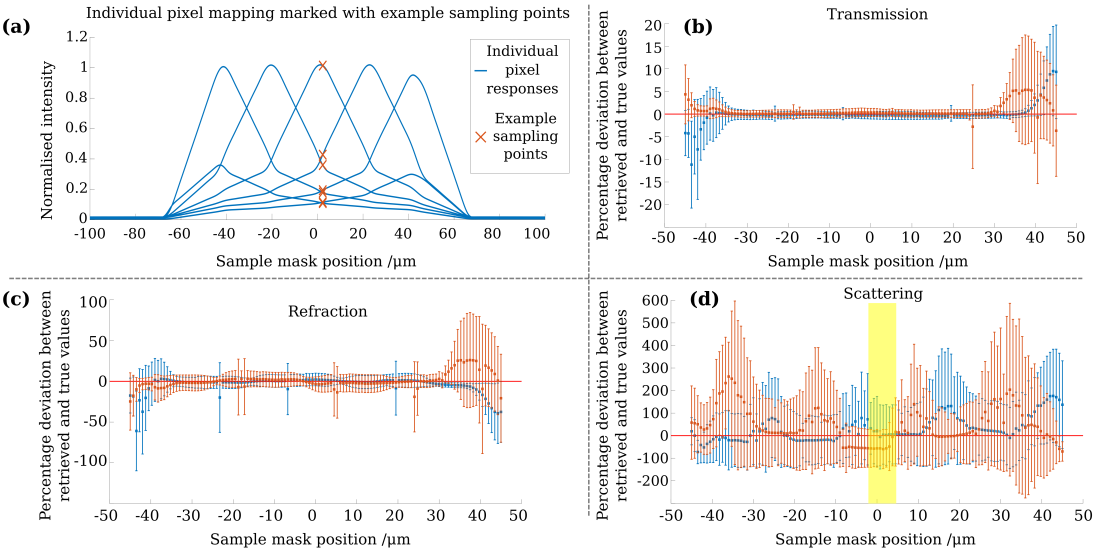

Figure 3.8: Testing of retrieval algorithm accuracy under single-shot conditions for different positions of M1 **with** a detector mask present. A set of sample parameters with positive and negative refraction angles are considered. Individual pixel ICs are shown in (a), with an example sampling vector marked; (b) - (d) show the accuracy (the distance from the average value to the zero-line) of retrieved values, and their precision (height of error bars) for the different possible positions of M1 relative to M2. The optimal sampling window for single-shot retrieval of scattering is highlighted in (d).

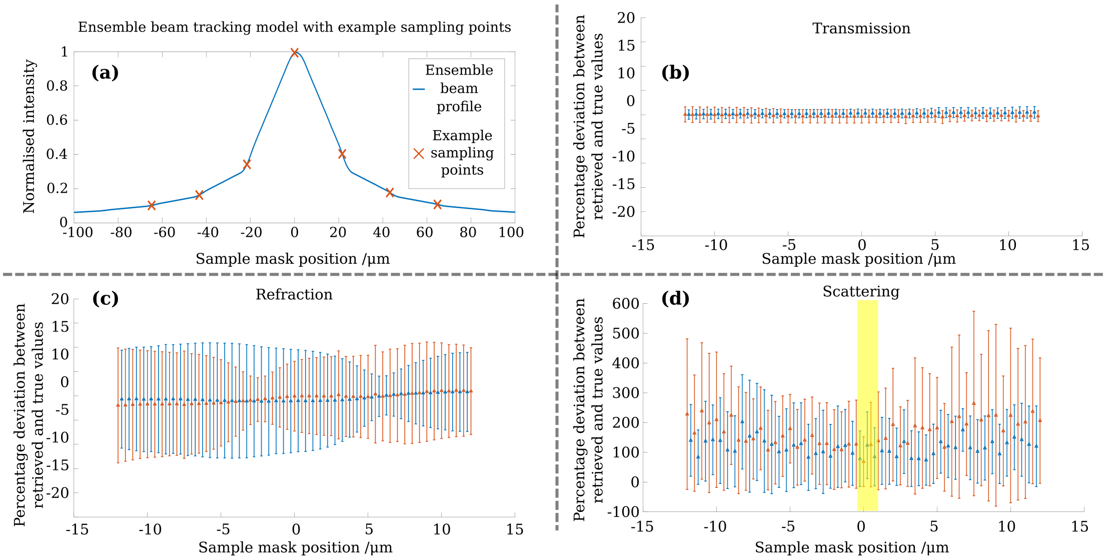

Figure 3.9: Testing of retrieval algorithm accuracy under single-shot conditions for different positions of M1 **without** a detector mask present - the BT modality. Sample parameters with positive and negative refraction angles are considered. The beam profile is shown in (a), with an example sampling vector marked; (b) - (d) show the accuracy (the distance from the average value to the zero-line) of retrieved values, and their precision (height of error bars) for the different positions of M1 relative to the centre of a pixel. The optimal sampling window for single-shot retrieval of scattering is highlighted in (d).

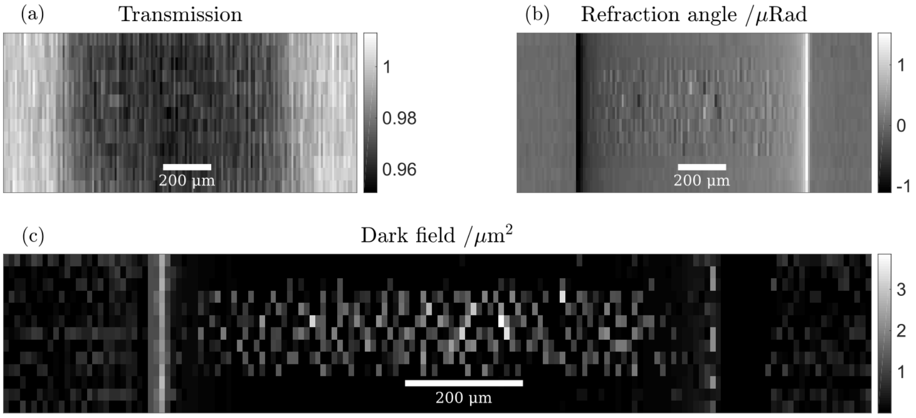

Figure 3.10: Single shot retrieval from simulated data of transmission (a), refraction angle (b) and dark field signals (c) at 50 keV. The sample is a cylinder of water, with a radius of 550 μm, with a 2.5% volume concentration of microspheres in the central region.

be more accurate in the EI implementation.

Considering that the scattering sample data used in the two-shot retrieval was acquired while M1 was positioned at -34.5 μm and 41.0 μm, Fig. 3.8 helps to explain why the spread of retrieved values in Fig. 3.6 was much greater in the two-shot case than for the EI-based three-shot scenario. The data in question comes from non-ideal sampling positions and is subjected to relatively high amounts of noise compared to the noise matrix used in the numerical study on retrieval accuracy.

3.3 Monte Carlo modelled single-shot dark field retrieval

As proof of concept for a single-shot retrieval, the virtual phantom described in Sec. 3.1.3, with M1 positioned at $x = 2.3$ μm and with the detector mask being present, was simulated. Fig. 3.10 displays the retrieved transmission, refraction and scattering signal of this phantom, with the microspheres only being present in the central region of the cylinder. The lack of dark field signal in the upper and lower regions of the cylinder confirm that the scattering signal is due to the spheres and not the water surrounding them.

The fewer-frame retrievals implemented here are possible because of the relatively large crosstalk between pixels, where pixel neighbours and next neighbours record $\approx 14\%$ and $\approx 4\%$ of a beam's primary intensity, respectively. For sufficiently large counts, these parasitic signals become significant enough to be considered as inputs for the retrieval. Indeed, as Lorentzians are characterised by long tails compared to Gaussians, subsequent pixels record similar levels of intensity as the next-neighbour pixels, which increases the number of possible inputs to the retrieval. With the optimal sampling position found to be in the centre of the M2 aperture, all of the dose deposited within the sample is used in image formation, which is the most efficient use of photons possible in EI.

3.4 Chapter summary and conclusion

The implementation of EI XPCi in this chapter allows for direct comparison between high-dynamic range EI and beam-tracking modalities, and enables single-shot retrieval of transmission, phase and dark-field signals. The approach takes advantage of crosstalk to form uniformly separated IC functions within the detector mask aperture. Data from these pixels represent complementary sampling points which can then be used to numerically determine the transmission, average refraction angle and dark field signals to a good degree of accuracy.

The comparison between EI and BT modalities shows that for the retrieval of transmission and refraction contrasts, BT is as stable and accurate as EI, while depositing less dose to the sample for a given background intensity level (as M2 is not present to reduce the overall number of photons). However, for retrieval of the dark field signal, multiple sampling points vastly benefit the precision of dark-field imaging and, considering that the EI modality allows for direct imaging of this contrast, it may be the preferred option.

Upon testing, it was found that the optimal position of the pre-sample mask for single-shot retrieval was also the most dose-efficient; namely the centre of the detector mask aperture. Since this position makes the mask-based setup equivalent to the BT setup, it is advisable that, if only single-images are to be taken, the latter setup be used, as it has more relaxed alignment requirements.

The ability of EI to detect *and distinguish* between dark-field signals of varying concentrations of microspheres at high energy implies that the same should be possible in a polychromatic lab setting, which is the focus of the next chapter.

4

Lab-based high energy XPCi

4.1 Chapter introduction and motivation

Having demonstrated the possibility to retrieve phase and dark field signals at high energy using synchrotron radiation, the aim of this chapter's study is to test this ability in a laboratory setting, where the extended source, polychromatic beam and larger EI masks present new challenges in signal retrieval. Models of this more complex experimental system must be benchmarked against changing spectra such that, once validated, they can be used to predict outcomes in situations that could not be tested in a lab (e.g. clinical settings).

The chapter begins by listing the equipment and methodologies employed in two experiments that compare the signal to noise ratio (SNR) of wires imaged in air and in water, at constant dose, with increasingly filtered tungsten spectra. Various concentrations of microspheres in ultrasound gel and a porous sponge, chosen as scattering samples, are then also imaged through different filter thicknesses for scenarios of constant dose and constant accumulated photons. The results for both SNR and dark field signal strength are then presented along with an analysis of differences between the two systems, and which of these differences lead to key improvements in image quality. Finally, a wave-optics model of the system is used in an attempt to recreate the wire experiments. The experiments involving “thinner” masks are recreated successfully, however attempts to simulate experiments that use thicker masks fail due to limitations of the model which are discussed and developed in the next chapter.

4.2 Equipment and methods

4.2.1 Source characterisation and KERMA measurements

A Rigaku MultiMax-9 source, with a tungsten rotating anode and take-off angle of 6° was used. The voltage was set to the maximum value of 60 kVp and the current to 20 mAs, which was the maximum current allowed at that voltage, in all experiments but for the dose rate measurements behind the Hamamatsu sample mask, where the current was set to 10 mAs. A gold-plated pinhole of diameter 75 μm was placed 13 cm downstream of the source shutter (the closest practical position), and a Photonic Science (Mountfield, U.K.) CCD camera, with pixel size 4.54 μm, was placed 204.5 cm from the shutter along the optical axis (chosen to be as close as possible to the standard EI distance of source to detector, which is 2 m). The detector has 1:1 bonding between pixels and optical fibres and uses a gadolinium oxysulphide scintillator, whose nominal density is 3 mg/cm^2. The resulting image and horizontal profile of the source are shown in Fig. 4.1. The magnification of the system, 15.7, was high enough to justify the approximation that image blurring due to the detector PSF was negligible in comparison with blurring due to the source, meaning that the image is an accurate magnified representation of the source spot. As the size of the pinhole is comparable to the source profile, however, it *was* necessary to account for image blurring due to the pinhole; this was achieved by demagnifying, then deconvolving the source profile

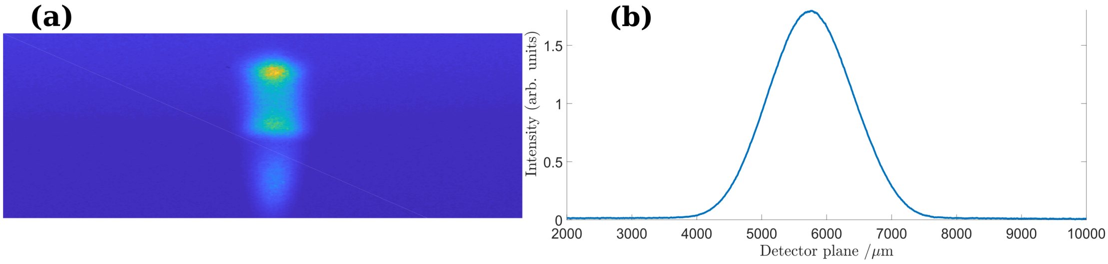

Figure 4.1: (a) Image of the source used; (b) shows the horizontal profile before deconvolution with the pinhole.

with a top-hat function whose width was 75 μm. The result was then fitted with a Gaussian:

$$a\exp\left(\frac{(x-b)^2}{2\sigma_{\text{source}}^2}\right)/\sqrt{2\pi\sigma_{\text{source}}^2}, \tag{4.1}$$

whose width parameter was found to be $\sigma_{\text{source}} \approx 31$ μm, though we note that, in general, σ_{source} depends on the angle from which the source is viewed.

The KERMA was measured using a PTW soft x-ray ion chamber (TW30010-1), calibrated by PTW-Freiburg with a rated uncertainty of 1.1%. The chamber was placed in the sample position, approximately 1.6 m from the source, held in place by a retort stand and clamp, then connected to an electronic readout, the UNIDOS E, by an RS232 cable. With the source active, the chamber integrated dose over ten second intervals three times, with the readings then being averaged. The beam was increasingly filtered by placing sheets of dural - an aluminium based alloy containing up to 5% copper and some amount (less than 1%) of manganese, magnesium, iron, silicon, zinc, titanium and possibly chromium - in front of the source window, in increments of 0.5 mm and 1 mm. One 300 μm thick sheet of high-purity copper was also available, and was used as a benchmark filter, as copper filters are routinely used in clinical x-ray systems [77, 78]. The measurements were then repeated with two different sample masks (designed for use with either the Hamamatsu or Pixirad detector) placed between source and ion chamber to determine the true dose incident on the sample rate in the EI system. The two

	Hamamatsu Mask	Pixirad Mask
Manufacturer	Creatv Microtech	MicroWorks
Nominal gold thickness	150 μm	300μm
Period	78 μm	48 μm
Aperture size	23 μm	12 μm
Substrate	Graphite (500 μm)	Silicon (525 μm)
Aperture filling	Epoxy resin	SU-8
Appropriate detector	Hamamatsu Flat Panel	Pixirad Photon counter

Table 4.1: Specifications of masks used in dose and SNR measurements.

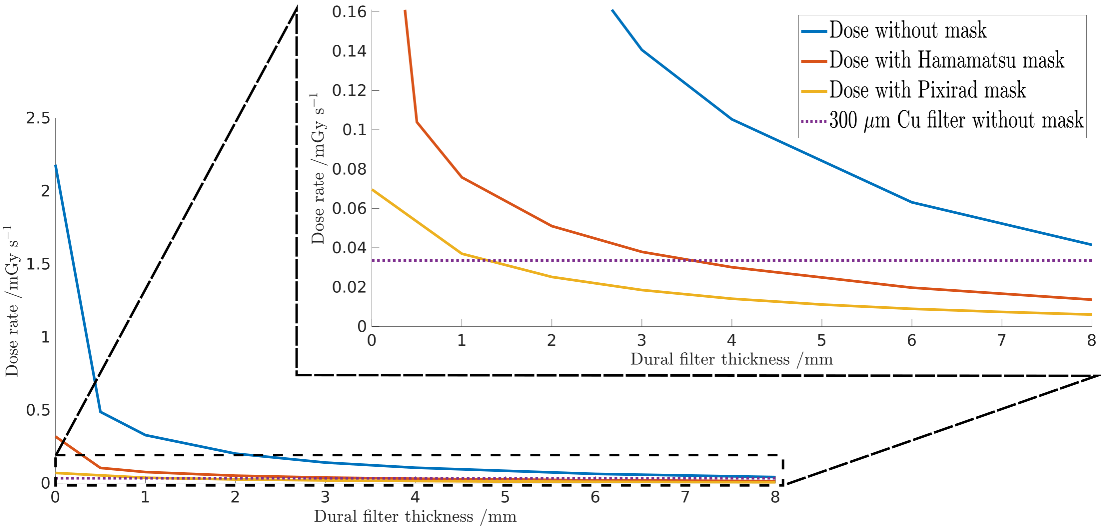

Figure 4.2: Measured dose rate of 60 kVp tungsten anode source, operated at 10 mAs through increasing thicknesses of dural filter, with and without different sample masks preceding the ion chamber.

masks were of different designs and their specifications are presented in Table 4.1, while the dose measurements themselves are shown in Fig. 2.18. Each curve in the plot, but for the dose rate measurements behind the Hamamatsu mask, where the current was 10 mAs instead of 20 mAs, was scaled down by a factor of 2 in order to portray dose rates due to equivalent amounts of flux. Of note is the fact that, despite the masks having a large difference in their gold thicknesses, the dose rate behind each of them is very similar after filters are introduced.

4.2.2 Detectors

A "standard" double mask EI setup was used for both experiments in this chapter. The sample and pre-sample mask were placed 1.6 m from the source, while the

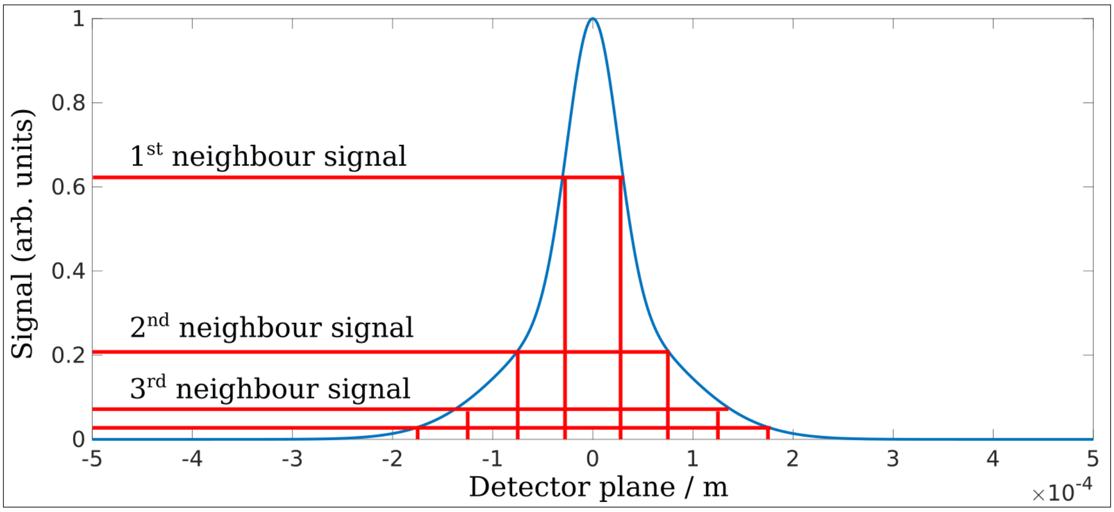

Figure 4.3: Measured PSF of the Hamamatsu detector with next-neighbour intensities marked; for ths detector, ceasium iodide is grown in columns directly onto the detector.

detector and detector mask were placed a further 0.4 m downstream. Different detectors were used in the experiments: a Hamamatsu flat panel CMOS detector (C9732DK-11) and a Pixirad photon counting and energy resolving detector. The Hamamtsu features a CsI scintillator and 50 μm pixels and integrates the number of visible light photons produced by x-rays interacting with the scintillator; its energy response function is shown in Fig. 2.19 (b). The PSF of the detector had already been characterised by the procedure described in Sec. 2.6.3.2 and the result is shown in Fig. 4.3. In order to minimise the impact of the relatively large PSF, the Hamamatsu masks had a line-skipped design, meaning the masks illuminated every other pixel column. Before acquisitions, “dark” images, taken when the source was shuttered and the detector is reading only electronic noise, were acquired for subtraction from any following images.

The Pixirad detector consists of two modules containing 402×512 pixels in each; as the modules are slightly rotated with respect to one another, only one was used for the EI experiments. Pixirad, which uses a cadmium telluride sensor layer, is capable of applying some degree of spectral discrimination on the counted x-rays. A lower energy limit of 10 keV was selected, with photons below this threshold not contributing to any images acquired. The upper energy limit was set to 70 keV in order to reject any contributions by electronic pileup in the pixels. A low operational temperature of -20°C (achieved via Peltier cooling) was used to reduce the electronic noise of the detector and a constant flow of dry, inert air was used to reduce the humidity on the detecting surface, thus preventing the formation of water droplets or ice crystals. The sensor layer material is cadmium telluride and the crosstalk between pixels, of size 62 μm, was assumed to be negligible.

4.2.3 Samples, acquisition processes and retrieval methods

A selection of wires were used in both experiments, with the Pixirad experiment also utilising samples that would generate dark-field signals, such as microspheres and a porous sponge. Some wires were imaged through air and others through water, with the various combinations being listed in Table 4.2.

For wire imaging, an IC was acquired immediately before the experiment and the half-maximum positions were determined. The procedure was to then acquire flat images (no sample in the beam) at these IC points, with 2× the exposure time, then wires, then flats with 2× the exposure time again, before finally being averaged. Flat images, which do not contribute to the dose to the sample, are used to correct for variations in pixel response and beam inhomogeneities; the increased exposure time was to minimise the impact of Poissonian noise in the flats on the sample images. In each filtration setting, the exposure time for the sample images was determined such that the total dose from imaging would be constant.

The procedure for imaging wires through water was slightly different in each experiment. In the Hamamatsu setup, the wires were affixed to a frame and placed in a sealable, thin plastic bag. Upon being filled with water, the bag's surface became curved, thus leading to a non-uniform background. As it was impossible

Host medium	Wire material	Radius /μm	Hamamatsu	Pixirad
Air	Maxima	150	✓	✓
Air	PEEK	72	✓	✓
Air	PET	52	✓	
Air	PET	85	✓	
Air	Boron with tungsten core	105; 14	✓	✓
Air	Sapphire	125	✓	✓
Air	Nylon	50		✓
Water	PMMA	1520	✓	✓
Water	Teflon	500		✓
Water	Nylon	675	✓	✓
Water	Hollow cannula	500	✓	✓

Table 4.2: Wires used for imaging in the Hamamatsu and Pixirad experiments. Maxima, PEEK and PET are all plastics, with Maxima being a trademarked material used in the production of fishing lines. The hollow cannula is a 20 Gauge B Braun product and consists of a PUR shell, lined with thin strands of iron.

to construct another water host of the same dimensions, flat field images had to be acquired in air, meaning the spectrum was slightly different between sample and flats. To avoid this non-uniformity in the Pixirad version of the experiment, wires were affixed to a rod which was placed inside a polypropylene box of 1 mm wall thickness, which was then filled with water. A separate polypropylene box, of the same dimensions, was filled with water and placed next to the sample box so flat field images and ICs could be acquired with the same spectra as the sample images. Aside from using the same spectra, flats and ICs were acquired in the same way as described above.

In both experiments, the dose per dithering step was kept constant for different thicknesses of the dural filter by varying the exposure time and number of frames. The “in-air” samples accumulated an entrance dose of 2.45 mGy per retrieved dithering step and the “in-water” samples a dose of 13.7 mGy per retrieved dithering step. The number of dithering steps varied between experiments, with the Hamamatsu having ten and five for the in-air and in-water samples, respectively. The Pixirad experiment had a finer sampling rate, in which twelve dithering steps were acquired throughout; this meant there was a finer sampling of, and therefore sharper, refraction peaks. Lastly, when imaging scattering samples, only one dithering step was used, as sampling was not a concern. For each experiment, filter thicknesses of 0 mm, 2 mm, 4 mm and 8 mm dural were employed, however some acquisitions were not successful and so the unfiltered Hamamatsu in-air and Pixirad 4 mm dural in-water measurements are missing from the analysis.

The two types of scattering sample used in the Pixirad experiment were a cuboid sponge (commercially available "Wunderschwamm") - approximately 1 cm thick and chosen as a weakly absorbing and highly porous material - and varying concentrations of microspheres. The microspheres were prepared and diluted using the method described in Sec. 3.1.1, but with a wider range of relative concentrations: 1, 0.5, 0.1, 0.005 and 0.01 (with 1 being the same concentration of 2.3% by volume, as before). The sponge was imaged from within a polypropylene box filled with air and then water, and acquisitions were made at three symmetric points on the ICs: the half-maximum and peak intensities. The microsphere concentrations were imaged though 4.1 mm thick cuvettes at five symmetrically located points on the ICs, shown in Fig. 4.4. Dural filter thicknesses of 0 mm, 4 mm and 8 mm (and for 2 mm in the case of the sponge) were used in imaging these samples and for each filtration, multiple frames were acquired in the sampling positions such that, in each case, the average number of counts was approximately constant. This meant that the overall noise was kept constant if the full data sets were used, and by using a subset of frames in the less filtered cases, images at a constant cumulative dose of 2.4 mGy for the microspheres, and 1.4 mGy and 7.2 mGy for the sponge in air and water, respectively, could also be obtained. Having access to both constant noise and constant dose data sets allows us to observe how noise affects the spread and accuracy of the retrieved dark field signals.

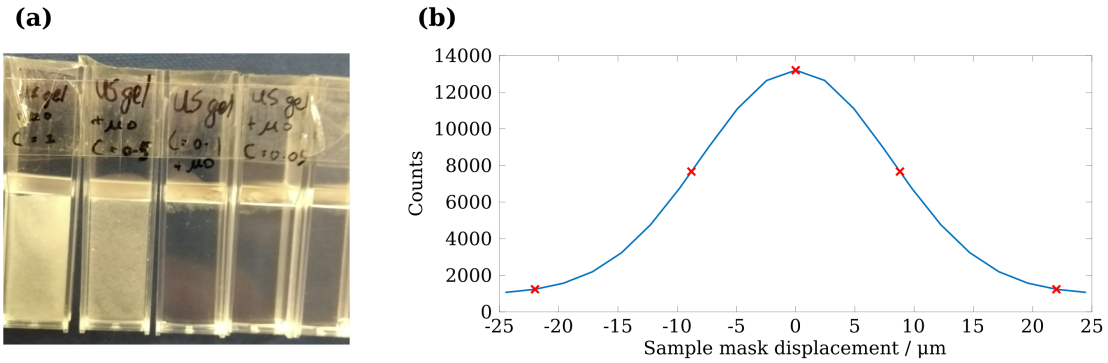

Figure 4.4: (a) Varying concentrations of microspheres inside cuvettes and (b) the IC sampling positions used when imaging.

To retrieve transmission, refraction and dark field signals, ICs corresponding to individual pixels were fitted according to the equation:

$$F(a,b,c^2,d,x) = a\exp\Big(\frac{-(x-b)^2}{2c^2}\Big)/\sqrt{2\pi c^2}+d, \tag{4.2}$$

where F is the function to be fitted, with (a,b,c,d) being coefficients to be determined and x is the vector of sample mask positions used in acquiring the IC. This equation differs from Eq. 4.1 only by the parameter d, which encapsulates the IC offset intensity due to mask transmission and any other background signals. Sample images were normalised by appropriate flat fields and for each sampling position, the values were scaled to the fitted IC values such that, in background areas, they lie on the curve. A least-squares approach was then used to retrieve the sample absorption, refraction and scattering i.e.

$$\chi(t,r,\sigma) \xrightarrow{\text{Minimise}} \sum(Y^2 - t\times F(a,b-r,c^2+\sigma^2,d)), \tag{4.3}$$

where Y is sample data vector and F is the fitted IC function.

4.2.4 Spectrum and wave-optics based modelling of Edge Illumination

In order to model the system, knowledge of the spectrum used in the experiments is required - both in the filtered and unfiltered cases. The TASMICS (tungsten anode spectral model using interpolating cubic splines) software, developed by Hernandez and Boone [79], was used to simulate the unfiltered spectrum. TASMICS was created through Monte Carlo modelling of electron interactions with a tungsten anode, then measuring the distribution of x-ray energies this produces. The software is made available as an Excel spreadsheet and was obtained upon request from the authors.

A distinguishing feature between the source modelled in TASMICS and the one used here is the difference in take-off angles, with the modelled angle being 12° and our source having an angle of 6°. This difference can be corrected by filtering the model spectrum by a small amount ($\approx$ 2-4 μm) of tungsten to account for the extra self-filtration of our source. In the figures of this chapter, “unfiltered” spectra refer to the TASMICS output after this initial tungsten anode self-filtration has been taken into account. The hardening of the beam due to dural filters was calculated using data from the `xraylib` library through a MATLAB interface, and approximating the material as being 95% aluminium and 5% copper. The unfiltered and filtered spectra are shown in Fig. 4.5.

The wave optics simulation framework was developed in house by Vittoria *et al.*, [56] and makes use of the Helmholtz propagator (Eq. 1.13), with convolutions being implemented via successive fast Fourier transforms. The masks in this model are constructed in two steps, the first of which is the template: a convolution of a

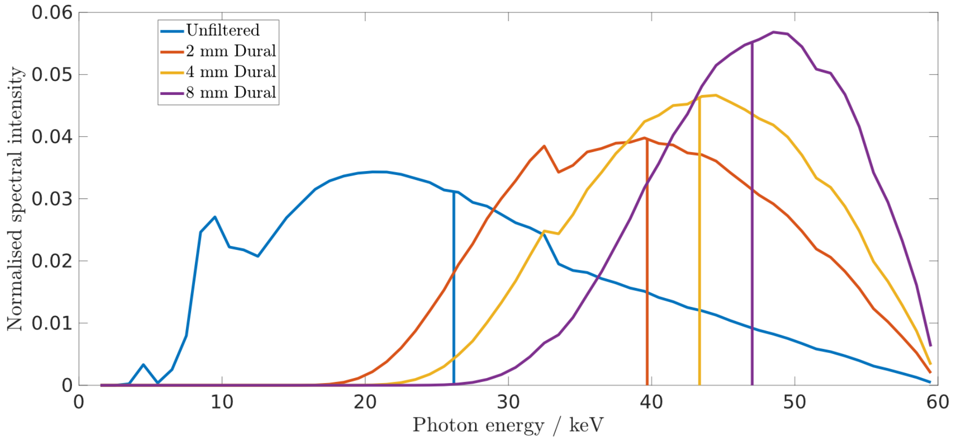

Figure 4.5: TASMICS tungsten spectra used in reproduction of experiments (3 μm W self-filtration included): unfiltered and filtered by 2 mm, 4 mm, and 8 mm of dural. Vertical lines indicate average beam energies.

top-hat function with a sequence of Dirac delta functions, i.e.

$$\begin{aligned}\text{Mask template} &= \text{Top hat}(x) * \text{Dirac delta sequence} &(4.4)\\ &= \texttt{heaviside}(w/2 - |x|) * \sum_{a \in N} \delta(x - ap), &(4.5)\end{aligned}$$

where w is the aperture width, p is the mask period, a is an integer and N is the number of apertures. The second step is, for regions where the template is zero, to replace these values with those of the mask transmission: $\exp\left(-\frac{2\pi}{\lambda}\left[i\delta_{\mathrm{Au}} + \beta_{\mathrm{Au}}\right]t_{\mathrm{Au}}\right)$, with t_{Au} being the gold thickness. In this way, the mask is constructed efficiently with the apertures remaining fully transmitting.

Samples are simulated using the projection approximation: the object's complex phase function multiplies the wavefront after the sample mask, which is then propagated to the detector plane. To implement a polychromatic simulation, the monochromatic simulation is performed for each 1 keV energy bin and then combined in a weighted sum, with the weights being the spectral intensities. A Gaussian source of width $\sigma_{\mathrm{source}} = 31$ μm, as previously measured, was used in simulations and was found to produce ICs whose widths were similar to those measured experimentally.

For each version of the experiments listed above, simulations are called using the nominal parameters for mask thickness, sample properties and filter thicknesses. In the Hamamatsu case, the spectra were pre-filtered by 1 mm graphite (total thickness of mask substrates) and multiplied by the energy response function. Spectra used in modelling the Pixirad experiments were pre-filtered by 1.05 mm silicon (total thickness of mask substrates). Illumination curves were simulated using the same procedure as in experiment: translation of the sample mask in an orthogonal direction to the apertures over one period. The ICs are produced first, followed by the wires and both are then quantitatively compared to their experimental counterparts. The modelling approach here is to reproduce mixed signal intensity profiles due to sample absorption and refraction, or in other words, to produce profiles equivalent to those obtained experimentally *before* processing, as seen through the different filter thicknesses.

4.3 Experimental results and discussion

The SNR for transmission and refraction of the wires in both setups, air and water, is displayed in Fig. 4.6. For ease of reading, this section is subdivided into distinct subsections for the SNR measurements corresponding to transmission and refraction, in air and in water.

4.3.1 Transmission of wires in air

Retrieved transmission profiles for both detectors are shown in Fig. 4.7. Weakly absorbing wires, such as PEEK and PET, have transmission SNRs less than 5 (below the Rose criterion), while the boron wire, with its inner tungsten core, shows a strong absorption signal that benefits from the increased sampling provided by dithering. The overall trend in this case is that SNR decreases slowly

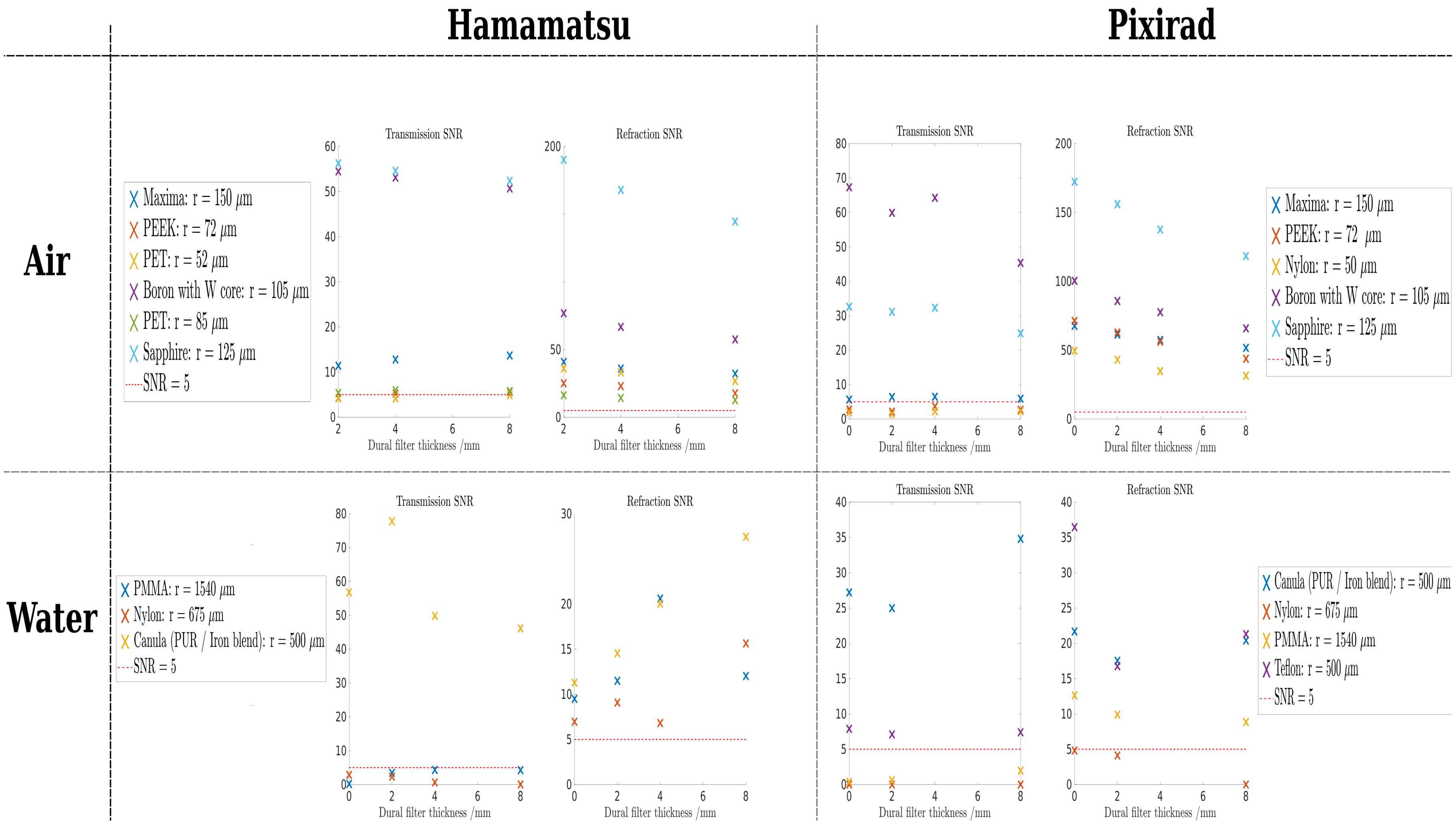

Figure 4.6: Collection of signal to noise ratio plots for wires imaged through air (top row) and water (bottom row); left and right columns correspond to measurements from the Hamamatsu and Pirixrad detectors, respectively. Dose delivered to the wires was constant for all in-air experiments (2.45 mGy / dithering step) and all in-water experiments (13.7 mGy / dithering step.).

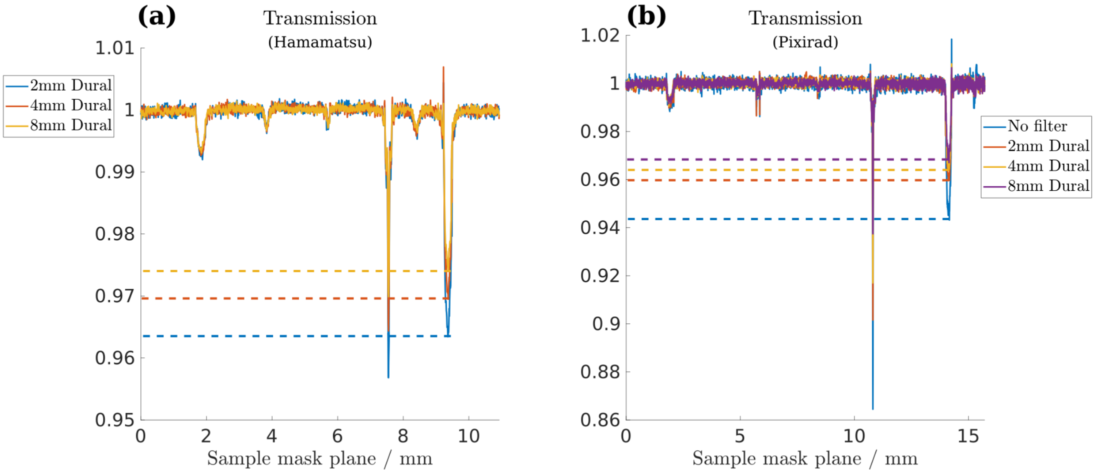

Figure 4.7: Hamamatsu (a) and Pixirad (b) detector measurements for retrieved transmission wire profiles for varying filter thicknesses, averaged over 20 vertical pixels. From left to right, the wires in (a) are maxima, PEEK, PET, boron with tungsten core, PET and sapphire; in (b), they are maxima, PEEK, nylon, boron with tungsten core and sapphire. The dashed lines indicate the decreasing signals for the sapphire wire as the average energy increases.

with increasing filter thickness. This is only valid, however, for the wires that exhibit sufficient absorption signals in the unfiltered case, as no clear trend can be discerned when considering these weakly absorbing wires against increasing filter thickness. That the transmission signal of given wires is quantitatively different between the detectors is a result of:

- The increased sampling in the Pixirad case (particularly for the 14 μm tungsten core in the boron wire); this has an associated dose increase of 20%;
- The different energy responses of the two detectors, with the Hamamatsu energy response increasing the effective energy and thus measuring lower signals compared to those measured by the Pixirad detector.

4.3.2 Transmission of wires in water

In both detectors, the cannula with iron thread results in significant absorption contrast for each filtration. Other wires, however, are mostly below the Rose criterion - even the PMMA wire, whose diameter is greater than three millimetres. This low SNR is mostly due to the high noise value surrounding the wire, which

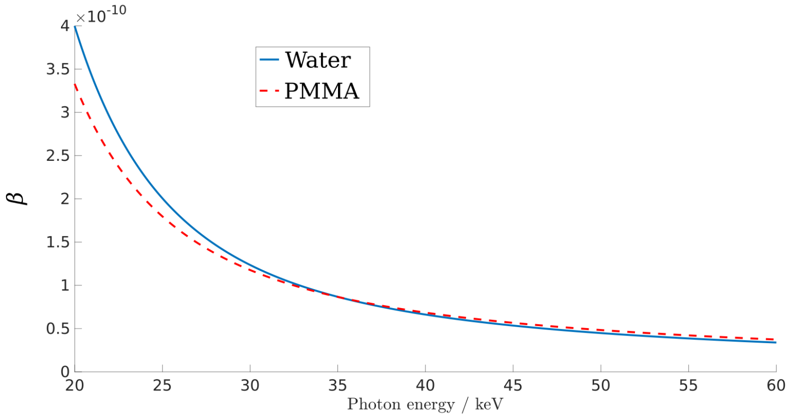

Figure 4.8: Attenuation coefficients of PMMA and water as a function of energy; attenuation of water becomes greater at approximately 35 keV.

is faintly visible in the full image; the absorption contrast of PMMA actually decreases and *inverts* before increasing between 4 mm and 8 mm dural filtration. The reason for this inversion is that the β for PMMA and water intersect at approximately 35 keV, as shown by Fig. 4.8; that the contrast *increases* is due to the difference between β_{PMMA} and β_{H2O} increasing with energy. As teflon (imaged only in the Pixirad experiment) is the only other wire whose SNR is above the Rose criterion, no clear conclusions may be drawn regarding the SNR trend in these cases. Further, as the Hamamatsu experiments used different spectra for ICs and flats compared to sample images, these data sets are particularly difficult to draw conclusions from since the nature of the noise in these settings will be different. The reason for this is that, as the detector energy response increases with photon energy, beam hardening due to water means that noise is more correlated in the sample images (i.e. smoother) than in the flats.

4.3.3 Refraction profiles of wires in air

Retrieved refraction angles for the various wire profiles are shown in Fig. 4.9. The refraction SNR for the Hamamatsu and Pixirad data is, on average, more than five times and ten times greater than the transmission SNR, respectively. As several of these wires were below the Rose criterion in the transmission plots, this figure

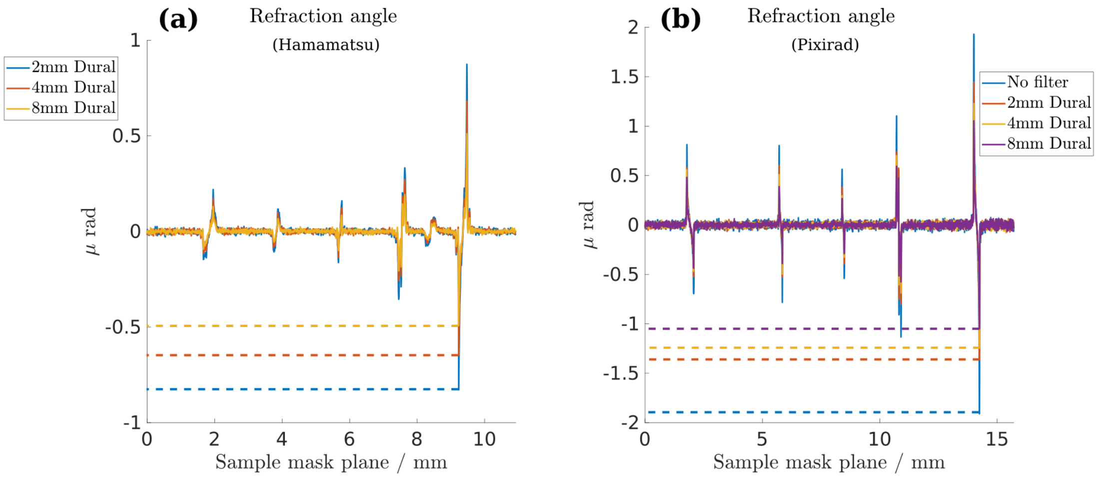

Figure 4.9: Hamamatsu (a) and Pixirad (b) detector measurements for retrieved refraction angle wire profiles for varying filter thicknesses, averaged over 20 vertical pixels. From left to right, the wires in (a) are maxima, PEEK, PET, boron with tungsten core, PET and sapphire; in (b), they are maxima, PEEK, nylon, boron with tungsten core and sapphire. The dashed lines indicate the decreasing signals for the sapphire wire as the average energy increases.

shows how significantly the image contrast is improved by the EI system. The overall trend for refraction SNR in air for constant dose is similar to that of the transmission SNR in air: decreasing with increasing filter thickness, though with a smaller average gradient.

4.3.4 Refraction profiles of wires in water

Fig. 4.6 shows clearly how wires with only slight absorption contrasts in water benefit from phase enhancement, with several of the wires becoming “visible” in both experiments (SNR $\geq$ 5) upon retrieval of the refraction angles. For the Hamamatsu experiments, which used flat images taken through air (thus using softer spectra), the refraction SNR of wires in water for constant dose increases with increasing filter thickness. For the wires measured with Pixirad, where the flat images used the same spectra as the sample images, the trend is either decreasing or approximately constant SNR with increasing filter thickness.

4.3.5 Noise in images of constant dose

In order to better understand the trends described so far, it is useful to consider the noise separately from the wire signals. Fig. 4.10 shows how the noise (standard deviation of the background, relative to the mean) decreases with increasing filter thickness as the dose is kept constant and each line is corrected by flats of the same spectra (flats are assumed to be noiseless relative to the sample frames used). In the Hamamatsu case, these "same-spectra" flats through water were obtained by considering a small region of interest (RoI) and using frames from different dithering steps of the sample images while ensuring that the sample was far from the RoI. The variation in water thickness due to the curving host medium was assumed to be negligible over the dithering span of 50 μm. Missing data points for the unfiltered Hamamatsu in-air and Pixirad 4 mm dural in-water experiments were obtained by using data from incomplete or failed acquisitions - usually due to crashing of the detector software or failure of the source cooling. The total dose used in determining these noise variations was comparable for the in-air and in-water settings.

Taken together, Figures 4.6 and 4.10 therefore indicate that the wires' contrasts *in air* decreases at a faster rate than the noise as the average energy of the beam increases. In water, however (and in the Hamamtsu measurements in particular, where the flat field spectra was different from the sample's), the wires' contrasts are decreasing at a rate less than or equal to that of the noise in the background. This difference in the behaviour of SNR must therefore be due to the difference between the wires' absorption and refraction parameters compared to those of the background: as energy increases, the difference between wire and water can reach a minimum and then increase depending on the material.

The key point is that when imaging weakly absorbing materials in air, shorter

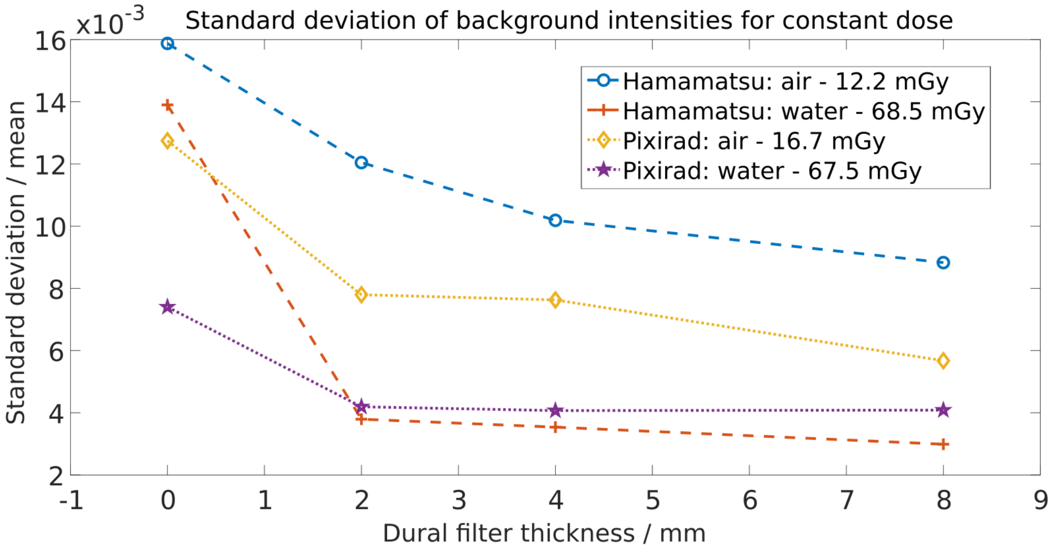

Figure 4.10: A dimensionless measure of standard deviation divided by the average background intensity (which differs between all settings) for increasing dural filter thickness and constant dose. The lines refer to measurements taken in air and water by both the Hamamatsu and Pixirad detectors; with the pixel responses being normalised by flat field images acquired through the same backgrounds of air and water.

acquisitions at low energy lead to a high SNR, whereas if imaging through water, the reduction in noise obtained by exposing the sample for a longer time and using a higher energy is a more effective strategy. For sources with a greater brilliance than the one used for these experiments, this higher exposure would not necessarily require a longer time in the beam - the longest acquisitions for these experiments, through 8 mm of dural, were 560 seconds per dithering step using the Pixirad detector, and 252 seconds per dithering step with the Hamamatsu.

4.3.6 Scatterers and discussion of dark field signals

Comparing absorption and scattering contrast is a useful way of visualising the benefits of dark field imaging, however in the case of the sponge, the transmission signal was consistently less than 1%, and so Fig. 4.11 shows only the retrieved scattering signal for the sponge in air and in water for different dural thicknesses. The data was taken by considering a 20×130 region of pixels within the sponge shadow and using their mean and standard deviation as the central points and

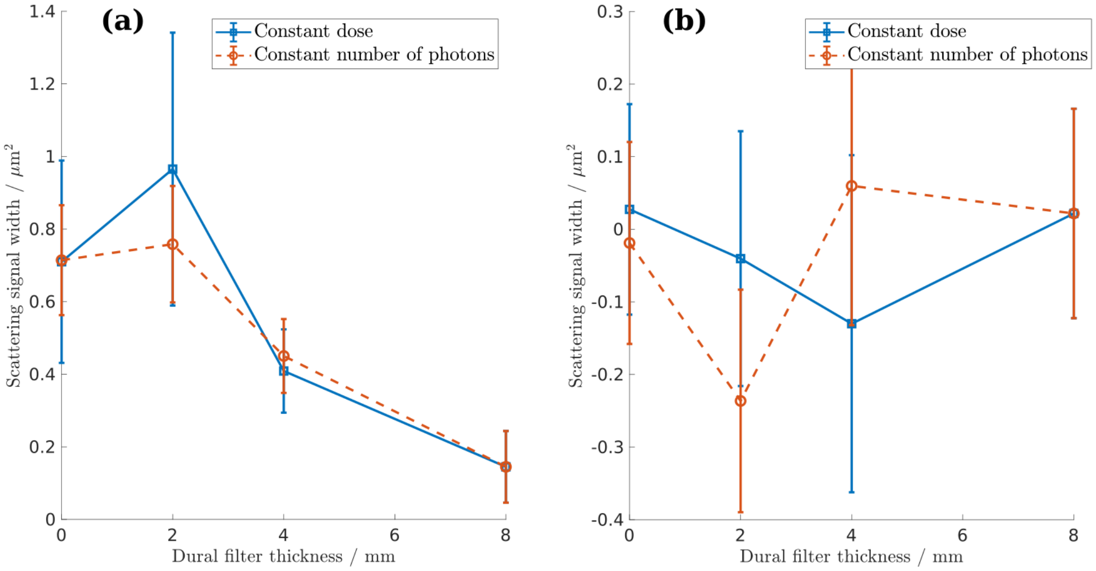

Figure 4.11: Retrieved scattering signals for sponge in air (a) and in water (b) through increasing dural filter thicknesses. Constant dose (solid blue lines) of 1.4 mGy and 7.2 mGy for air and water measurements were used, and the dashed red lines correspond to constant cumulative photon counts, as measured by the Pixirad detector.

uncertainties in the figure. In air, the scattering signal changes noticeably with increasing filter thickness, increasing slightly between 0 and 2 mm dural filtration, then decreasing. In water, however, the scattering signal is almost nonexistent and this persists with increasing filter thickness; nor does increasing the photon statistics have any discernible impact. The sponge becoming near-invisible in the dark field regime as it is immersed in water illustrates the difficulty in detecting fine structures when immersed in a medium with a similar value of δ.

The retrieved transmission and dark field signals for the different microsphere concentrations are shown in Fig. 4.12 (a) - (b) and 4.12 (c) - (d) for constant dose and constant noise, respectively. For each concentration, a small region of pixels near the middle of each cuvette was selected, with their average and standard deviations being used as the central points and uncertainties in the measurements. In both cases, the absorption and scattering signals decrease as the filter thickness increases, with the absorption signals decreasing in a consistent manner for all of the concentrations. While the error bars for transmission measurements are overlapping in some cases, the average transmission of concentrations 1 and 0.1 are almost identical, with the same being the case for concentrations 0.5 and 0.05. The average transmission of the 0.01 concentration is between those of the two pairs. As the filter thickness increases, these groupings of average transmission become slightly less apparent.

Scattering from the different concentrations decreases with increasing filter thickness also, while the average signals they produce have a relatively large spread, with lower concentrations generating higher signals in some cases. This is consistent in both the constant noise and constant dose cases, with the size of the error bars at the lower filtration settings being the most obvious change between constant dose and constant noise plots in Fig. 4.12. As the average energy increases, however, the mean scattering signals begin to separate in the way one might expect, with the highest to lowest concentrations generating the highest to lowest signals, with the exception of the 1% concentration having the median scattering signal.

If the grouping pairs for average transmission, identified above and applied also to the average scattering signals, are considered as well as the trends of those signals, they can be linked to where in the FoV the concentrations were imaged, shown in Fig. 4.13 (a). The same pairings of transmission and scattering signals for the different concentrations (Fig. 4.12) can be seen in the positions of the cuvettes, with concentrations 1 and 0.1 in the same position, 0.5 and 0.05 sharing another, and 0.01 in the centre of the field of view. A pixel-by-pixel retrieval, which should account for different pixel responses by using their unique ICs, was used, yet the retrieved scattering signals do not appear to correlate with microsphere concentration. Considering data obtained by Millard *et al.* [80], which show

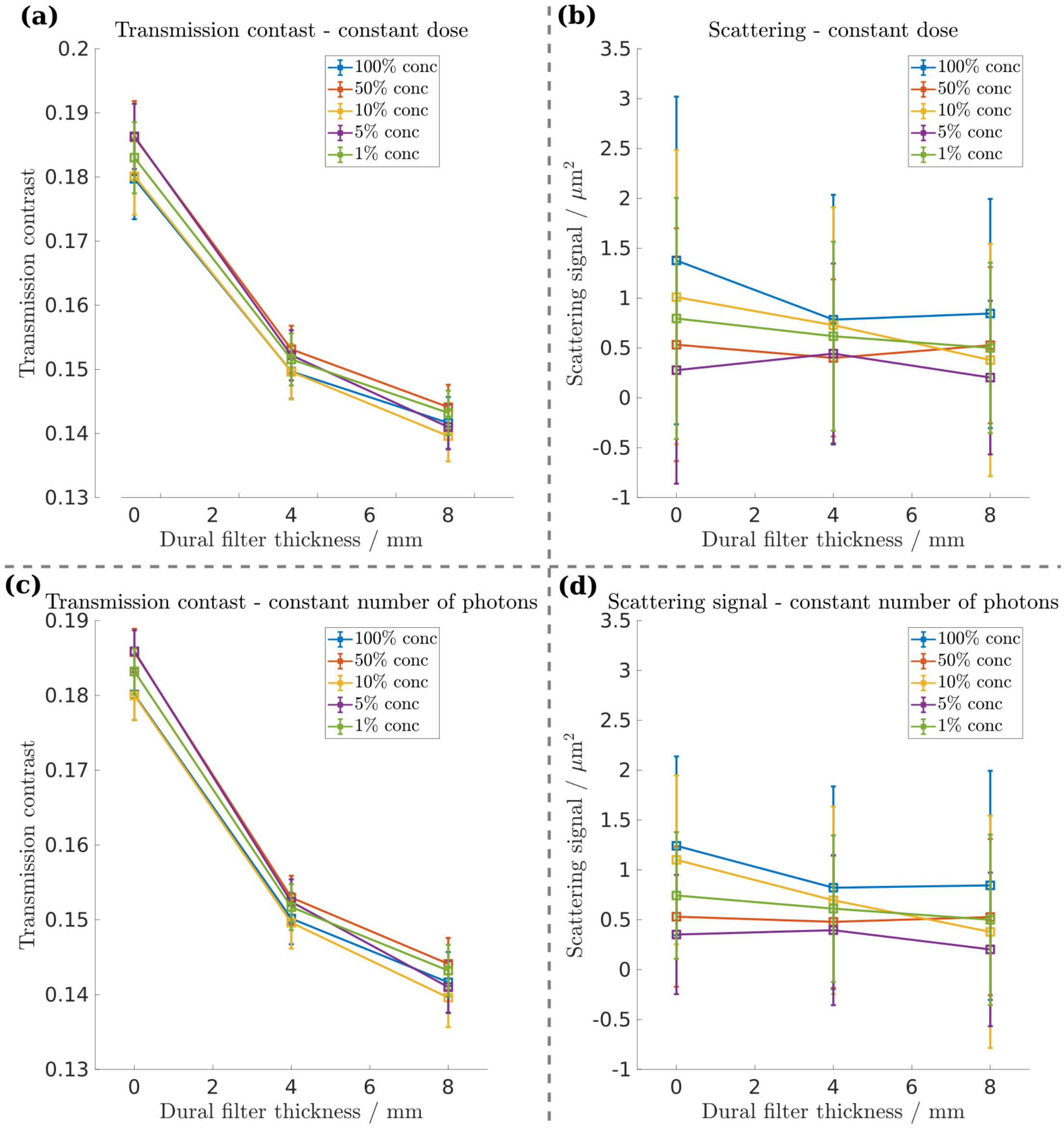

Figure 4.12: Transmission contrast (a), (c) and scattering signals (b), (d) for various concentrations of microspheres suspended in ultrasound gel, imaged through increasing thicknesses of dural filter. (a) and (b) are retrieved contrasts in the case of dose being kept constant for each measurement; (c) and (d) for constant total counts.

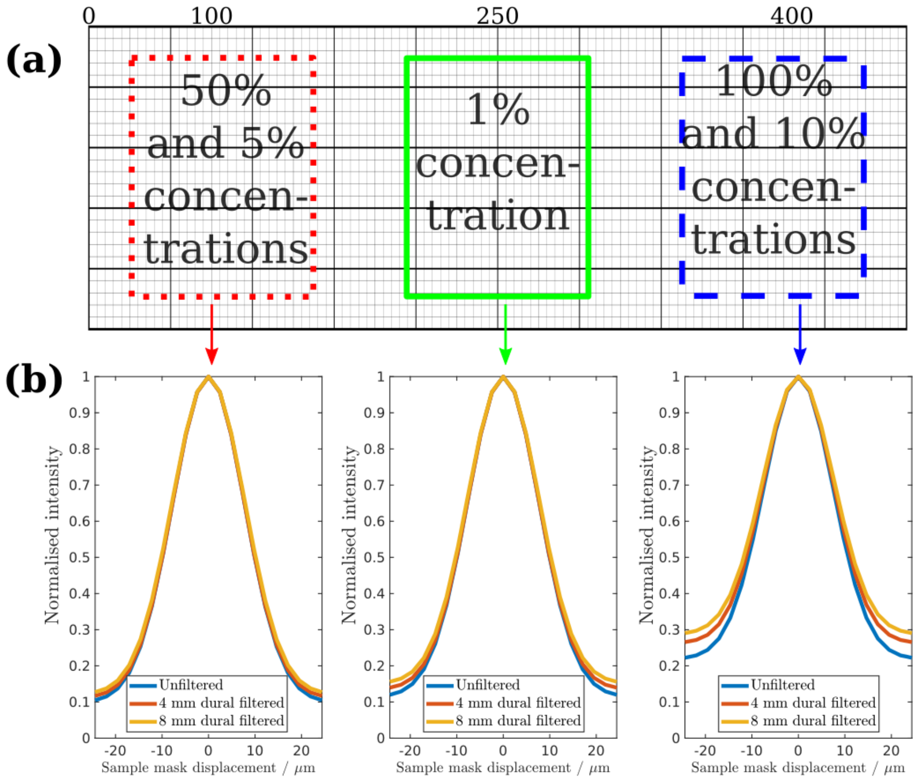

Figure 4.13: (a) Positions of the different microsphere concentrations in the Pixirad field of view, with pixel numbers marked at the top of the grid; the porous sponge was imaged in approximately the same position as the 100% and 10% microsphere concentrations. (b) Illumination curves corresponding to the centres of each marked location in the FoV.

that this correlation exists in XPCi, and that the results of the previous chapter validate this for high x-ray energies, the large difference in retrieved scattering signals between 1 and 0.5, compared with that between 1 and 0.1, must be due to one or two effects:

- The effective energy of the system varies significantly between the two sections of the detector used in imaging the sphere concentrations, thus changing the *real* scattering signal by some amount, and / or
- The illumination curve functions used in the retrieval of dark field signals, seen in Fig. 4.13 (b), are different in a way that significantly affects the sensitivity of the retrieval algorithm, i.e. the *retrieved* scattering signal is changed.

A difference in effective energies, and a contributing factor to the difference in ICs, could be a result of the Heel effect. This, and a variety of physical mechanisms that may affect IC parameters, are investigated in the next chapter. That the scattering signals appear to correlate with the microsphere concentrations when imaged through 8 mm dural supports the hypothesis of there being different effective energies, as the change in mean energy across the FoV due to the Heel effect should decrease with increasing filter thickness due to the reduction in spectral bandwidth.

In principle, it should be possible to correct for the Heel effect by using a tungsten wedge placed in front of the source that compensates for the self filtration of the anode, but such a task is not undertaken as part of this thesis. That the Heel and other effects could cause such large variations in a laboratory-based system's parameters, and hence have such a significant impact on dark field imaging, was never observed or hypothesised before and is discussed here for the first time. Unfortunately, the observation was only made during the data analysis phase, when the experimental setup was no longer available for more experimentation.

4.4 Modelling results and discussion

Modelling of the Hamamatsu experiment considered sapphire wire profiles, which were simulated using 10 dithering steps and dividing by flats simulated at the same points on the illumination curves as were used experimentally - the IC half maximum positions. The results, which show a moderately good match between simulated and experimental wire profiles, but a poor match between ICs, are shown in Fig. 4.14.

In the Pixirad case, PEEK and sapphire wire profiles were simulated using 12 dithering steps and again dividing the output by appropriate flat fields, with

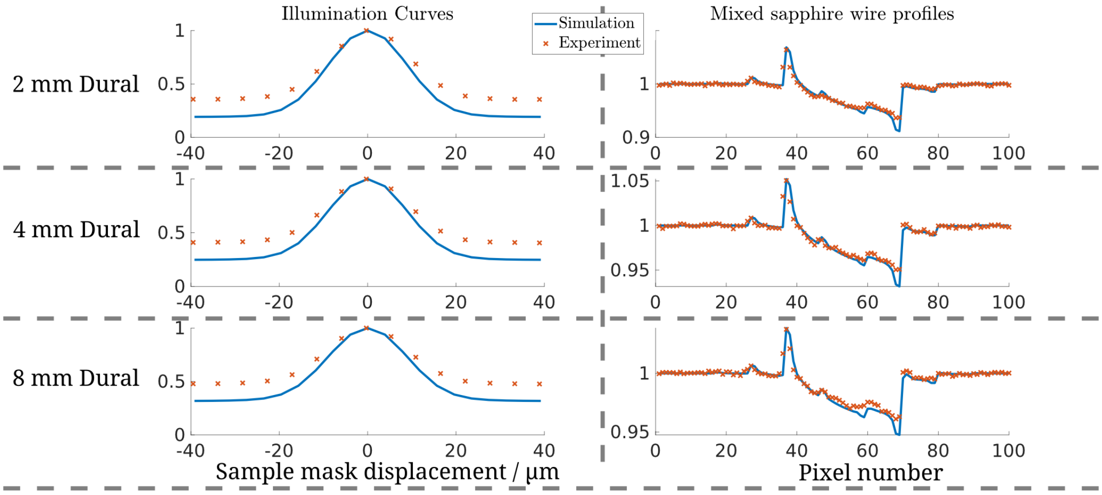

Figure 4.14: (Hamamatsu) Simulated and experimental ICs and sapphire wire profiles as measured through different thicknesses of dural filter; the simulated spectra are generated via the TASMICS software and filtered by **3** μm of tungsten; the mask thicknesses used in simulations were equal to the nominal thickness of 150 μm.

the results being shown in Fig. 4.15. These show that the simulated ICs strongly deviate from the measured equivalents, and in the case of the sapphire wire, neither the absorption or refraction signals are being simulated correctly; the PEEK wire, however, appears to be simulated reasonably well. As is evident from figures 4.14 and 4.15, simply using the nominal values from experimental conditions is insufficient to reproduce the results correctly. Therefore, possible corrections and adjustments to the initial model parameters are explored in the following sections.

4.4.1 Adjusting Hamamatsu model inputs to match experimental results

There are two system parameters that have significant effects on simulation outputs and about which it is difficult to be certain: the thickness of the absorbing septa used in the masks, and the spectrum. When seeking to match simulated and experimentally measured ICs, the former parameter, with only one degree of freedom as opposed to the N energy bins making up the spectrum, is expected to have a stronger effect on the IC simulation outputs. Changing the spectra, however, is expected to have a more significant effect on the wire profiles. As

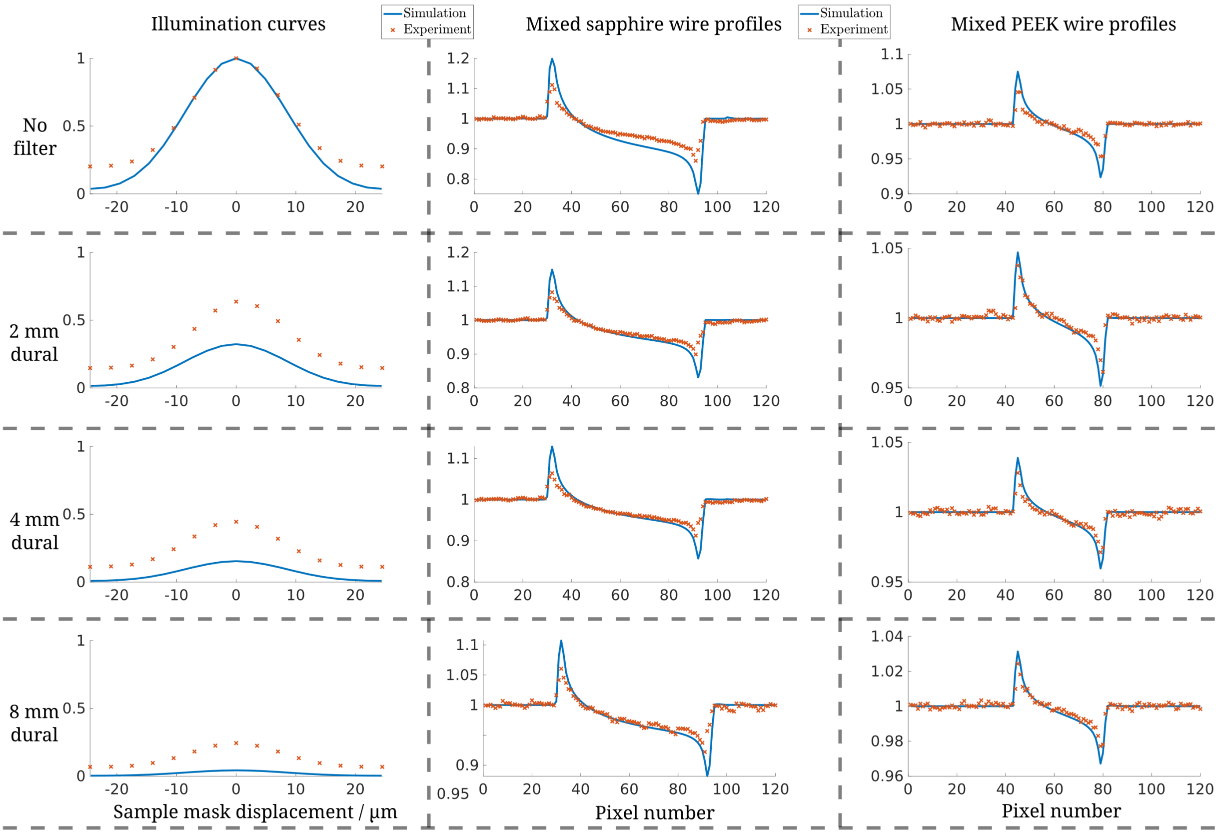

Figure 4.15: (Pixirad) Simulated and experimental ICs, normalised by the peak intensity of the unfiltered IC; sapphire and PEEK wire profiles as measured through different dural filter thicknesses. The simulated spectra are generated via the TASMICS software and filtered by **3** μm of tungsten; the mask thicknesses were equal to the nominal thickness of 300 μm.

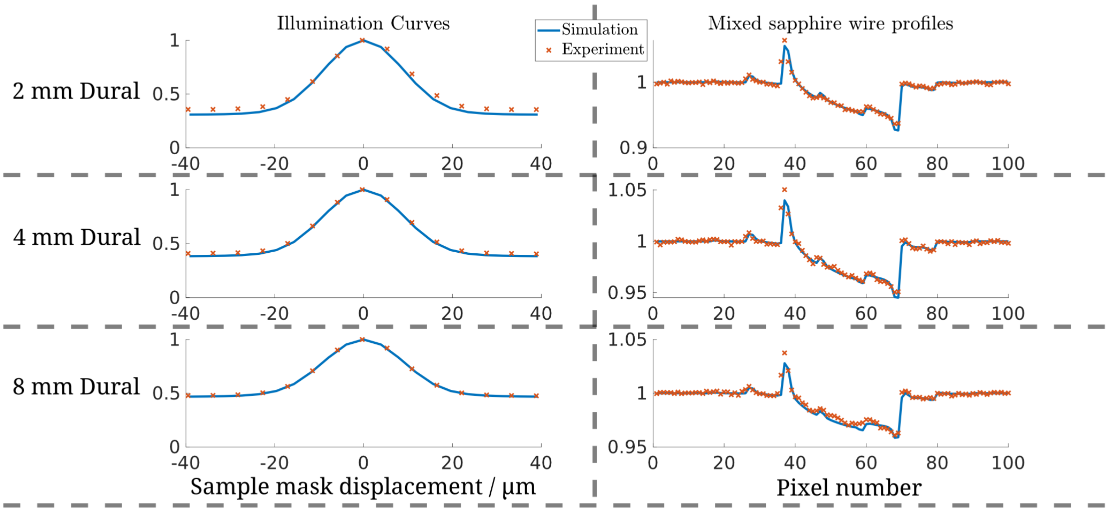

Figure 4.16: (Hamamatsu) Simulated and experimental ICs and sapphire wire as measured through different thicknesses of dural filter; the simulated spectra are generated via the TASMICS software and filtered by **3** μm of tungsten; the mask thicknesses were reduced from the nominal thickness to 120 μm. ICs have been normalised by the maximum intensity of the unfiltered beam.

TASMICS has been repeatedly proven to be reliable [81, 82], and the assumption of some additional self-filtration of our source reasonable, we leave this variable unchanged for now and change only the thickness of the absorbing gold septa in the masks. Indeed, a simple trial and error approach of reducing the amount of gold in the absorbing septa and observing the effect of this on the ICs finds that a septa thickness of 130 μm (for the Hamamatsu experiment, where the nominal septa thickness was 150 μm), in both masks, leads to a better match for the ICs and some small improvement in the wire profiles, as shown in Fig. 4.16. As the simulated and experimental outputs match for each of the filter thicknesses, it is clear that the parameters used in the simulation must be sufficiently close to those used in the experiment. A lower projected thickness of gold could be due to the electroplating not continuing to the nominal septa thickness, or possibly because the electroplated material has a lower density than solid gold. An effective 20% loss of gold for masks of this thickness (which the supplying company agrees can be considered acceptable) results in the IC offset being 10-15% higher than expected.

4.4.2 Hamamatsu modelling of the SNR of wires in water

Concerning the SNR of wires varying with filter thickness, the wires imaged experimentally through water with the Hamamatsu detector used flat fields taken in air, hence the SNR trends in Fig. 4.6 for this setting are inconsistent compared to the other measurements. Our model, in combination with data from Fig. 4.10, can be used to make predictions on how the SNR would vary had the experiment been conducted using flat fields in water of the same thickness. Using the simulation parameters determined in the previous section, nylon, PMMA and teflon wires of (arbitrary) radius 675 μm were simulated in a water medium with an unfiltered spectrum, and spectra filtered by 2 mm, 4 mm and 8 mm dural, with normalisations by flat profiles acquired through the same amount of water and filter thickness. Noise, whose standard deviation was set to the same values seen in Fig. 4.10, was added to these profiles before processing. The profiles were processed in the same way as the experimental data (Section 4.2.3) to retrieve absorption and refraction SNR values, with the results being plotted in Fig. 4.17.

The actual SNR values are arbitrary in this case, as they depend on the beam intensity and integration time of an actual experiment, however the trend is discernible for wires in water being imaged with the Hamamatsu detector for a constant dose. While the results are dependent on the wire material, the general trend of refraction SNR is semi parabolic, with a peak when imaging through 2 mm dural. The absorption SNR shows greater variation with filter thickness, increasing significantly for PMMA and teflon, but decreasing for nylon. Comparing these results with the measured SNR of PMMA in Fig. 4.6, we can qualitatively say that the different spectrum of the flat field “shifts” the SNR curve’s peak to the higher filtration setting in refraction. This is reasonable, as we expect smoother noise in the sample images than in the flats due to the energy response of the detector, but this difference decreases as the beam is hardened by filters. If the filter becomes

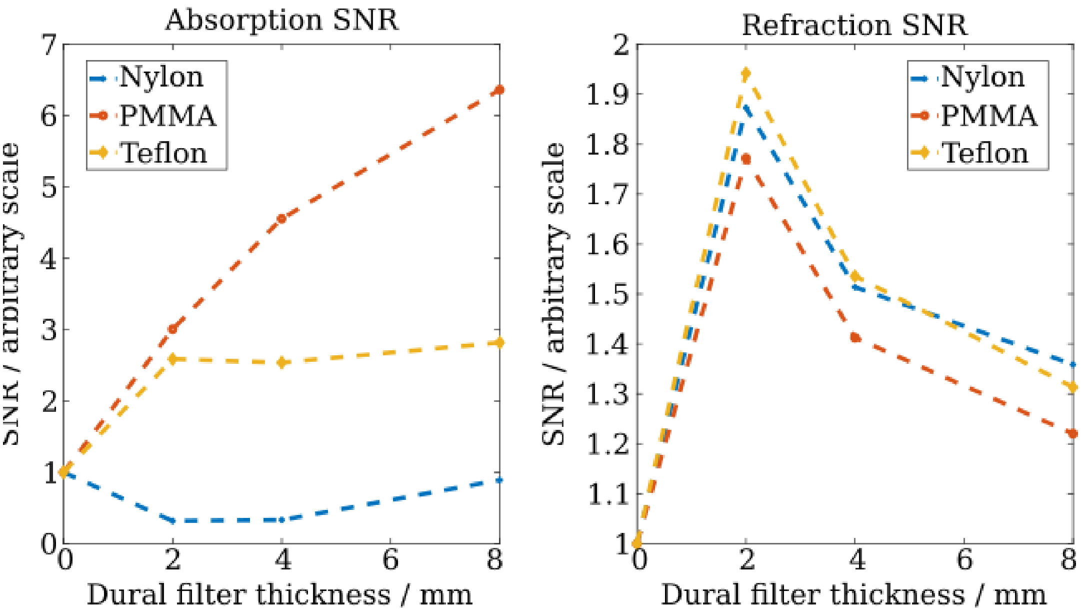

Figure 4.17: Simulated signal to noise ratio trends of nylon, PMMA and teflon wires (675 μm radius) immersed in water and imaged at constant dose with the Hamamatsu system through increasing thickness of dural filters. The simulated 60 kVp tungsten spectra were generated by the TASMICS software.

sufficiently thick, the difference in spectra between air and water media, outside of the sample region, will become small. From the simulation, refraction signals of the PMMA wire normalised by a flat field through air are almost identical to those normalised by a flat through water. The absorption contrast, again according to the simulation output, is improved slightly by 2.5% when using a flat field through air, however as seen in Fig. 4.6, the SNR for this wire is already very low and so the small boost in contrast is of little significance.

4.4.3 Pixirad modelling adjustments

Fig. 4.15 used the nominal mask thickness of 300 μm and the same initial spectrum as in the Hamamatsu case. The simulated IC offset, the absorption signal at the centre of wires being lower than experimentally measured (by 2.7% in the unfiltered case), and the magnitude of phase peaks being greater than in the experiment, all indicate that the spectrum used in the model is too soft, i.e. the average energy is too low. The deviation between modelled and experimental ICs,

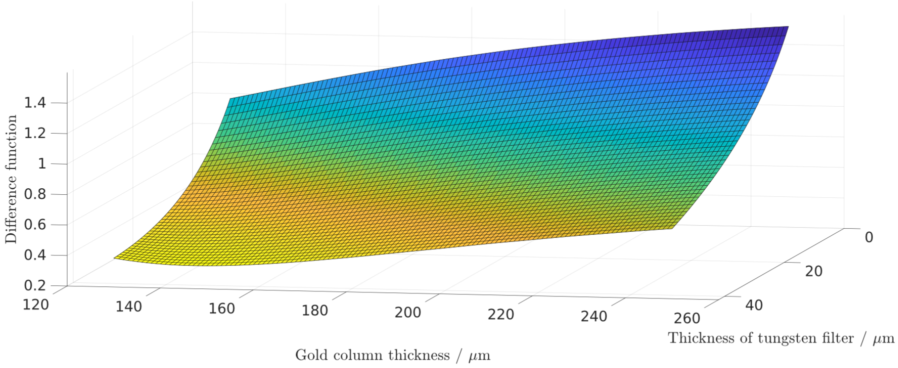

Figure 4.18: Difference function between simulated and experimentally measured IC and wire profiles for varying mask septa and tungsten filtration thicknesses.

however, is not limited to the offset: it persists for all points on the IC such that the simulated peak intensity, or the expected attenuation of the raw beam due to filters, is systematically lower than measured in experiment.

Fig. 4.16 implies that the refractive index parameters used to simulate the sapphire wire are correct, thus, as the masks and detectors are the most significant changes in system parameters, the inaccuracies of modelling is likely to be due to these elements. The Hamamatsu and Pixirad experiments were also conducted a little over a year apart; it is possible that, as the source was in almost continuous operation during this time, the tungsten anode could have ejected particles over time that coated the source window, forming an additional filtration layer. With this in mind, I attempted to find a combination of parameters for gold thickness and tungsten filter thickness that led to a match between simulation and experiment.

Changing the amount of self filtration has a predictable effect on each of the N energy bins of the spectra, so a systematic approach was taken in order to find a solution that worked for all the changing variables. Eq. 4.6 is the minimisation used:

$$\chi \xrightarrow{\text{Minimise}} \sum f^2(t_{\text{Au}}, t_{\text{W}}) - Y^2_{\text{IC, wire}}, \tag{4.6}$$

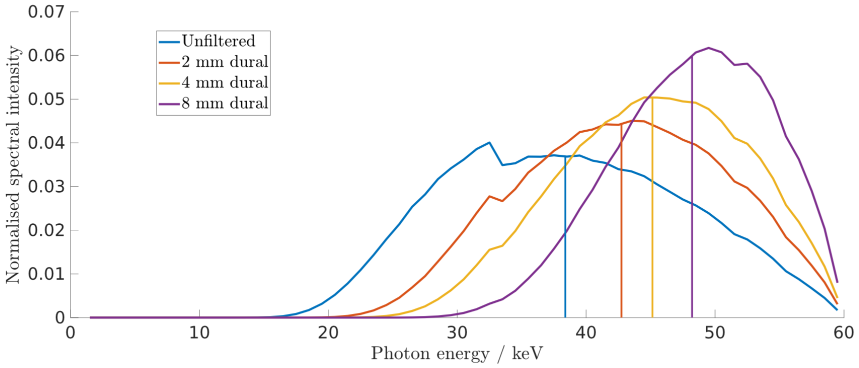

Figure 4.19: Effective specta of a beam filtered by 42 μm of tungsten used to best-match experimental Pixirad measurements through increasing thicknesses of dural filters. Vertical lines indicate mean energies.

where $f(t_{\mathrm{Au}}, t_{\mathrm{W}})$ produces a matrix of simulated IC data and wire profiles as a function of gold column and tungsten filter thickness. The output for χ is displayed in Fig. 4.18, with a global minimum being found for $t_{\mathrm{Au}} = 147$ μm and $t_{\mathrm{W}} = 42$ μm. Fig. 4.19 shows the spectra and mean energies for this level of filtration, while Fig. 4.20 shows the simulation outputs for this combination of parameters. Even for this extreme filtration and less than 50% gold in the masks - both of which are excessive - the ICs and wire profiles fail to consistently match their experimental equivalents through the various filters. The observation that dark field signals originating from the microspheres (Fig. 4.12) are significantly influenced by *where* they are positioned in the detector FoV implies that there are systematic effects present that have not been accounted for, and a more sophisticated model may be required to determine what these effects are - this will be the subject of the next chapter.

4.5 Conclusions

For constant dose, the SNR of wires measured in air decreases with increasing energy for both absorption and refraction. For wires in water, however, the SNR trend is curved, with a positive or negative turning point depending on which of

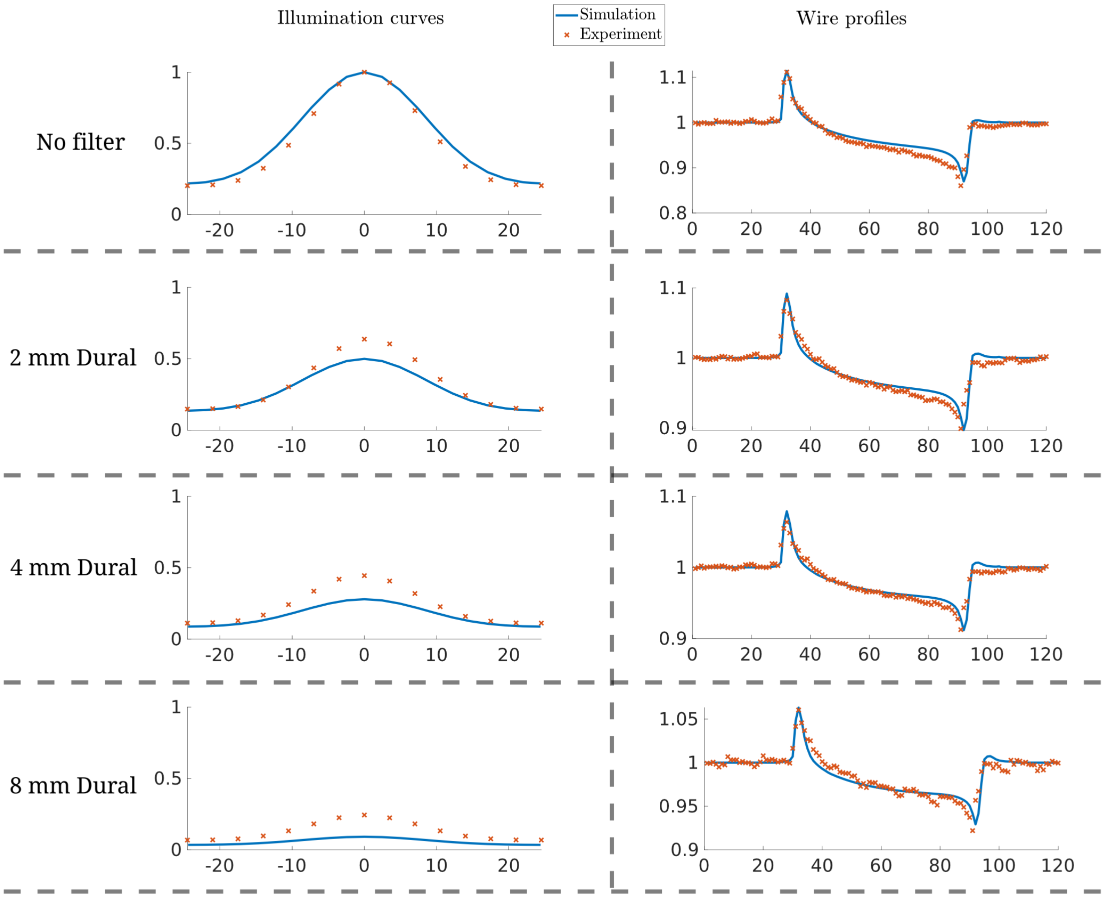

Figure 4.20: Simulated and experimental ICs, normalised by the peak intensity of the unfiltered IC, and sapphire wire profiles as measured by the Pixirad detector through different thicknesses of dural filter. Simulated spectra were generated by the TASMICS software and filtered by **42** μm of tungsten; the mask thicknesses were reduced from the nominal thickness of 300 μm to 147 μm in order to provide a better, though still imperfect, match between simulated and measured ICs.

the two available detectors was used. This change in SNR behaviour due to the different host media can be attributed to two significant physical effects:

- The attenuation of photons through water being different to that of their attenuation in air. In both cases, more photons accumulate at the detector plane at higher filtration settings if the dose is kept constant, but this effect is greater in the case of water, meaning the noise is more reduced with increasing filter thickness in this case.
- The way in which the difference of refractive indexes varies between the “wires in air”, and “wires in water” cases, with contrast only decreasing in the former case and possibly increasing with mean beam energy in the latter case (neglecting the effect of absorption edges).

For the in-air measurements, lower energy experiments lead to a higher SNR, as the wires’ signals decrease at a faster rate than the noise with increasing energy. Since at constant dose, noise decreases with increasing filter thickness, the data suggest that it may be possible to choose an optimal filter thickness for a given imaging experiment, if enough is known about the material properties a priori.

Comparing the two systems employed in this chapter, it is clear in both cases that EI enhancement enables detection of wires that would otherwise go undetected in transmission-only systems. The Pixirad detector, with a near-flat energy response (and thus lower effective energy compared to the Hamamatsu detector, which weights high-energy photons more than low energy ones), measures greater refraction and transmission signals than the Hamamatsu. As the crosstalk between pixels in the Hamamatsu case is relatively large, the Pixirad detector also provides greater resolution when sample dithering is not employed. The thicker masks used in the Pixirad experiments also result in a lower IC offset, but modelling suggests that this offset should be even lower than measured experimentally.

Scattering signals for a porous sponge were acquired at different energies for a constant dose and are seen to decrease with increasing mean energy when imaged in air. In water, however, the sponge becomes invisible for all retrieved contrasts, showing that not all micro-structured objects will produce dark-field signals when immersed in a host medium with similar δ. Dark field signals due to different concentrations of microspheres immersed in ultrasound gel are seen to decrease with increasing energy in both the constant number of photons and constant dose cases, with smaller signal uncertainties at the highest energies for constant dose, but relatively constant uncertainties for constant number of photons. The ability to distinguish between different concentrations, however, is low in general, and appears to be affected more by their position in the FoV of the detector than by their concentration, at least for the two orders of magnitude in concentration that were used in the experiment. The precision could possibly be improved at the cost of an overall increased dose, but the change in dark field signal with position in the FoV is suspected to be a result of the Heel effect and variations in the IC parameters, whose impact is diminished by using large amount of filtration. Correcting for these effects should improve the ability to distinguish different concentrations, though this is yet to be tested.

When modelling the two experiments, the Hamamatsu system parameters were straightforward to determine: 3 μm ± 1μm of tungsten filtering the spectra produced by TASMICS in order to account for the different take-off angles between our source and the one modelled by TASMICS and 20% less gold than the nominal amount of 150 μm in the masks' absorbing septa. Using these settings, a wave-optics simulation was capable of re-creating the same ICs and wire profiles as measured experimentally. Having benchmarked the simulation in this way, it was possible to virtually recreate the SNR measuring experiments of wires in water for the Hamamatsu detector in a way that was consistent with the other measurements. The results emphasise that being able to tailor the average beam energy by filtering can improve SNR if dose is a constraint. Re-creating experimentally measured ICs and wire profiles with the model as it currently stands was not possible in the Pixirad experiment case, which used masks from a different manufacturer, with different specifications, and which was conducted a year after the Hamamatsu experiments (thus potentially having a slightly different amount of tungsten self filtration due to source window coating). The next chapter is aimed at refining the models to enable this recreation.

5

Model refinements required for high energy XPCi implementations

5.1 Chapter introduction and motivation

The previous chapter showed that, when using masks designed for high energies, the position of a sample in the detector's FoV played a significant role in the measured signals. This chapter describes how models which reproduce these effects were developed, while also incorporating additional effects that become relevant at high x-ray energies.

Various experimental measurements on the Pixirad masks, and the EI system of which they are a part, are presented as an ensemble. The addition of physical processes to the Monte Carlo and wave optics models are presented in order of significance to the simulation output over several sections. As the two models in use have unique advantages over one another, there are some cases where only one is refined, and this is made clear in the text. The last section describes how the fully upgraded model is utilised in combination with another simulation tool for wavefront propagation through ensembles of spheres to recreate the dark field experiments from the previous chapter. While the Pixirad masks described previously are the main focus of this chapter, it is expected that the knowledge gained will be useful when designing and characterising high energy EI systems in the future, and in understanding any inherent limitations of such setups.

5.2 Experimental measurements of the Edge Illumination masks

A source of uncertainty in modelling the EI system is the true thickness and density of the absorbing septa used in the masks. Normally this is not an issue, as the gold thickness parameter may be adjusted (as well as the source width, spectrum, and mask aperture widths) until a match between simulated and experimentally measured illumination curves is obtained. The results from the previous chapter, however, showed that this approach can lead to unreasonable results, where the gold thickness is less than half the nominal value (300 μm) and the spectrum is excessively hardened (42 microns of tungsten filtration) by anode self filtration from the outset. The following subsection describes the IC parameters measured across the Pixirad FoV, highlighting areas where measured values deviate significantly from expectation, then an experiment undertaken in an attempt to remove uncertainties regarding the masks used.

5.2.1 Pixirad IC parameters across the detector FoV

With the Pixirad EI system set up as described in Chapter 4, ICs were acquired in the normal manner by scanning the sample mask, M1, over one period and measuring the intensity at the detector. Fig. 5.1 (a) shows ICs across the FoV for the unfiltered 60 kVp tungsten spectrum and (b) - (d) show the fitted parameters of amplitude, IC centre position and width according to Eq. 4.1 for the unfiltered,

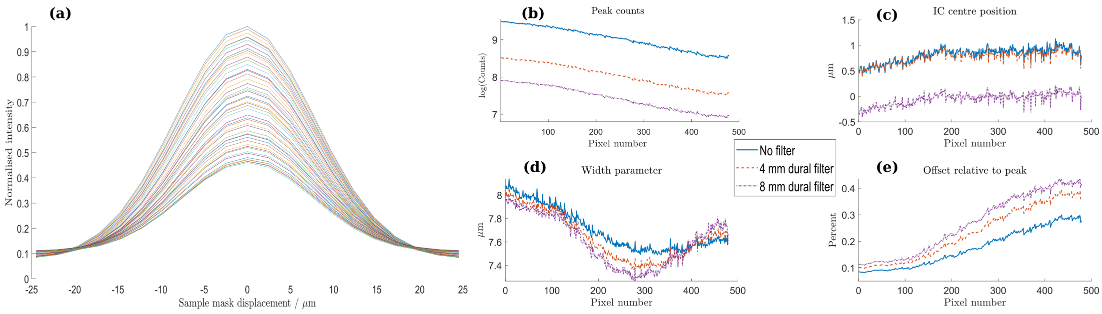

Figure 5.1: (a) Illumination curves across the Pixirad detector FoV for an unfiltered 60 kVp tungsten spectrum; each curve is an average of ten pixel columns. (b), (c) and (d) are fitted parameters for amplitude, centre position and width across the FoV for the unfiltered, 4 mm and 8mm dural filtered spectra; (e) is the ratio of IC minimum and maximum intensities.

4 mm and 8 mm dural filtered cases. Panel (e) shows the ratio of IC minimum and maximum intensities across the FoV for the same filtration settings. The following features of the EI system can be deduced from this figure:

- (a), (b) and (c) - The IC peak intensity decreases by more than 50% when moving from one side of the FoV to the other - a length slightly greater than 3 cm;
  - The stable position of the IC peaks indicate that this loss of intensity is not due to misalignment of the masks (which can lead to Moiré fringes).
  - The high level of mask alignment indicates that the masks are uniform in pitch across the FoV.
- (d) - The width parameter of the IC decreases and increases across the FoV;
  - The projected source size is expected to vary across the FoV, but should only be increasing from some minimum value.
- (e) - The offset-to-peak intensity ratio increases significantly across the FoV and is, on average, much greater than simulations predict for the nominal mask thickness and spectra (which would be 1%, instead of the measured 10% for pixels along the detector's left edge (DLE) for the unfiltered beam).

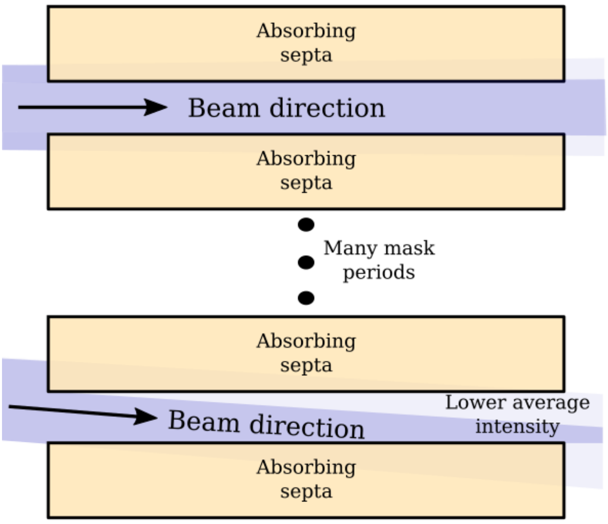

Figure 5.2: Illustration of angular filtration due to tall mask septa affecting beamlet intensity and IC widths (not to scale).

To some extent, the loss of intensity and the decreasing IC width can be explained by the angular filtration of the masks, the effect of which is illustrated in Fig. 5.2.

If a fully 3D model is used for the masks instead of the projection approximation, it should be possible to replicate the loss of intensity and decreasing IC width from the left to right edges of the detector. Making the masks into 3D components, however, requires making assumptions on how thick the absorbing septa are and, potentially, the density profile of those septa, which may or may not be significant. In practice, when using the nominal thickness and density of solid gold, a model that utilises 3D mask components predicts some loss of intensity across the FoV when the masks are aligned, but not as much as is measured experimentally. Moreover, if the full IC is modelled using these masks, the offset intensity they predict is the same as that predicted by models using 1D masks, which is significantly lower than what is measured. In the former case, where intensity is decreasing, the model thus implies that the thickness of the mask septa must be *greater* than the nominal 300 μm. In the latter case, to increase the offset to match what is measured, the septa thicknesses are required to be *less* than the nominal amount. Finally, it is also impossible, from these measurements alone, to decouple the attenuation due to M1 or M2 individually, which increases the complexity of the problem. ICs, however, are not the only measurements available.

5.2.2 X-ray measurements of the Pixirad masks

Two different experiments were performed using the available tools in attempts to discern the amount of gold in both mask septa. The difficulty shared by any approach using x-rays, however, is that decoupling the density of the gold septa from their thickness simultaneously requires both high energy and high resolution, which can be difficult to access. The density of solid gold is 19.3 g/cm^3, equal to that of tungsten, however this is an *upper limit* for gold that has been electroplated, as there is no guarantee that the packing efficiency of gold atoms during the electroplating process will be the same as that of solid gold. After the masks have been fabricated, the individual structures are also difficult to image with x-rays due to the close proximity of neighboring gold columns. Any measurements utilising the Pixirad EI system are also affected by some amount of tungsten filtration due to the Heel effect, which is not known *a priori* and may have changed since the Hamamatsu experiments described in Chapter 4.

5.2.2.1 Edge illumination field of view

Fig. 5.3 shows an example image of the entire Pixirad FoV when the system was aligned (note that the left side of the detector is not aligned for EI as the module was slightly rotated with respect to the module on the right). As shown, there is an active area where the EI condition is realised and an inactive area, where only the detector mask, M2, obscures the detector. With M1 decoupled from M2, the loss of intensity across the FoV should be primarily due to the angular filtration of M2 alone (see the red line in part (b) of the figure). Thus, it may be possible

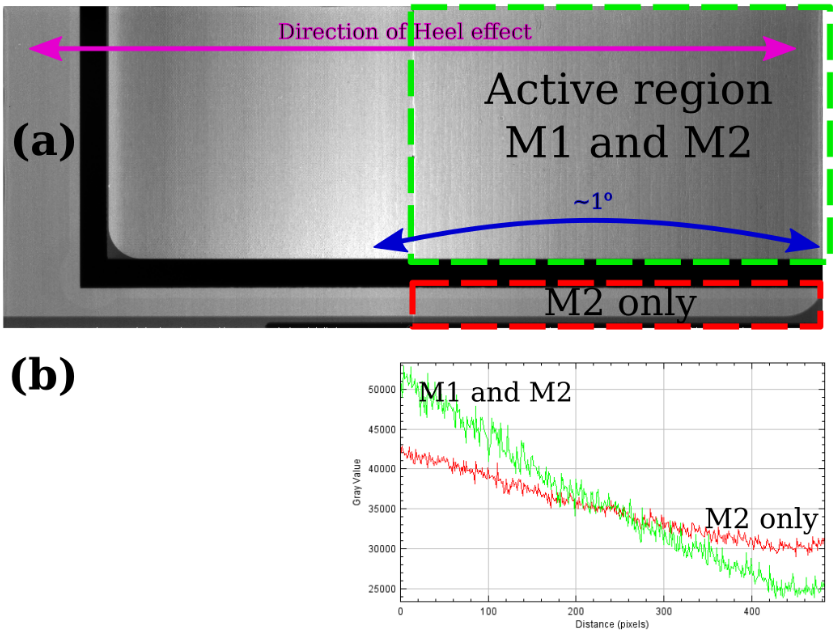

Figure 5.3: (a) Example FoV image from the Pixirad detector. For this system geometry, the angle subtended between the detector's left and right edges is approximately 1°; the Heel effect causes the spectrum to change across the FoV in the horizontal direction. (b) The loss of intensity due to both masks (54% ± 2%) and due to M2 only (29% ± 1%).

to create and use a forward model that aims to match this 29% ± 1% loss of intensity.

From the geometry of the setup, the detector's right-edge (DRE) makes an angle of $\approx 1°$ with the DLE (≈ 3 cm across, with the beam originating 2 m upstream); this can be used as an approximate value in determining the change in average filtration by the mask septa between pixels near the DLE and those near the DRE. All possible path lengths through the absorbing septa that arrive within given pixel boundaries must then be determined and weighted via the Beer-Lambert law.

Considering the polychromatic spectrum, there is some degree of uncertainty due to the Heel effect, but all other sources of filtration, such as the mask substrate (525 μm silicon), and 2 m of air, can be accounted for; the overall intensity loss across the inactive region of the detector, due to some thickness of M2's septa

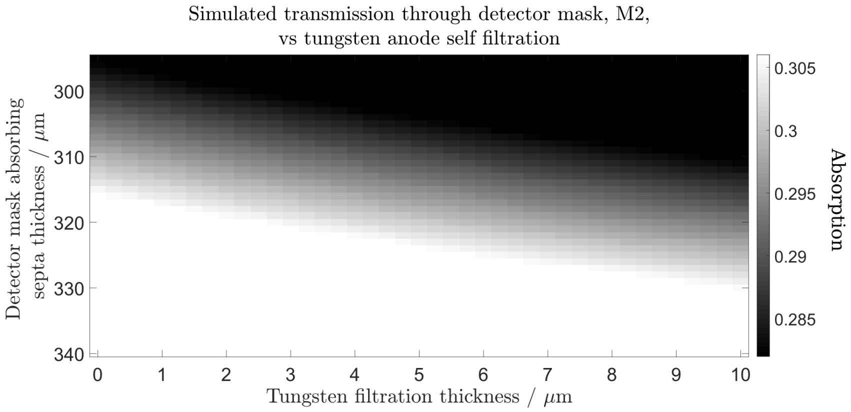

Figure 5.4: Forward model attenuation of the unfiltered 60 kVp tungsten x-ray beam due to angular filtration of the detector mask only. The experimentally measured attenuation was 29% ± 1%, i.e. the grey region of this figure.

(for now assuming the nominal density of solid gold) and for different amounts of tungsten filtration, may then be determined. Fig. 5.4 is the result of this, with the grey region defining the possible combinations of tungsten self filtration (x axis) and gold septa thickness (y axis) that produce the measured attenuation.

The range of possible septa thickness from this approach is 305 μm - 320 μm, corresponding to 0 - 10 μm of tungsten filtration. As the nominal septa thickness is 300 μm, this range of predicted thicknesses appears reasonable both in terms of accuracy and precision. If a reduced gold density is considered and the calculations performed again, the required amount of gold increases. By way of example: gold whose density is 75% that of solid gold requires septa thicknesses in the range of 325 μm - 340 μm, in combination with 0 - 8 μm tungsten filtration, in order to reduce the beam intensity by approximately 29%.

With plausible combinations of gold-tungsten thicknesses determined, it should be possible to use the same model to infer a range of septa thicknesses for the sample mask, M1, that satisfy the loss of attenuation due to both masks, as measured in Fig. 5.3. The geometry of the setup is again considered and a range of different septa thicknesses for M1 are assumed. In combination with pairs of M2 septa thickness and tungsten filtration values that resulted in the measured loss of intensity due to M2 alone, the decrease in intensity is determined for these thicknesses; with thicknesses of M1 that cause an intensity loss of 54% ± 2% being noted. For the lowest value of M2's septa, 305 μm (no tungsten filtration), this approach implies that the septa of M1 has a thickness of approximately 275 μm. For the largest M2 septa value of 320 μm (10 μm tungsten filtration), the corresponding M1 thickness according to the model is approximately 270 μm. However, using any of the combinations of M1, M2 and tungsten thicknesses calculated here in an IC simulation does not produce ICs that match those measured experimentally. Hence, given that:

- The Heel effect varies the amount of tungsten filtration and the flux intensity across the FoV, and
- EI models predict IC offset intensity for this septa thickness being much lower than is measured,

questions regarding the gold density and variations in the tungsten filtration thickness remain.

5.2.2.2 Attenuation images of Pixirad masks with the Hamamatsu detector

Attenuation images of the masks were taken under different conditions. In house at UCL, a microfocal (≈ 7.5 μm) tungsten source, operated at 60 kVp, was used in combination with the well-characterised Hamamatsu detector. A high magnification (10.2) was used and planar images of the masks were acquired alongside dark and flat field images. The projected source size and image blurring due to pixel crosstalk were small relative to the magnified pitch of both masks and the results of these measurements are shown in Fig. 5.5. Advantages of this method are that the source spectra and energy response of the detector were well known, image

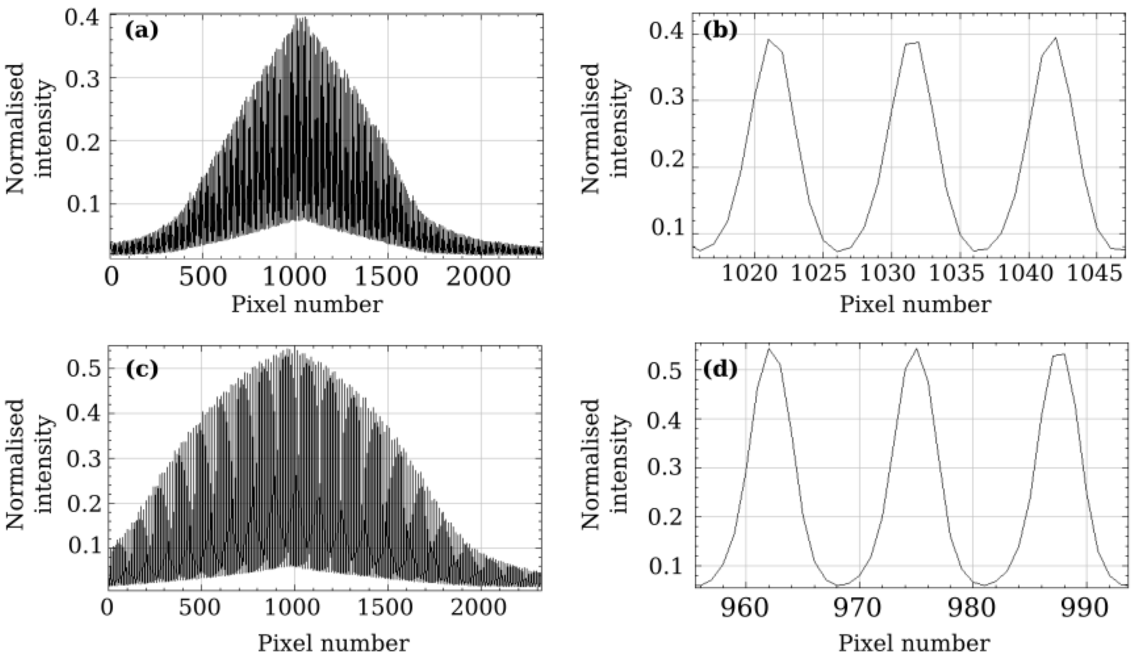

Figure 5.5: Normalised intensity profiles of attenuation images of (a) the sample mask, with (b) showing several periods close to the global maximum, and (c) and (d) showing the same for the detector mask. Magnification was 10.2, a 60 kVp tungsten spectrum was used in combination with the Hamamatsu detector.

blurring effects were small and the experiment was straightforward to implement.

Considering periods near the DLE, and assuming nominal mask parameters, the intensities measured through the apertures were approximately 10 - 15% lower than predicted by the simulations, while minimum intensities through the septa were approximately 5 - 6% greater than predicted. Similar to the problem of decreasing intensity across the Pixirad FoV, which contrasts with the IC minimum intensity being relatively high, this experiment failed to explain how the gold septa were simultaneously tall enough to cause significant angular filtration while not causing greater attenuation to the primary beam. However, the transmission through apertures being lower than expected led to the suggestion of including the effect of aperture-filling epoxy resin in the models, which did attenuate the beam more than expected (≈10% of an unfiltered 60 kVp beam). This experiment would possibly have benefited from an even greater magnification, as

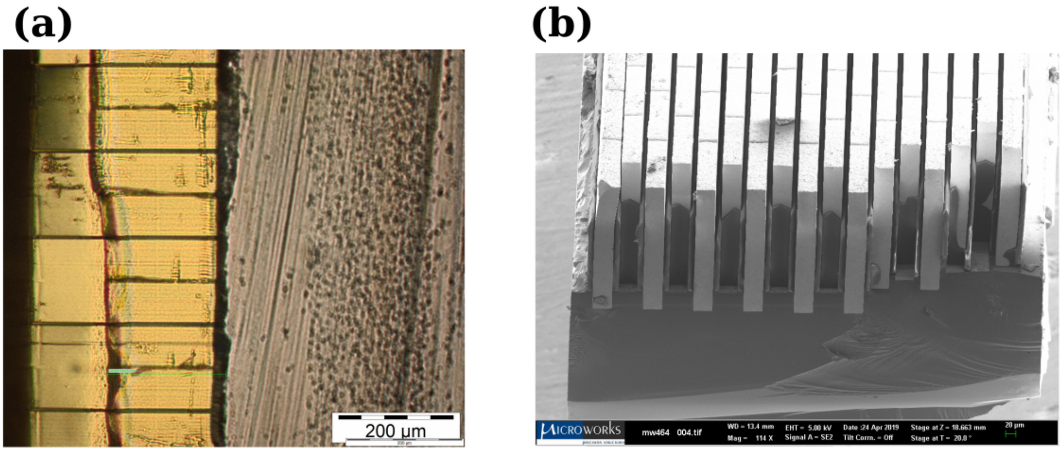

Figure 5.6: Optical (a) and electron (b) microscope example images of the Pixirad sample mask. The gold thickness of the sample mask was found to be 310 μm, with SU-8 in the apertures being approximately 203 μm thick with a triangular top.

simulation work later revealed that the density profiles of the absorbing septa may be non-uniform which, if this is the case, can affect how photons are attenuated by different parts of the septa.

5.2.3 Direct measurement of the Pixirad mask thicknesses and bulk density

Ultimately, as different measurements were unable to converge on a single set of parameters that described the masks, the septa thickness and density were measured directly via destructive methods by technicians at microWorks. The information gained here, in combination with the previous measurements, led to a working model of the masks (and hence the EI system) and may be useful both in the fabrication of EI masks and in the design of future high energy EI systems.

A diamond saw was used to slice 0.7 mm wide sections of both masks. Optical imaging was performed under a microscope to determine the septa thickness, and again with an electron microscope in order to determine the thickness of epoxy resin in the apertures; the sections were also weighed in order to ascertain the

	Sample mask	Detector mask
Thickness / μm	310	319
Gold density / g cm^{-3}	17.3	17.5
Density / Percentage of solid gold density	89.5	90.8

Table 5.1: Pixirad mask parameters determined by direct measurement; the substrate and epoxy resin masses were accounted for in the calculations.

bulk density of the electroplated gold.

Fig. 5.6 (a) and (b) shows example optical and electron microscope images of a section of the sample mask. Some gold lamellae were also removed and individually measured in height in order to further verify the optical measurements. The final results of septa length and density for both masks are listed in Table 5.1. The gold septa thickness being slightly greater than the nominal 300 μm in both cases explains the intensity loss across the Pixirad FoV, while the bulk density being $\approx$90% of that for solid gold gives insights as to why the Pixirad IC offset intensity is greater than models predict. The SU-8 filling the apertures appears to fill roughly 2/3 of the aperture volume, and has a triangular top; since the process of stripping SU-8 down from the original height of 350 μm was a passive process of oxygen free radicals interacting with the material, this shape is not necessarily going to be the same in other EI masks.

Understanding the reasons for less-than-nominal gold density is beyond the scope of this thesis, but by using data gleaned from the x-ray experiments and these direct measurements, a density profile of the absorbing septa that allows models to accurately recreate measurements of the masks, and the EI system of which they form a part, may be posited. Although this experiment requires at least partial destruction of the masks, the information gleaned is reliable and contains as much detail as is possible to acquire. It is expected that these results will have some applicability to other EI masks and gratings.

5.3 Model refinements

Many physical processes were built into the two models, with varying levels of significance in terms of their outputs. The following subsections are thus in order of priority for making a working model.

5.3.1 Angular filtration with three-dimensional mask models

Both the Monte Carlo model described in Chapter 3 and the wave optics model from Chapter 4 can be adjusted in order to reproduce the effect of angular filtration. The manner of implementation varies according to the models' computational workflow, illustrated in Fig. 5.7 (a) and (b); when discussing model upgrades, this figure can be used as a reference for each of the virtual objects being altered. In its first implementation developed by Millard *et al.*, EI masks used in the Monte Carlo model were simulated using the projection approximation, with photons entering an aperture (1) or absorbing septa (0) according to the function:

$$T(x) = \begin{cases} 1 \text{ if } \cos\left(\frac{2\pi x}{P}\right) \geq \cos\left(\frac{\pi w}{P}\right) \\ 0, \text{otherwise}, \end{cases} \tag{5.1}$$

where P is the mask pitch and w is the aperture width [74]. The refractive index of the septa is determined by a (formatted) look-up table and the incident photon's energy. A real photon is either absorbed or transmitted through the septa, and the Beer-Lambert law describes the statistical distribution of these events; simulations of such a process can be made to be computationally efficient by ascribing each photon an initial *weight* which is adjusted by the Beer-Lambert law as the photon traverses a material, then added to a given pixel bin at the detector (i.e. a photon that traverses N different media with attenuation coefficients μ_i and

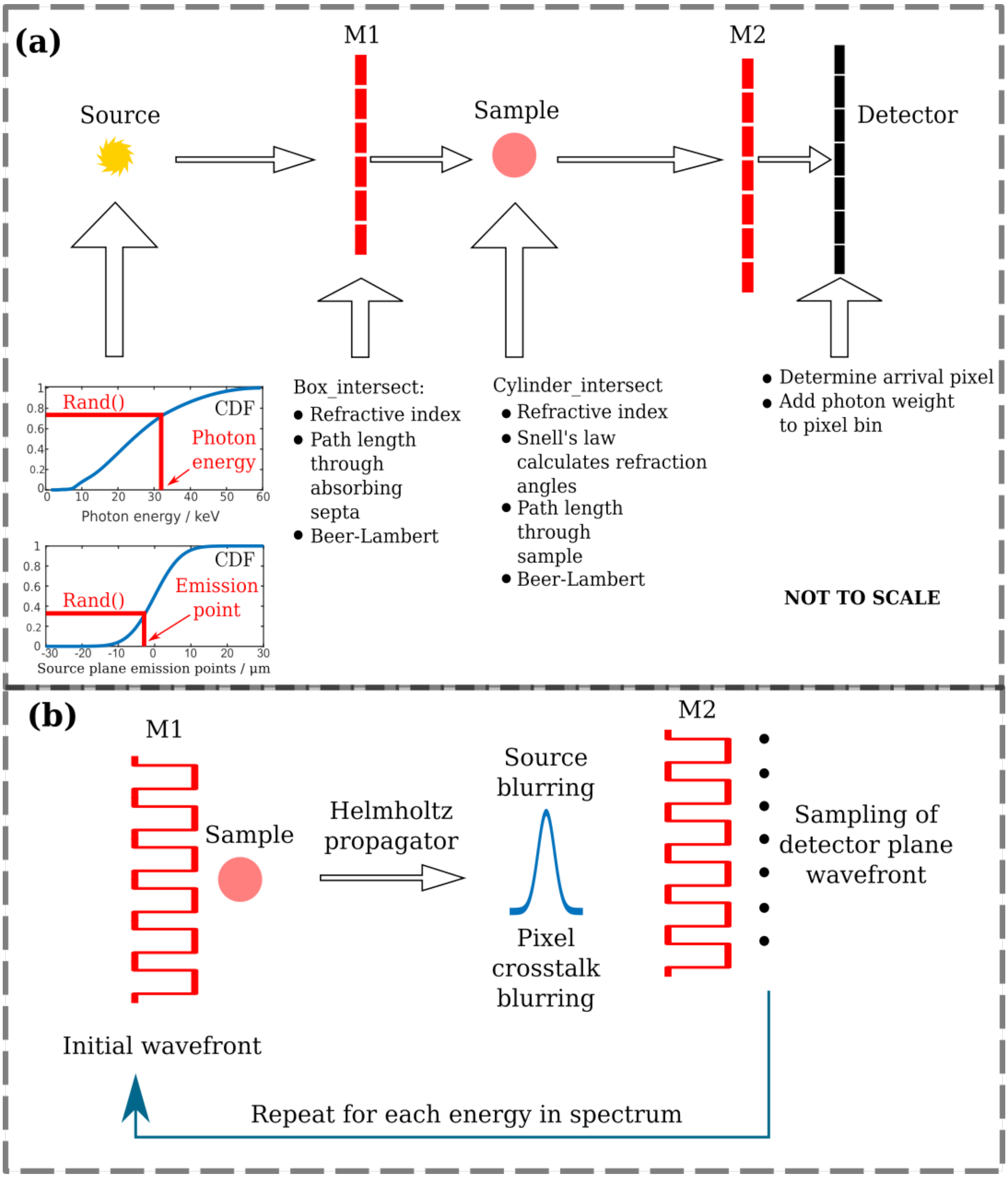

Figure 5.7: Computational workflows of the Monte Carlo model, McXtrace (a), and the wave optics model (b). McXtrace uses random numbers to select x, y, z emission points and energies of photons in the source plane, while the wave optics model iterates over discretised energy bins in the spectrum and blurs each intensity profile with the projected source function.

path lengths t_i has its weight adjusted from 1 to $\exp(-\sum_i^N \mu_i t_i$; all the weights of photons that arrive within a specified pixel area are summed to produce the intensity in that pixel). The efficiency gain lies in simulating only those events which will contribute to the final image statistics, rather than the full range of photons which are either transmitted or absorbed. For the mask component, a photon's weight is only adjusted when entering the septa, according to the single specified thickness in all cases, and is not at all attenuated if it enters an aperture.

The only change necessary in this Monte Carlo model is to make the absorbing septa into fully three dimensional cuboid structures by using the `box_intersect` function from the McXtrace library. Eq. 5.1 is still called to determine if a photon enters an aperture window or absorbing septa, however at this point, `box_intersect` is called to determine whether the photon will intersect an adjacent septum or window, or remain in the current section until the photon has traversed the full length of the component. The path lengths through absorbing septa and aperture are recorded in allocated variables and are then used to weight the photon, as described, as the photon leaves the component. This formulation improves on the model in a general way by determining the different path lengths through gold in all parts of the mask, which will have some deviation from the nominal thickness except in the case of a photon travelling parallel to the septa walls. As the model uses Cartesian geometry and simple equations to determine intersection of lines with planes, the additional computational cost is small.

The wave optics model uses a projected transmission function for the masks. A concise modelling method for angular filtration, then, is to replace this function with one that accounts for the curvature of the wavefront at different points. Fig. 5.8 (a) and (b) illustrates how a two-dimensional image, or matrix, of the mask is constructed and used in calculating the projected transmission functions. Each

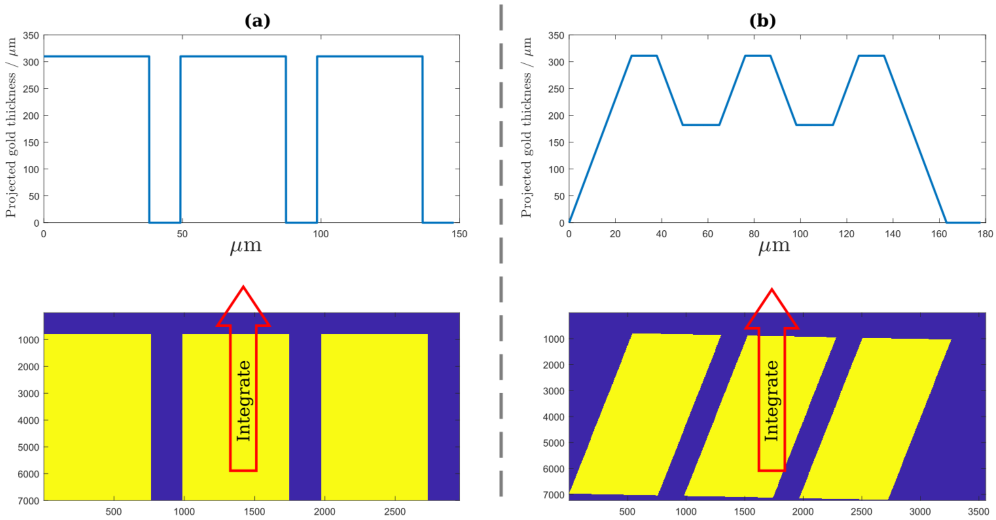

Figure 5.8: Illustration of how angular filtration may be handled in an XPCi wave optics model. (a) Shows the mask image and projected path length through gold for apertures parallel to the beam axis and (b) shows the same but for apertures far from the beam axis.

entry in the matrix takes a value of 1 or 0 to indicate the presence, or lack, of gold. For a given angle subtended by a point in the detector FoV, the matrix is rotated and integrated in the direction shown in order to determine the projected thickness of gold. The projected thickness is then used to determine a complex transmission function of the mask; the waveform is then propagated as normal to the detector mask, whose transmission function is determined using the same method. With this upgrade, the entire FoV may be simulated if necessary, though simulating larger fields of view means more image-rotation operations which, depending on the image size (determined by the sampling), can slow the simulation.

Both models return the same decreasing IC peak intensity, and Fig. 5.9 illustrates their increased resemblance to the experimental case they probe, by comparing the McXtrace output with real and simulated data from the model that did not use three dimensional mask structures. The new simulation output does not yet match the intensity gradient from real data, however - this is because the mask septa density, Heel effect and variations in source size have not yet been incorporated into the models.

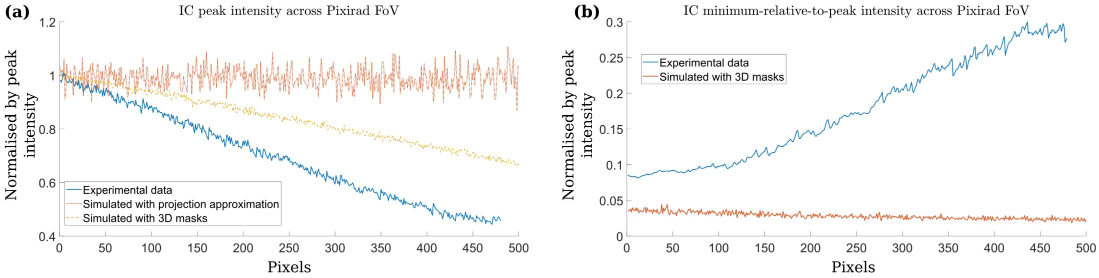

Figure 5.9: (a) IC peak intensities across the FoV of Pixirad for unfiltered 60 kVp experimental data and Monte Carlo simulated data that uses the projection approximation (red dotted line) and fully three-dimensional masks of thickness 300 μm (yellow dashed line). (b) IC minimum intensity, relative to the peak, for real and simulated (using 3D mask functions) data.

5.3.1.1 SU-8 inside apertures and variable mask septa density

SU-8 in the apertures leads to a small decrease (absorbing $\approx$9% of an unfiltered 60 kVp tungsten spectrum) in intensity transmitted through the apertures, and its beam hardening effect is negligible. The internal phase of a beamlet, however, may be affected, especially given the triangular top of SU-8 filling the apertures seen in Fig. 5.6 (b).The variable septa density also has a moderate impact on the EI system characteristics, such as the IC offset intensity. These are not “strong” effects, but are a straightforward addition to the models once the three dimensional nature of the masks has been included.

The chemical formula ($C_{723}H_{65}O_{182}F_{12}S_6Cl_2Sb_9$) and physical density (1.265 g/cm^3) of SU-8 were provided by the mask manufacturers microWorks GmbH, which enabled the x-ray refractive index to be generated by the `xraylib` software. The shape of the aperture filling is known from the electron microscope image in Fig. 5.6; while it could be modelled this way in the wave optics model, for convenience in McXtrace it is usually modelled as a cuboid that fills approximately two thirds of the aperture: this led to no visible difference in model outputs. Variations in the gold septa density are easier to implement in the wave optics model: as the projected thickness is determined by summing pixels which are normally set to 1, the values may instead be set to have reduced values depending on their position. A single reduced value can be applied universally to all septa pixels or, if the density profile were known, this could be applied as appropriate to the image pixels.

5.3.2 The Pixirad detector response

For an EI system, the potential impact of multi counting can be significant. Referring to Fig. 2.14, multi counting may occur when a photon of sufficiently high energy is incident near the edge of a pixel; the generated charge cloud spreads across both pixels and is sufficient to exceed the threshold in both cases. Consider two cases of the EI system:

- M1 is aligned with M2 (the IC peak) -
    - Any photons not absorbed by the septa that reach the pixel do so near its edge and are likely to be of high energy, thus having a high likelihood of being counted multiple times, however:
    - Flux due to the primary beam through M2's aperture accounts for the majority of photon events.
- M1 is out of phase with M2 (the IC minimum) -
    - High energy photons, which are more likely to be transmitted through some amount of gold in the septa of M1 or M2, form the majority of photons being detected; they arrive near pixel edges and corners and are thus likely to be counted multiple times.

The relative intensity measured for these two cases will be affected as the ratio of multi-to-single counts is shifted. In order to incorporate this effect in the models,"near pixel boundaries" must be defined. Charge-sharing for a similar detector, the Pixirad-1 photon counter, was characterised by Vincenzi *et al.* [83], based on

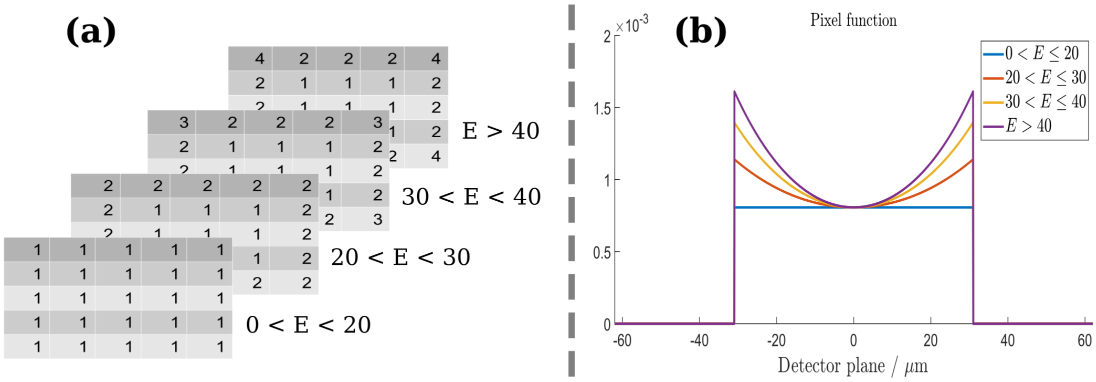

Figure 5.10: Scheme for multi-counting implementation in (a) McXtrace and (b) wave optics models; the Pixirad detector they represent had a low energy threshold of 10 keV, thus only photons of twice this energy or more can be counted multiple times. McXtrace implements sub-pixel energy resolution, with each energy band having a specified weighting scheme; the wave optics model changes the pixel function for each energy band through use of a cosh function such that pixel edges contribute $\sqrt{A}$ more to the final intensity than pixel centres, with A being 2, 3 and 4 for each of the energy ranges considered in this 1D model.

methods described by Iniewski *et al.* [84]. Thus, I make an approximation for the radius r of a diffuse electron cloud at a pixel anode to be given by the equation:

$$r = 2.3d\sqrt{2k_BT/qV}, \tag{5.2}$$

where d is the photoconductor thickness (650 μm), k_B is the Boltzmann constant, T is the temperature in Kelvin (253 K), q is the charge of an electron and V is the applied bias voltage (400 V). Using these values leads to a charge cloud with an approximate radius of 7.8 μm. Considering whether such a cloud may spread from its point of origin in one pixel, across boundaries and into another pixel, this value is used as a baseline.

Figures 5.10 (a) and (b) show how multi counting is approximated in the Monte Carlo and wave optics models, respectively. In McXtrace, pixels are sub-divided into 5×5 grids (of 12.4 μm sides) and are simulated as being semi-energy resolving. As the low energy threshold of the Pixirad detector was set to 10 keV in all experiments, only four energy bins of $10 < E < 20$ keV, $20 < E < 30$ keV,

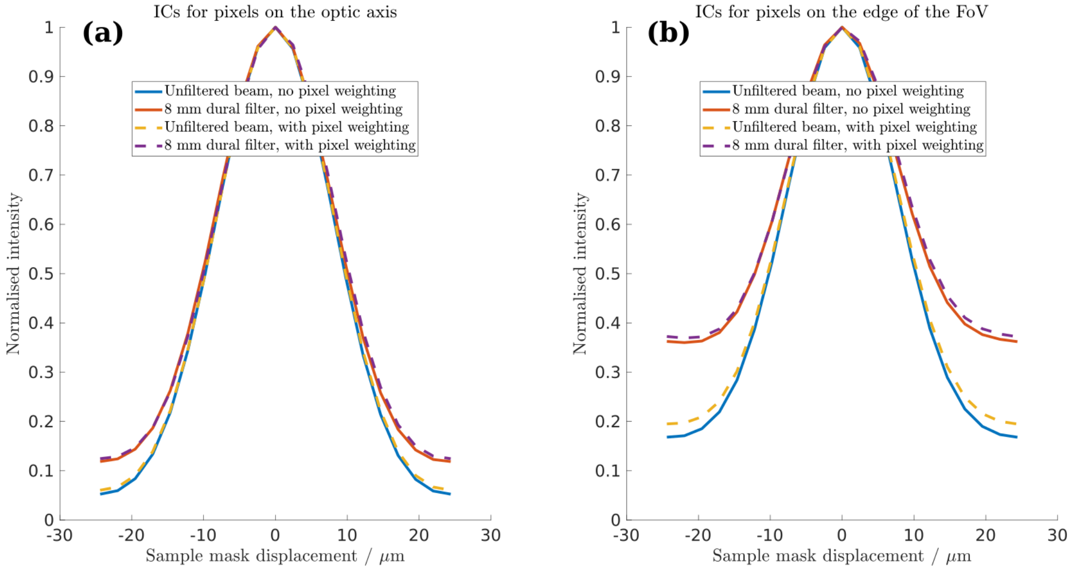

Figure 5.11: Effect of the Pixirad detector counting single photons multiple times on IC measurements in the case of an unfiltered and 8 mm dural filtered 60 kVp tungsten spectrum: on the detector's left edge (a), and on the detector's right edge (b).

$30 < E < 40$ keV and $E > 40$ keV are necessary. After the simulation is complete, the true pixel regions are defined, with the edge and corner sub-pixels being weighted according to their energy range, before the sub-pixels are finally binned. In the wave optics model, the pixel function - normally a top-hat - is adjusted in a similar, but continuous, manner according to the energy range in question. A cosh function is used to modify the pixel function, as it encapsulates the pixel's symmetry and the exponential damping of electron movement in the semiconductor material. As wave optics typically considers the one-dimensional case, the adjusted pixel function increases only to the square root of the maximum weight used in the McXtrace weighting scheme.

Fig. 5.11 (a) shows the effect of multi counting on a simulated IC for an unfiltered and 8 mm dural filtered 60 kVp tungsten spectrum for pixels located on the DLE and (b) shows the same for pixels located near the DRE, where the angle of beamlets results in more photons arriving near pixel boundaries. For ICs acquired near the DLE, multi-counting has very little effect on the offset intensity for both the unfiltered and highly filtered beam. Far from the axis, however, the increase in the offset intensity is visible, particularly for the unfiltered beam. The reason for this lies with the ratio of multi-to-singly counted photons: in the unfiltered case, where the spectral bandwidth is large, the ratio increases as M1 moves out of phase with M2 due to the relative increase in high energy photons being detected, as these are the ones that are more likely to be transmitted through the mask septa. In the highly filtered case, the bandwidth is smaller, meaning that the number of high energy photons that induce multiple counts is high for all points of the IC.

5.3.3 The Heel effect and variable source size

The apparent size of the source, its brilliance and the amount of self-filtration due to the Heel effect vary depending on the angle from which the source is viewed, as illustrated by Fig. 5.12 (a). Our source having a shallow take-off angle, which enables high power output from a small region, enhances this effect and is *evidenced* by the measured width parameter of ICs across the FoV shown in Fig. 5.1 (d). For a source of fixed size, models predict that the IC width should decrease uniformly across the FoV due to the effective aperture size decreasing; the measured curve, however, decreases and then increases again across the FoV.

To model the Heel effect perfectly would require full knowledge of the electron beam's penetration depth and exact geometry of the anode, which is not available. Some assumptions were thus made in order to determine the appropriate level of filtration of the system for different source-viewing angles. These are that:

- The transverse variation in tungsten filter thickness would be linear.
- Any variations of tungsten filter thickness in the vertical direction could be neglected.

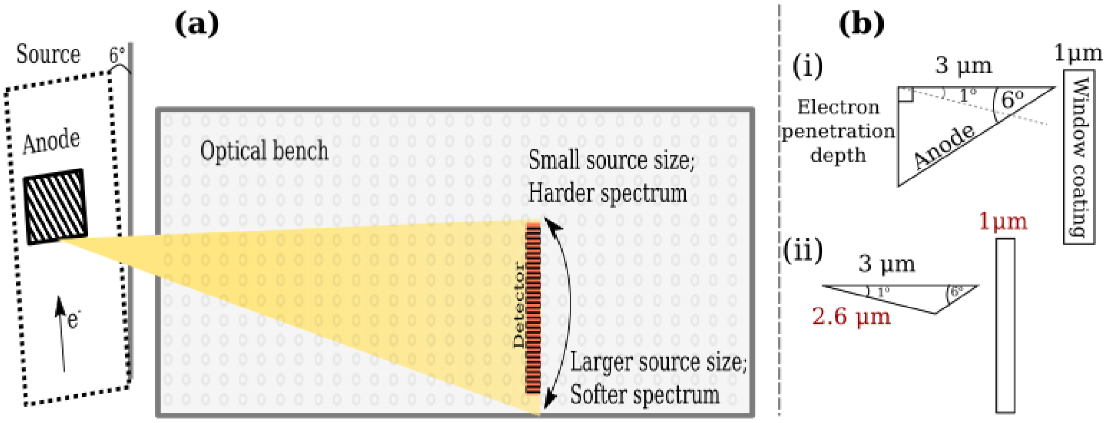

Figure 5.12: (a) Illustration of the variation in source size and average beam energy as a function of viewing angle. (b) Basic geometric model for determining the different amounts of tungsten that filter the beam as a function of the angle at which the source is viewed; (i) is the face-on view, while (ii) is for the source being viewed from 1°.

Remembering that ≈ 3 μms of tungsten filtration led to a good match between simulation and experiment in the Hamamatsu experiments, and that this inherent filtration may have increased due to coating of the source window (assuming an upper limit of 1 μm additional filtration), we can estimate the possible variation in filtration with a simple geometric model of the anode. Construction of triangles, shown in Fig. 5.12 (b), then allows for an estimation of how much tungsten is filtering photons being emitted across the 1° arc being considered. The estimated range of tungsten thickness is then ≈ 0.5 μm regardless of which initial filtration is assumed, and is thus smaller than the inherent uncertainty in filtration. The inherent tungsten thickness (seen from the DLE) was thus modelled as being 4 μm, decreasing to 3.5 μm at the DRE, making this one of the smallest changing physical parameters across the FoV. For completeness, the effect was built into both models, but appears to be of little significance overall.

To implement the Heel effect and variations in source size, consider first the Monte Carlo model. In McXtrace, the emission point of a photon is first determined by generating a random number and using a cumulative density function (CDF; see the inset plots in Fig. 5.7 (a)) that describes the measured source profile to determine the point of emission, then the photon's initial direction is randomly generated in the same way. By swapping the order of computations such that the angle of emission is determined first, the photon may be weighted by an appropriate amount of tungsten filtration before it has left the source component. Further, the source's size may be allowed to vary by re-scaling the x axis of the CDF according to a pre-determined function of the emission angle. This method is straightforward and efficient.

Implementing the Heel effect in the wave optics model is also straightforward, however the variations in source size are more difficult to recreate. To account for spectral changes, instead of weighting all pixel intensities in the same way with a single spectrum, the pixel's position in real space may be used in determining a spectrum that corresponds to the appropriate amount of tungsten filtration. For the variable source size, the blurring effect is achieved by a convolution, so only one source function may be used at a time for each pixel. If a given region of pixels, and the local change in source size, is small, a single well-chosen single source size may be used. For large FoVs, however, groups of smaller pixel regions must be simulated one at a time and convolved with the appropriate source function, then recombined to form the larger image.

How the source size varies as a function of the view angle can be extrapolated by comparing the widths of ICs output by the model with the experimentally measured widths, and is shown as a smoothed fit in Fig. 5.13 (a), with parts (b) and (c) comparing the simulated and measured IC widths and offsets due to this variable source, and one whose size is constant for all viewing angles. Also shown in plots (d) and (e) is the effect of variable mask septa densities on the IC offset for the increasing source size: the effect is greatest near the DLE, where there is negligible angular filtration, and negligible as the viewing angle increases. The simulated offset, which is mostly unaffected by these relatively small changes in source source, exhibits the same trend seen experimentally and deviates from the measured values only by 3-4%, indicating that the model has captured most of the significant physical mechanisms.

Figures 5.14 and 5.15 conclude this section on “primary” effects by comparing the experimentally measured absorption and refraction of a sapphire wire with the simulated equivalents predicted by the basic model, and by a model which accounts for angular filtration, Pixirad’s energy response and the changes in source size and spectrum. The wire radius was 125 μm, the spectrum was that of a 60 kVp tungsten source filtered by 0, 2 mm, 4 mm and 8 mm of dural. The former figure demonstrates that the refined model predicts the absorption signal of the wire with greater accuracy, while the latter figure shows that the basic and refined model are both capable of producing the wire’s phase profile, however the refraction angles at the wire edges are over-estimated in both cases. The subsections that follow describe model changes only applicable to McXtrace that aim to bridge the gap between simulated and experimental IC offset intensities.

5.3.4 Refraction through and reflection from gold septa in EI masks

Refraction of photons inside the mask components can affect their total path length through gold, and if the incident angle is below the critical angle ($\theta_{\text{crit}} = \sqrt{2\delta}$), reflections may occur, which may increase the overall width of the beamlets if the propagation distance is sufficiently long. These effects are illustrated in Fig. 5.16 (a) and (b). Here, I model refraction only using McXtrace, as it is naturally suited to 3D interactions, however it could also be modelled in wave optics if small discrete propagation distances, or “slices”, through the mask component are considered.

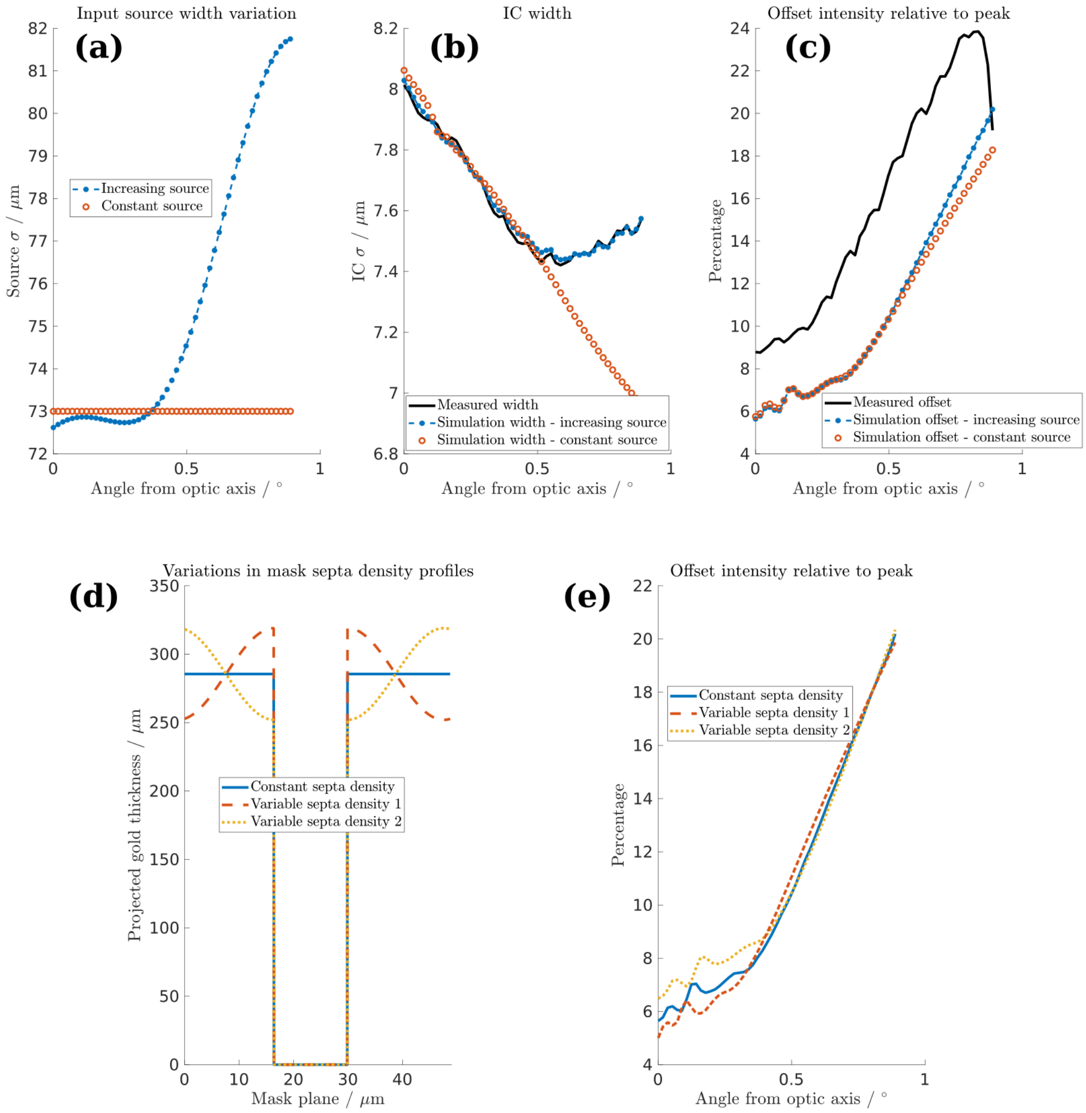

Figure 5.13: (a) Fitted and static source width as a function of the viewing angle; (b) and (c) compare simulated and experimental IC widths and offsets respectively for a 60 kVp tungsten spectrum. The effect of having variations in mask septa density, shown in (d), on the IC offset are shown in (e). The Heel effect is included in the relevant plots.

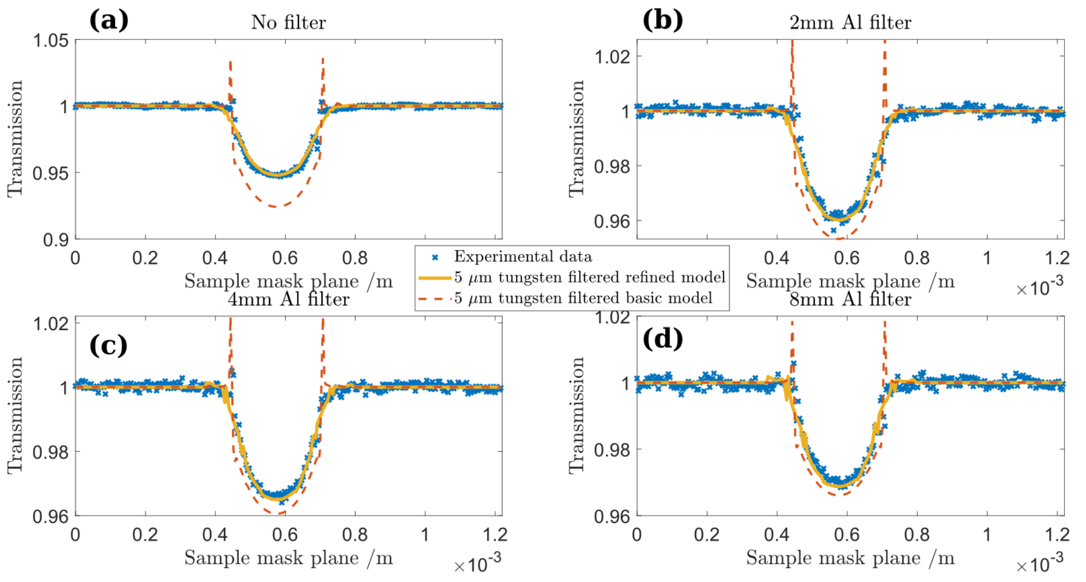

Figure 5.14: Comparison of the absorption profiles of a sapphire wire for (a) 0, (b) 2 mm, (c) 4 mm and (d) 8 mm dural filtration and the simulated equivalents produced by the basic and refined wave optics models.

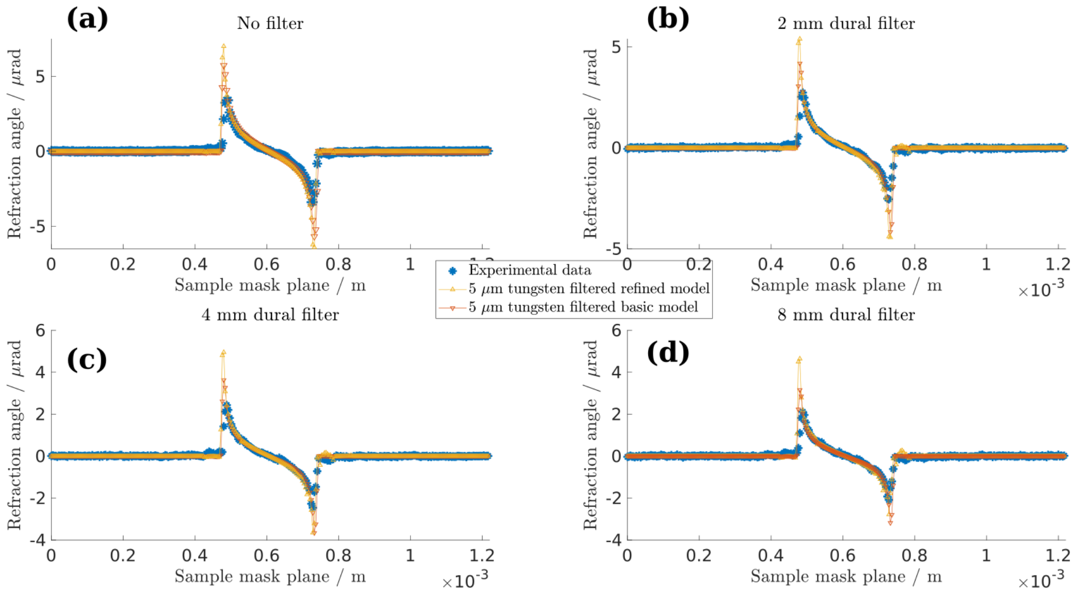

Figure 5.15: Comparison of the refraction profiles of a sapphire wire for (a) 0, (b) 2 mm, (c) 4 mm and (d) 8 mm dural filtration and the simulated equivalents produced by the basic and refined wave optics models.

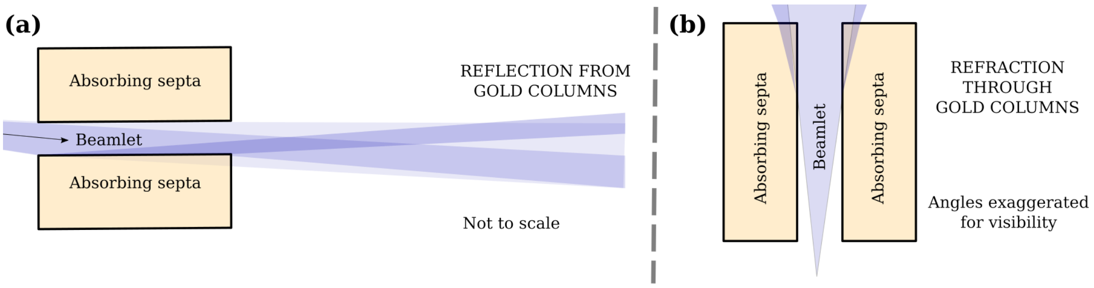

Figure 5.16: (a) Possible effects of reflection on the beamlet may include broadening if propagation distance of beamlet is long after the mask. (b) Slightly increased path length through gold columns due to refraction, increasing the effects of angular filtration by some amount.

Refraction between different media within the mask object were handled via Snell's law, while reflections required the introduction of a new function. X-rays reflect mainly from high-Z materials (i.e. heavy metals) and only do so for very shallow angles of incidence. The reflection coefficient, $R(\theta)$, for an x-ray beam falling at an angle θ on a solid surface is given by the Fresnel formula [85]:

$$R(\theta) = \frac{(\theta - \theta_1)^2 + \theta_2^2}{(\theta + \theta_1)^2 + \theta_2^2} \exp\left(-4k^2\sigma_{\text{rough}}^2 \sin^2\theta\right), \tag{5.3}$$

where $\theta_1 = 2^{-\frac{1}{2}}[((\theta^2 - 2\delta)^2 + (2\beta)^2)^{\frac{1}{2}} + \theta^2 - 2\delta]^{\frac{1}{2}}$, $\theta_2 = 2^{-\frac{1}{2}}[((\theta^2 - 2\delta)^2 + (2\beta)^2)^{\frac{1}{2}} - \theta^2 - 2\delta]^{\frac{1}{2}}$, σ_{rough} is the root-mean-square height of the material roughness, k is the wavenumber and δ and β are the real and imaginary parts of the refractive index.

The surface roughness of the gold septa could not be measured directly, however, as scientists at microWorks were investigating their electroplated structures as possible x-ray mirrors, they were able to provide an estimate of the surface roughness as being 15 nm. As Fig. 5.17 (b) shows, this reduces the likelihood of reflections for all but the lowest energy photons nearly to zero.

The variation in simulation outputs for illumination curves where refraction is enabled or disabled, for pixels along the optical axis and at the edge of the Pixirad

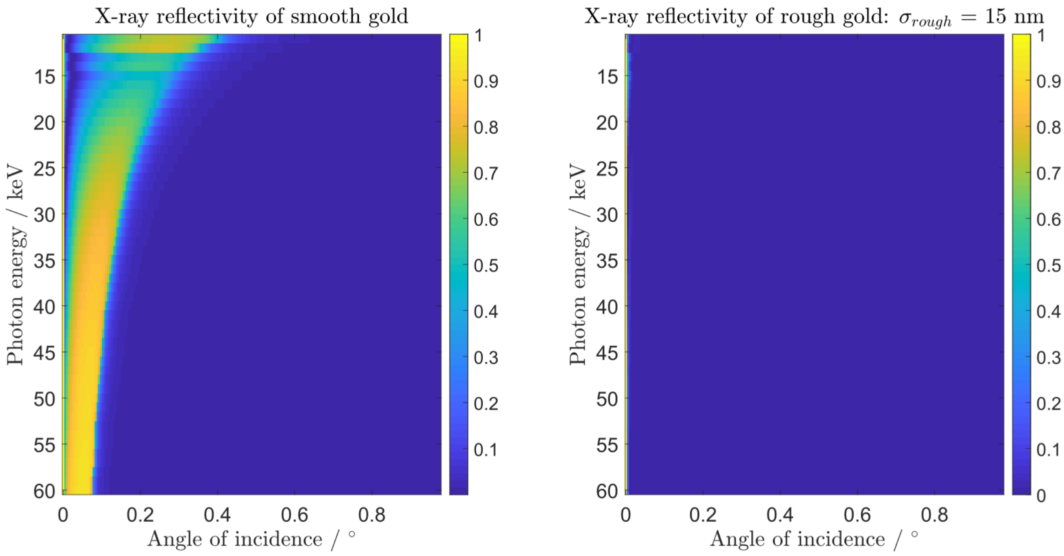

Figure 5.17: Reflection coefficient heat-maps of x-ray photons from SU-8 incident on (a) smooth gold and (b) gold with root-mean-square surface roughness of 15 nm.

FoV, is shown in Fig. 5.18. Note that in producing this figure, the mask septa are of uniform density, and the Heel effect and multi-counting physics were not enabled in order to isolate the effect of refraction only.

Along the DLE, the IC offset does not increase noticeably when refraction is included, however the effect is significantly greater towards the right edge of the Pixirad FoV, where the IC offset is increased by ≈5%. This difference in IC offset is similar to that due to multi-counting of photons, indicating that a model using only the projection approximation for the masks, even if accounting for a curved wavefront, may be insufficient to recreate experimental measurements.

5.3.5 Scattering through air

The EI masks are, by design, anti-scattering grids. However, scattering through air was investigated here as a possible mechanism for increasing the flux arriving at the detector while the masks are misaligned. The procedure for implementing this in McXtrace is similar to that described by Busi *et al.* [86]. An "air-block" component is placed between the source and M1, and also between M1 and M2.

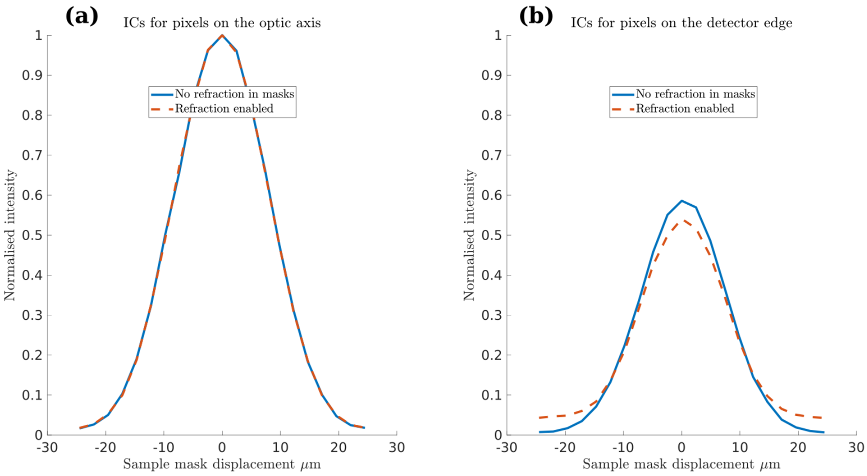

Figure 5.18: Effect of internal mask refraction physics on the IC for pixels on (a) and far from (b) the optic axis.

Photons in these components move in discrete amounts depending on the total thickness of the component, and after each movement a scattering event may occur. The function used to determine whether or not scattering occurs does so by comparing a randomly generated number against the probability of scattering through a given volume of air coherently:

$$P(\text{coherent}) = 1 - \exp\left(-s_i \rho_{\text{air}} \sigma_{\text{coh}}(E)\right), \tag{5.4}$$

and incoherently:

$$P(\text{incoherent}) = 1 - \exp\left(-s_i \rho_{\text{air}} \sigma_{\text{inc}}(E)\right), \tag{5.5}$$

where ρ_{air} is the density, s_i is the path length of the ray through the i^{th} volume and $\sigma_{\text{coh}}(E)$; $\sigma_{\text{inc}}(E)$ are the coherent and incoherent scattering cross sections, respectively, which were obtained from the NIST database. The probabilities of scattering coherently and incoherently through 0.4 m of air (the distance between sample and detector masks in a standard EI setup), and the Thompson and Klein-Nishina distributions, are shown in Fig. 5.19. The scattering angles in both the coherent and incoherent case are determined in the same way as described by Beni

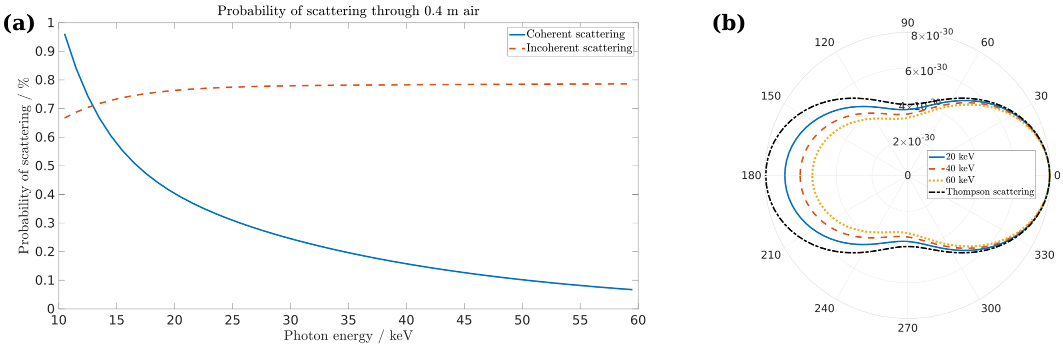

Figure 5.19: (a) The probabilities, as a function of photon energy, of coherently and incoherently scattering through 0.4 m of air - the distance between M1 and M2. (b) The angular energy dependent distributions of the scattering cross sections for Thompson scattering (black dot-dashed line) and incoherent scattering (other lines).

et al. [87]. In the event of coherent scattering, the angles are determined relating a random number to a CDF described by:

$$\mathrm{CDF}_{\mathrm{coh}} = \frac{1}{2} - \frac{1}{8}\cos^3\theta - \frac{3}{8}\cos\theta. \tag{5.6}$$

For incoherent scattering, the energy α of a scattered photon, relative to the unscattered energy, α_0, is first related to a random number ξ by the equation:

$$\alpha = \frac{\alpha_0}{1 + (\frac{\alpha_0}{1+0.5625\alpha_0})\xi + \big(2\alpha_0 - (\frac{\alpha_0}{1+0.5625\alpha_0})\big)\xi^3}, \tag{5.7}$$

which arises from the Klein-Nishina formula. The scattering angle may then be determined by the relation:

$$\frac{\alpha}{\alpha_0} = \frac{1}{1 + \alpha_0(1 - \cos\theta)}. \tag{5.8}$$

Upon simulating the ICs with these air-blocks in place, however, the effect of air-scattering on all IC parameters was found to be negligible across the FoV for the standard geometry of the EI setup. Experiments using low x-ray energies or long setup lengths may measure some moderate effects due to scattering in air, but for the purposes of this analysis, it may be safely neglected.

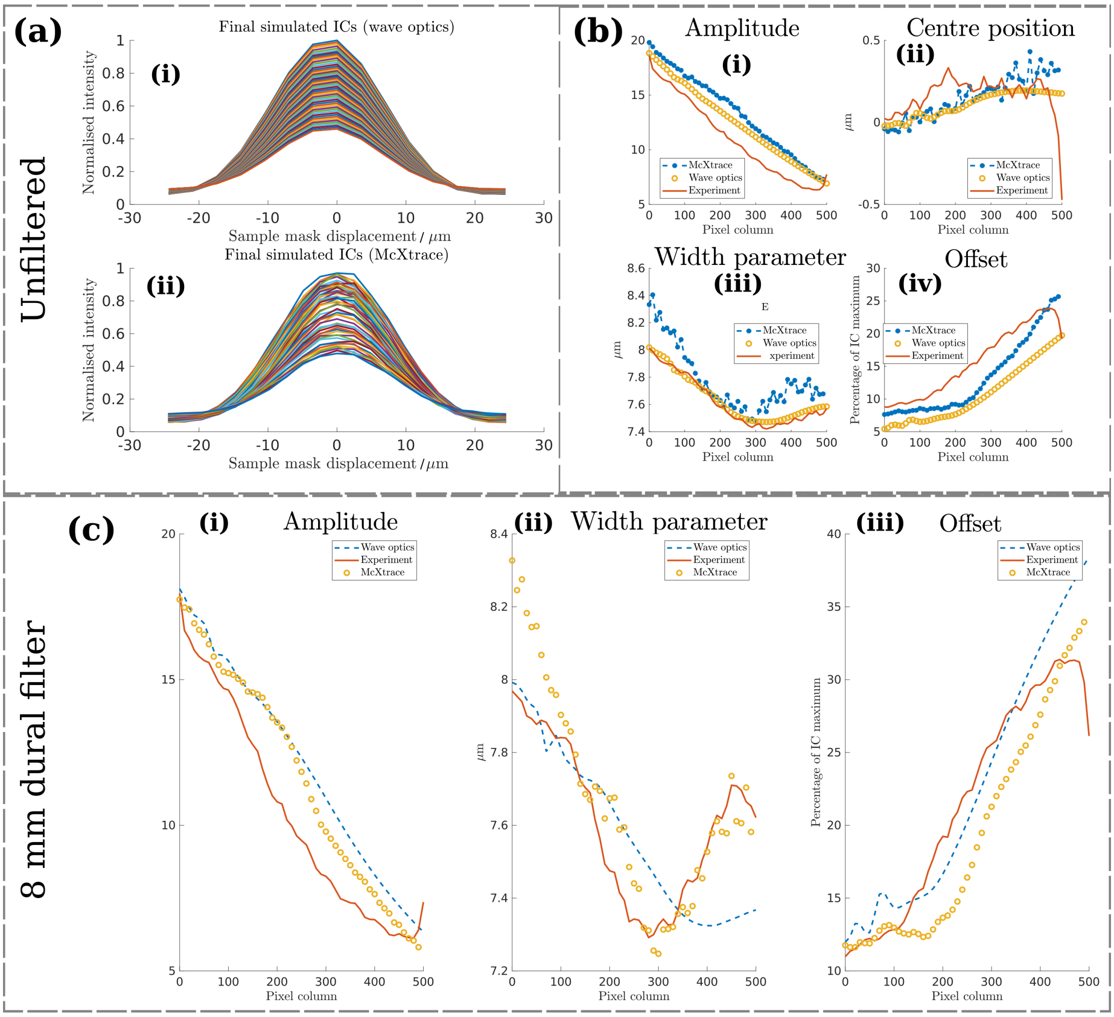

Figure 5.20: Panel (a): (i) and (ii) show ICs produced by the refined wave optics and McXtrace models, respectively, normalised by the DLE IC peak. Panel (b): the amplitude (i), IC centre position (ii), IC width parameter (iii) and IC offset (iv) for the simulated and measured ICs using an unfiltered spectrum. Panel (c): the amplitude (i), width (ii) and offset (iii) for the simulated and measured ICs using an 8 mm dural filtered beam.

Fig. 5.20 shows a collection of simulated ICs and their fitted parameters, in addition to the measured parameters, for the unfiltered and maximally (8 mm dural) filtered cases. Panel (a) shows example IC outputs from the wave optics and Monte Carlo models, normalised by the peak value of the IC simulated in the same position as the DLE, for an unfiltered 60 kVp beam. Panel (b) shows the corresponding IC parameters, both measured and simulated, for amplitude (i), centre position (ii), IC width (iii) and offset (iv). The trends for the simulated parameters of (i) - (iii) are generally in good agreement with the measured values, whereas the offset parameter is predicted by models as being slightly lower than is measured, but this deviation decreases - particularly in the Monte Carlo model - as the viewing angle increases. Panel (c) shows the amplitude, width and offset parameters predicted by the wave optics model, along with the measured values, for the 8 mm dural filtered beam; here the simulated and measured amplitudes and offsets are in agreement, with the latter indicating that refraction of x-rays through the gold septa becomes less of a discrepancy between model and experimental settings for high energy photons. Differences in the measured and simulated width parameter, however, are evident, which could be due to chromatic structure in the source spot being selectively filtered, or perhaps due to variations in the gold septa's density resulting in more (high energy) x-rays being transmitted as the angle of incidence between wavefront and mask increases.

Overall, the effects of angular filtration, variable source size, detector response, internal refraction within the masks and the Heel effect are all seen to affect ICs with varying levels of significance, but the cumulative effects are important when considering large FoVs, and cannot be neglected. As the average energy of the spectrum increases, the effects of angular filtration and detector response begin to dominate the IC offset parameter, as evidenced by the one produced by the wave optics model - which neglects internal mask refraction - beginning to match the experimental offset. Variations in mask septa density may lead to some minor changes to the IC parameters, but as only the bulk density is known, this potential effect was not examined thoroughly.

5.4 A multi-slice wave optics model for wave optics based dark field simulations

In comparison with Monte Carlo models, wave optics models are entirely deterministic and, as a result, can be computationally efficient since there is no noise due to an insufficient photon count, which is occasionally a drawback of Monte Carlo methods. Complicated samples may be simulated in the current 1D EI model, however there are two restrictions:

- In the 1D case, simulating objects whose size varies over small regions (i.e. comparable to the mask apertures) in two dimensions (e.g. microspheres as cylinders) is a poor approximation.
- The projection approximation for complex samples in 3D space must be valid [88].

A simulation tool developed recently within the Advanced X-ray Imaging group at UCL [89] overcomes both of these issues by partitioning a sample into slices thin enough such that the projection approximation is valid. In this way, the projection approximation is applied to each slice in sequence. The code is inherently 3D ready and, in collaboration with the author, was adapted for use in conjunction with my refined EI model that accounts for changing system parameters in different positions of the FoV.

The models were combined as shown in Fig. 5.21. The refined EI model calculates a waveform corresponding to a plane wave that has been transmitted through M1. The sample mask transmission function is a projection of a mask rotated through some angle, as described previously, depending on which pixel region in the Pixirad FoV is being simulated. For each energy, the sampling of the wavefront, as well as the attenuation of the beam by the mask, is adjusted

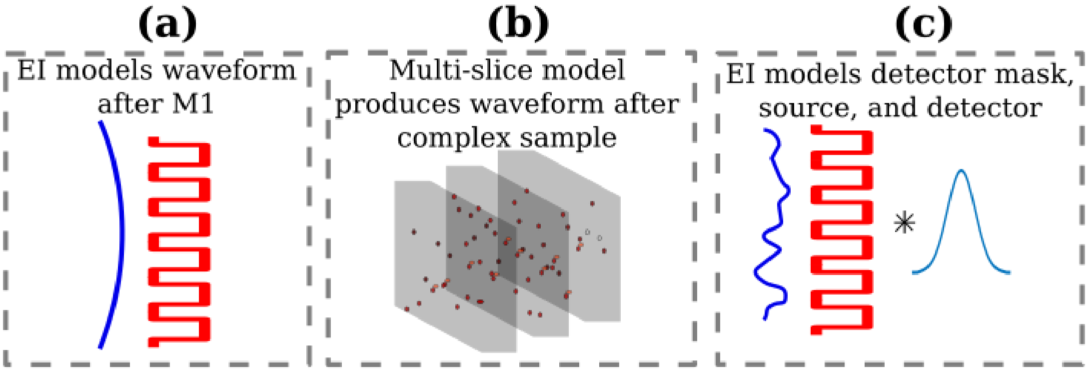

Figure 5.21: Scheme for combining multi-slice and refined wave optics model for dark field EI simulations: the refined model produces a wavefront immediately after the sample mask, which is used as input to the multi-slice code. After propagating the wavefront through the sample and to the detector mask plane, the refined EI model processes the waveform to produce an IC.

to ensure that aliasing is negligible. In representing the sample - in this case an arrangement of microspheres suspended in water - the multi-slice code is executed. The waveform is multiplied with the projected transmission function of each sphere, and then propagated from the plane of the sphere's centre to that of the next sphere using angular spectrum propagation. Finally, the wave is propagated from the end of the sample to the detector plane, where a convolution on the field intensity to account for source blurring is performed, then the EI model again provides a transmission function for M2. This is applied to the intensity matrix before convolutions with the pixel and PSF functions take place as normal.

In order to reduce the computation time of the simulation, which guarantees correct sampling of the field, several optimisations were made to the code, as listed below.

- In the original version of the code, slice thicknesses were set to be equal to the spacing between spheres with adjacent axial coordinates. This was altered such that slices of thickness 500 μm were considered. This required that each sphere within the slice be represented by the projection function corresponding to the slice in which it is located. Furthermore, angular spectrum propagation is used to propagate the field by a distance of 500 μm for each slice considered.

  - The effect of using thicker slices was investigated by comparing the IC outputs for slice thicknesses ranging from 1 μm to 500 μm. The ICs in a 5×5 pixel grid were found to remain constant, as illustrated in Fig. 5.22. The discretisation having little impact on the resulting intensity is in agreement with the findings reported by Malecki *et al.* [90].

- As the complex amplitude matrices could be as large as 3 GB in some cases, the size of the area being sampled was restricted to a 5×5 pixel region for all energies, with the sampling being increased as necessary; this reduced the memory requirements by more than three times.

- ICs were acquired by shifting the detector mask over one mask period, instead of the sample mask, thus removing the need to repeatedly simulate the sample, which was the most computationally demanding step. This was found to produce the same ICs as previously output by the refined 1D model, in which the sample mask was translated.

- As the multi-slice code iterates for all energies in a spectrum being considered, the size of each energy bin was increased from 1 keV to 2 keV.

  - The error in average beam energy due to this change is less than 0.5 keV for both the unfiltered and 8 mm filtered spectra.

- Microsphere shells were not modelled, with the spheres instead being treated as voids (as was originally modelled in the method by Millard *et al.* [80]).

Four concentrations of microspheres in water, for 0, 4 mm and 8 mm dural filtration applied to a 60 kVp tungsten spectra were simulated. These concentrations corresponded to 100%, 50%, 10% and 5% of the stock concentration described in the previous chapter (where 100% concentration implies 2.3% fill by volume),

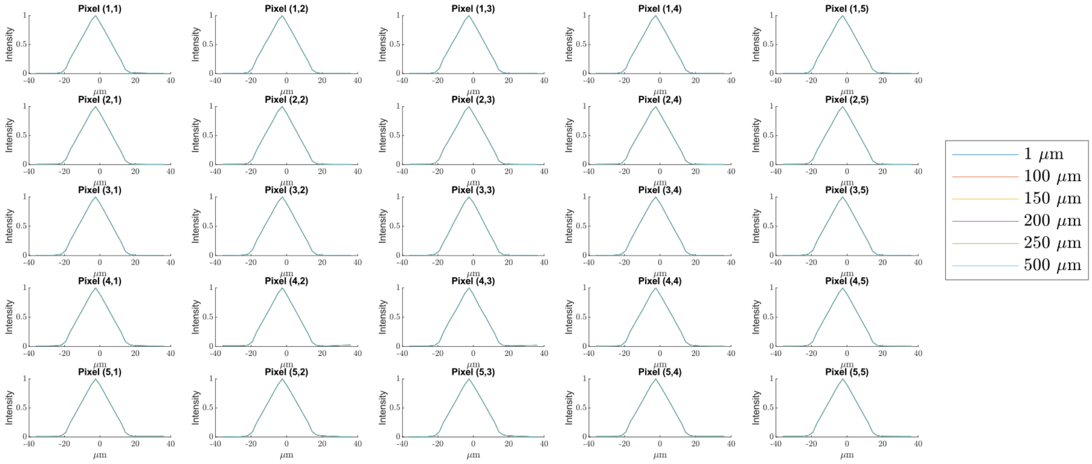

Figure 5.22: Effect of increasing the size of discrete slices used in the multi-slice wave optics code on IC outputs. Each subplot corresponds to individual pixel ICs where discretisations of 1 μm, 100 μm, 250 μm and 500 μm are used in the simulation. These ICs are monochromatic 30 keV - the approximate mean energy of the unfiltered 60 kVp beam - with a point-like source and a detector with a delta function PSF in order to ensure any changes are due to the discretisation alone.

and were simulated in the same detector FoV positions as in those experiments (see Fig. 4.13 (a)); the maps of sphere coordinates were generated in the same way as described in Chapter 3. Simulated mask parameters were those that have been described for the Pixirad masks in this chapter, with a uniform density septa of 90% solid gold and septa thicknesses as measured. The simulated area was a square of sides 310 μm, or 5 pixels in both the horizontal and vertical directions.

Transmission and dark field signals were retrieved on a pixel-by-pixel basis using the same method described in Chapter 4 with 21 sampling points on the IC, and also using the three-Gaussian method developed by Maughan-Jones *et al.* [91], with the retrieved signals - shown in Fig. 5.23 - being equivalent. As in Fig. 4.12, the transmission and USAXS signals of all concentrations decrease, in general, with increasing dural filter thickness. The USAXS signals produced by the different concentrations are of the same magnitude seen experimentally, and have mean values that do not "cross over" each other as the filter thickness increases. Except for the 10% concentration, which has a lower retrieved signal than the

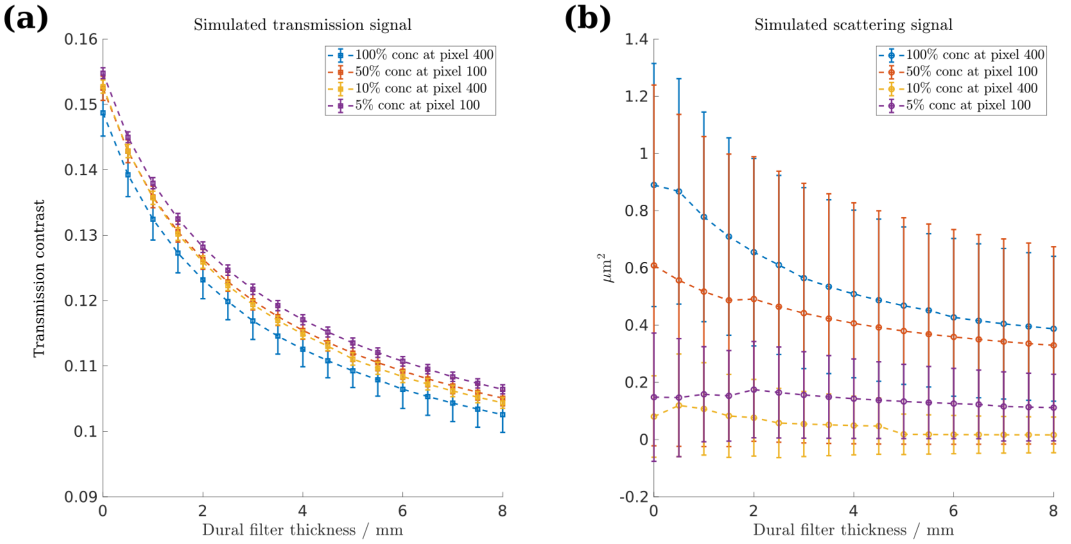

Figure 5.23: Retrieved transmission (a) and dark field signals (b) from wave optics simulation of different concentrations of microspheres in water, accounting for the angular filtration, variations in source size, and the Heel effect, for increasing dural filter thickness. Each concentration was simulated as being in the same FoV position as in experiments - see Fig. 4.13 (a).

5% concentration, signals produced by the different phantoms are correlated with their microsphere concentrations. In addition, the range of scattering uncertainties for all concentrations, or the spread of retrieved signals over the 5×5 pixel grid, is very large relative to the mean signals. The reasons for these two observations are as follows:

- The retrieval:
  - The average width parameters of ICs simulated in the absence of a sample, for pixel numbers 100 and 400, are ≈ 8.55 μm and ≈ 8.14 μm, with 95% confidence regions being on the order of 0.04 μm; the widths of ICs simulated *in the presence of a scattering sample* are on the order of ≈ 8.6 μm and ≈ 8.3 μm, for the 50% and 100% concentrations respectively. As the scattering signal is the difference between squared width parameters of the sample and flat ICs, only scattering signals produced by the highest concentrations, or greater, can be *distinguished* while, although the lower concentrations may generate some detectable

  dark field signal, they cannot be well separated from each other by those signals.

  - Absorption due to a sample cannot be well separated from the effects of scattering, as these signals affect the ICs in “opposite” ways, depending on where the IC is being sampled - in general, scattering redistributes the area under the IC, decreasing the peak value and increasing the offset, whereas absorption decreases the IC uniformly. This mixing of signals is reflected in the size of the error bars associated with the transmission contrast in Fig. 5.23 (a), which are greatest for the highest concentration of microspheres. That the IC offset varies significantly across the FoV also makes retrieval of a consistent scattering signal more difficult.

- Differences in mean energy reaching the detector for the different pixel positions.

  - In the absence of any samples for the two pixel positions, the average energies are shown for each IC position in the unfiltered and 8 mm dural filtered cases in Fig. 5.24. While possibly small in absolute terms, this effect would become relatively more important when signals from low concentrations of microspheres need to be retrieved. When considering this figure, it should be noted that, as the masks become misaligned, the high energy photons transmitted through the mask septa do not contribute to the dark field signals, rather, they contribute only to the background.

- Different microsphere ensembles.

  - As described above, the sensitivity of the IC width fitting is required to be very high; different numbers, and placement, of spheres within a given sphere map, and especially between different maps, lead to vari-

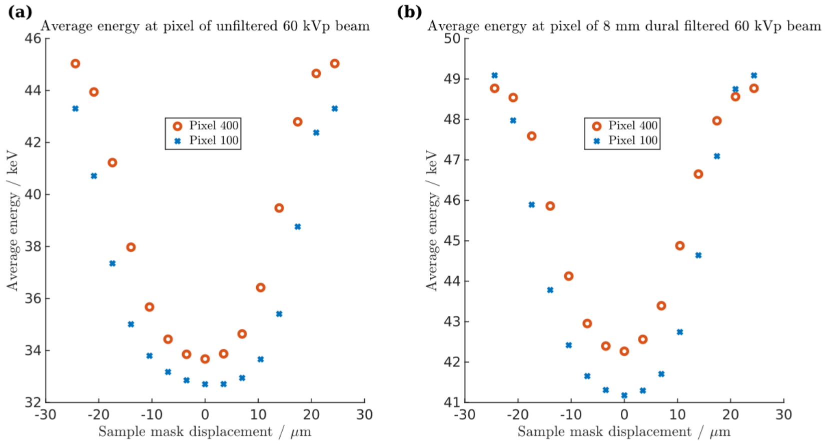

Figure 5.24: Average energy of spectra arriving at the detector plane for pixels 100 and 400. Each position of the IC is considered and (a) corresponds to an unfiltered 60 kVp tungsten spectrum, while (b) corresponds to the same beam filtered by 8 mm dural.

ations in scattering signal that arrive in any given pixel. The accuracy of average scattering signals could perhaps be improved by simulating larger volumes of microspheres in water, though this would increase the computational load significantly.

In terms of the dark field signal, Fig. 5.23 (b) shows that, if only the mean signal is considered, different concentrations of microspheres may be distinguished if the absolute concentration is sufficiently high. Indeed, comparing this figure with Fig. 3.6, which showed considerable variation in retrieved scattering signals for different sphere concentrations, we are assured that microspheres do produce USAXS signals at high energies, and that different concentrations may be separated through comparison of their dark field signals in an optimised EI system. Taking into account the spread of scattering signals shown by the error bars in Fig. 5.23 (b), however, implies that distinguishing different microsphere concentrations with this EI system has several inherent difficulties. First, that there is a minimum detectable scattering distribution that depends on the accuracy, and values, of the fitted IC parameters; this is exemplified by the 10% concentration's scattering signal, which falls within a “gray zone” of detectability, as its error bars extend below zero and the mean signal is the lowest of those simulated. Second, noise - and by extension, the position in the FoV, which determines the overall intensity due to angular filtration - will have a significant effect on the retrieval, meaning that larger RoIs may be required in order to produce a statistically significant average scattering signal. Third, samples placed in different areas of the detector FoV produce different transmission and scattering signals; this could be accounted for through modelling, where the work required would potentially be extensive, or by calibration of a scattering sample in the experimental environment. Optimisation of a lab-based setup may potentially be achieved by reducing the initial width of the system's illumination curve, which would increase the sensitivity to scattering, and to find ways of reducing the experimental offset intensity as much as possible, thus decoupling the effects of absorption and scattering in the retrieval phase. These could both be accomplished through a variety of methods, such as changing the system geometry, decreasing the widths of mask apertures, collimating the source, or finding ways of increasing the density of electroplated gold.

5.5 Conclusions

The active FoV of the Pixirad detector is approximately 3 cm long, but EI characteristics - as seen in the illumination curve function - vary significantly over this region. Thick mask septa, and the high energies employed during these experiments, have made these effects particularly evident, and a sophisticated model was required in order to understand the physical mechanisms at play in the system. In order of significance, these effects are:

- Angular filtration of the beam due to the thick mask septa, which must be accurate if simulating a large FoV;
- Variations in source size, energy and flux due to the system geometry (due to the Heel effect and inverse square law, respectively);

- The detector response as a function of both photon energy and how closely the photon arrives to a pixel boundary;
- Refraction within the mask structures at the aperture - septa interfaces, which become more important as the angle at which the source is viewed increases, particularly for low energies, as refraction increases the angular filtration effect.

Each of the above effects were incorporated into two existing models based on wave optics and Monte Carlo techniques. Accurate spectral modelling - affected by the mechanisms described above - benefits retrieval of absorption signals, whereas phase retrieval of wire profiles is not noticeably improved by the refined models compared to the basic versions. The IC parameters, which characterise the EI system, were recreated well across the FoV in both models for all filter thicknesses, though small deviations between simulation and experiment exist, these are likely due to small-scale variations of the real mask parameters across the FoV.

Concerning the retrieval of weakly scattering ensembles of microspheres, a model for multi-slice dark field simulations was used in combination with the refined EI model to virtually recreate the conditions of microsphere scattering experiments described in the previous chapter. The results of this investigation suggest that, if the difference in microsphere concentrations is sufficiently large (the threshold for which depends on the spectrum and IC parameters), a lab-based EI system may be capable of distinguishing them under certain conditions, namely that their positions in the FoV be accounted for, and that the accuracy of fitted IC parameters is sufficiently high - the requirements of which, again, depend on the magnitude of scattering signal being considered.

The implications of this refined model, and the experimental data they recreate, are that if large fields of view are required in conjunction with current designs of thick absorbing masks, angular filtration is likely to reduce the system's performance. Possible applications of the model exist in both EI and grating interferometry, and would be especially useful for predicting the performance of new mask or grating designs. In-house, the model may be useful when considering ways to optimise existing EI systems for phase and dark field imaging. Further research regarding the effects of the IC offset (produced by the physical mechanisms described above) on the retrieval algorithm's accuracy may also be beneficial, as this is the IC parameter that varies most significantly within the EI system's FoV.

6

Conclusion and future work

The work presented in this thesis explores the feasibility and inherent challenges of edge illumination (EI) based X-ray phase contrast imaging (XPCi) with high x-ray energies to produce images of good quality while maintaining a constant dose. The motivations for the work are derived, in part, from successful dark field imaging experiments of different concentrations of microspheres [80] using synchrotron based ABI and hence repeating those measurements in an EI system with thick mask septa which, if successful, would have potential applications in a variety of industrial, security and medical settings. The investigation was carried out through a combination of experimental XPCi measurements, dedicated measurements of individual EI optical components (masks) themselves, and extensive modelling of the EI system in various settings. In this chapter, summaries of the thesis' main findings are presented, followed by suggestions for further research that could build on these results to better optimise the EI system for a variety of applications.

6.1 Conclusion

XPCi techniques, which generally produce superior images compared to traditional x-ray attenuation images, are on the verge of being adopted in a variety of medical and industrial applications. Their use, however, has often been restricted to synchrotron facilities, with limited availability, high costs and fixed locations restricting their use. Translating from synchrotron to in-house, or research facilities, while maintaining image quality, remains one of the key challenges in XPCi research. In particular, fast, dose-constrained measurements and rapid analysis of data for large, complex samples, *ex-* and *in-vivo*, are perhaps the most significant barriers to the widespread use of XPCi in clinical or commercial settings.

X-ray sources, x-rays, their interactions with matter and their use in imaging were examined broadly, after which several XPCi methods were described, with a focus on EI. To provide a basis upon which fine details of the EI system could be discussed, the technologies used in x-ray imaging detectors, along with methods used in the creation of XPCi masks and gratings, were also described. EI setups in experimental and simulated environments were used in order to demonstrate the possibility of high energy phase and dark field imaging; components used in these EI systems, and their positioning therein, were examined in detail to understand how the system behaviour changes under a variety of conditions. With an understanding of why certain limitations arise, it is hoped that the knowledge may be used to find new implementations that overcome these limits.

6.1.1 Dark field imaging with high energy synchrotron radiation

A description of the experimental setup was provided, followed by an overview of the simulation tool, McXtrace, that was used to model the system. Illumination curves (ICs), which characterise EI systems, were acquired for all pixels that were not obscured by the detector mask, with both the ensemble and individual curves being used in two different retrieval approaches. The use of individual pixel ICs in this case presents an opportunity to use fewer input frames than are normally required by retrieval algorithms.

Experiments that used monochromatic 50 keV photons were performed first on standard wire samples, which allowed for a straightforward comparison of the two retrieval approaches where single-frame acquisitions achieved equal or better signal to noise (SNR) values of the wire than the "standard" two-frame approach, despite using only half of the data set. The fact that the noise in retrieved images was lower even while using half the data set was attributed to errors in the IC sampling positions used, which affected the retrieval algorithm more in the two-frame case. Microspheres of increasing concentrations in ultrasound gel were then imaged at multiple sampling points on the IC, and the reduced-frame (two in this case) approach was again compared with the standard approach (which requires three frames). Both retrievals enabled the recovery of dark field signals whose magnitude increased with the concentration of microspheres. It was found, however, that the uncertainty in retrieved dark field signals was significantly greater in the reduced-frame case compared to the standard three frame one.

A combination of analytical and McXtrace modelling was then used to understand why this was the case. The retrieval algorithm was tested against all possible sampling positions, revealing that those used in-experiment were sub-optimal when considering a reduced-frame implementation. As the experimental setup in the reduced-frame case shared similarities with that used in beam tracking (BT), a comparison of both setups was also carried out, with the retrieval outputs being of similar quality. Finally, McXtrace was used to demonstrate that a single frame could be used to retrieve scattering signals where the sampling position of the IC was chosen according to best-predictions from the analytical model.

6.1.2 Lab-based XPCi experiments with increasing mean energies.

In some imaging scenarios, such as those found in clinical settings, x-ray beams are polychromatic and samples can be dense, have significant depth, or exhibit some combination thereof. This can lead to inefficient use of photons due to the majority of low-energy x-rays being absorbed by the sample and not contributing to image formation. A possible solution is to pre-filter the beam such that these low energy rays do not reach, and hence do not deposit, any unnecessary dose in the sample. The disadvantage of filtering is that the contrast of materials typically decreases with the increasing average energy resulting from the filtration itself.

Experiments were performed with two different systems employing two different detectors (a CdTe single photon counter - Pixirad - and an indirect conversion CMOS-based flat panel - Hamamatsu) in order to determine how the SNR, for a variety of wires of differing materials imaged using an EI system, depends upon the amount of filtration applied to a 60 kVp tungsten anode beam. Different mask designs, host media, dose and noise constraints were considered, with a wave optics model being benchmarked by the experimental measurements. Samples expected to exhibit ultra-small-angle x-ray scattering (USAXS) were also imaged with the system that was expected to be more suited to high-energy x-rays - the “Pixirad system” - due to the thick septa used in the masks and the supposedly “flat” energy response of the Pixirad detector. Good agreement was found between experimental and simulated data for the “Hamamatsu system”, with the model then being used to make predictions of how SNR for different materials measured through water varies with increasing average energy. Simulations meant to model the Pixirad system were only partially successful, whereby the best agreement between simulated and experimental results was achieved by assuming the values of some physical parameters as being excessively different to their nominal ones, which was considered unrealistic.

The SNR for wires in air decreases with increasing energy, with refraction effects enabling detection of wires that would be invisible using attenuation contrast alone. For wires imaged through water, which is often a better representation of imaging *in-vivo* features, the SNR was found to increase initially - due to noise decreasing at a greater rate than wire signals - and then decrease with increasing energy. When retrieving dark field signals due to scattering samples with the Pixirad system, the porous sponge material showed a decreasing signal in air for increasing filter thickness, and had no discernible signal when immersed in water, thus illustrating the finite ability to distinguish materials when immersed in media of similar refractive index. The different concentrations of microspheres produced scattering signals whose large uncertainties made distinguishing them difficult. It was observed that the position in the filed of view (FoV) at which the concentrations were imaged had a significant impact on the retrieved scattering signal, which prompted further investigations.

6.1.3 Model refinements for high energy Edge Illumination XPCi systems

Models of imaging systems are useful for their ability to predict performance of, or discover issues with, proposed implementations. In EI and other XPCi methods, models exist and have been benchmarked against a variety of different experimental settings. However, using standard EI models for the Pixirad experiments failed to adequately capture the system parameters, especially when considering different x-ray spectra. A variety of x-ray based and ultimately direct measurements of the EI masks were performed in order to determine the thickness and density of their absorbing septa. Different physical mechanisms were then incorporated into the Monte Carlo and wave optics models until it became possible to reproduce the system characteristics measured experimentally.

The effects that were added were as follows:

- Mask components were changed from a 2D to 3D implementation that allows for evaluation of angular filtration as a function of mask thickness.
- The density profiles of absorbing mask septa are allowed to diverge from the nominal density of solid gold; this is to account for the difference in density exhibited by electroplated gold.
- Mask aperture fillings of epoxy-resin based SU-8, which harden the spectrum and reduce the beam flux.
- The apparent size of the source is allowed to vary as a function of the angle at which it is viewed.
- The energy response of a photon counting detector is included to account for single photons being counted multiple times if their energy is more than twice that of the lower energy threshold for the detector. This is particularly important in an EI setting, as when the masks are misaligned, high energy photons are predominantly detected, thus increasing the IC offset parameter.
- The Heel effect, which weakly changes the average beam energy across the FoV due to variations in the x-ray anode's self filtering, was included.
- Refraction of photons within mask components; photons refract along septa walls to be directed further into the gold, thus increasing the loss of intensity due to angular filtration.

This refined model was then used in combination with an additional model, developed for wave optics simulations of ensembles of spheres, to recreate the scattering signal results of the previous chapter; the simulated sphere ensembles produced dark field signals of a similar magnitude to those measured experimentally in the lab. Furthermore, in terms of the distinguishability between different concentrations of microspheres, high absolute concentrations appear to be separable by their dark field signals, even when imaged in different parts of the FoV, while smaller absolute concentrations produce dark field signals too small to be cleanly separated. The limitations of dark field sensitivity are due to the width of the IC function, the non-zero offset parameter, noise - each of which vary considerably across the FoV - and, potentially, the size of the RoI being considered, as scattering distributions are non-uniform by their very nature, and larger RoIs may improve the precision of retrieved USAXS signals.

6.2 Future work

A rigorous model capable of simulating complex attenuating, refracting and scattering samples has been constructed and with it, the sensitivity of the EI system to small dark field signals has been explored. An important application of this model would be to explore which system factors (e.g. IC parameters, geometry of setup, mask parameters) impose the most significant limitations in the detection of dark field signals; comparisons of such signals measured in a single FoV location, for example, may result in greater distinguishability, while multiple imaging locations could be used to construct a calibration function that could be verified through experimental work. Techniques developed to predict trends in noise statistics for different levels of beam filtration, while maintaining constant dose, should also be combined with the refined EI models both to improve their accuracy and to improve their predictive capabilities.

In terms of the retrieval methods used, one that corrects for the position in the FoV could potentially be constructed through a calibration function, for instance, the scattering signal of a sample is determined for several pixel positions, and the variation then used to scale subsequently retrieved values. Alternatively, as the Pixirad detector is to some extent capable of photon discrimination by energy, experiments could be performed where the lower energy threshold is gradually increased, and the pixel responses across the FoV monitored, thus revealing more detailed information about the spectrum, which could be used to implement multi-energy retrievals.

As high IC offsets reduce the sensitivity to phase effects, and are determined by a combination of source size, transmission through the masks, and other secondary effects, finding ways of reducing the offset that do not rely solely on thick mask septa should also be investigated. These could begin by considering possible changes to the setup geometry, collimating the source, or reducing the mask aperture widths, to name but a few options.

Secondly a focus on the practical elements of EI, with the aim of minimising the IC offset parameter consistently across the FoV, should also be pursued; potentially this could involve new designs of the masks themselves. However, as new mask formats are difficult to fabricate, it would first be useful to learn how the density profiles of mask septa evolve during fabrication, as this may be advantageous in some designs. Alternatively, it may be possible to develop masks with a defined curvature that matches that of a wavefront, thus transmitting the beam uniformly and without any angular filtration. If both of these pursuits are followed, the possible gains in fast, dose-constrained dark field imaging could be significant.

The practical limitations of the EI setups considered here need not apply universally, and if the above attempts to reduce the lower limit of detectable dark field signals are successful, EI could be used in a variety of medical, security and industrial settings. In particular, considerations of dose, or of minimising exposure time, in relation to SNR should be combined with the refined models, which could be extended even further to compare the efficacy of EI against that of different XPCi systems in a variety of settings, with GI - which utilises gratings fabricated in similar ways to the EI masks - being one possible example.

References

[1] A. Michette. *X-rays: the first hundred years.* John Wiley and Sons, 1996. 26

[2] S. Webb. *Webb's Physics of Medical Imaging.* CRC press, New York, 2012. 27

[3] S. Mobilio, F. Boscherini, and C. Meneghini. *Synchrotron Radiation: basics, methods and applications.* Springer, 2015. 30

[4] M. R. Teague. **Deterministic phase retrieval: a Green's function solution**. *J. Opt. Soc. Am.*, **73**(11):1434–1441, Nov 1983. 34

[5] D. Paganin. *Coherent X-Ray Optics.* Oxford University Press, 2006. 39

[6] G. Greene. *The woman who knew too much: Alice Stewart and the secrets of radiation.* University of Michigan Press, 1999. 42

[7] D. Andisco, S. Blanco, and A. E. Buzzi. **Dosimetra en radiologa**. *Revista Argentina de Radiologa*, **78**:114117, 06 2014. 42

[8] F. A. Mettler, W. Huda, T. T. Yoshizumi, and M. Mahesh. **Effective Doses in Radiology and Diagnostic Nuclear Medicine: A Catalog**. *Radiology*, **248**(1):254–263, 2008. 44

[9] A. Snigirev, I. Snigireva, V. Kohn, S. Kuznetsov, and I. Schelokov. **On the possibilities of x-ray phase contrast microimaging by coherent high-energy synchrotron radiation**. *Review of Scientific Instruments*, **66**(12):5486–5492, 1995. 46

[10] P. Cloetens, R. Barrett, J. Baruchel, J. Guigay, and M. Schlenker. **Phase objects in synchrotron radiation hard x-ray imaging**. *Journal of Physics D: Applied Physics*, **29**(1):133–146, jan 1996. 46

[11] S. W. Wilkins, T. E. Gureyev, D. Gao, A. Pogany, and A. W. Stevenson. **Phase-contrast imaging using polychromatic hard X-rays**. *Nature*, **384**(6607):335–338, 1996. 46, 77

[12] P. Cloetens, W. Ludwig, J. Baruchel, D. Van Dyck, J. Van Landuyt, J. P. Guigay, and M. Schlenker. **Holotomography: Quantitative phase tomography with micrometer resolution using hard synchrotron radiation x rays**. *Applied Physics Letters*, **75**(19):2912–2914, 1999. 47

[13] A. Peterzol, A. Olivo, L. Rigon, S. Pani, and D. Dreossi. **The effects of the imaging system on the validity limits of the ray-optical approach to phase contrast imaging**. *Medical Physics*, **32**(12):3617–3627, 2005. 47

[14] D. Paganin, S. C. Mayo, T. E. Gureyev, P. R. Miller, and S. W. Wilkins. **Simultaneous phase and amplitude extraction from a single defocused image of a homogeneous object**. *Journal of Microscopy*, **206**(1):33–40, 2002. 47, 77

[15] T. E. Gureyev, Y. I. Nesterets, A. W. Stevenson, P. R. Miller, A. Pogany, and S. W. Wilkins. **Some simple rules for contrast, signal-to-noise and resolution in in-line x-ray phase-contrast imaging**. *Opt. Express*, **16**(5):3223–3241, Mar 2008. 47

[16] U. Bonse and M. Hart. **An xray interferometer**. *Applied Physics Letters*, **6**(8):155–156, 1965. 48

[17] A. Momose, T. Takeda, Y Itai, and K Hirano. **Phase contrast Xray computed tomography for observing biological soft tissues**. *Nature Medicine*, **2**, 1996. 48

[18] A. Momose. **Recent Advances in X-ray Phase Imaging**. *Japanese Journal of Applied Physics*, **44**(9A):6355–6367, sep 2005. 48

[19] C. David, B. Nöhammer, H. H. Solak, and E. Ziegler. **Differential x-ray phase contrast imaging using a shearing interferometer**. *Applied Physics Letters*, **81**(17):3287–3289, 2002. 49, 51

[20] A. Momose, S. Kawamoto, I. Koyama, Y. Hamaishi, K. Takai, and Y. Suzuki. **Demonstration of X-Ray Talbot Interferometry**. *Japanese Journal of Applied Physics*, **42**(Part 2, No. 7B):L866–L868, jul 2003. 49

[21] H.F. Talbot Esq. F.R.S. **LXXVI. Facts relating to optical science. No. IV**. *The London, Edinburgh, and Dublin Philosophical Magazine and Journal of Science*, **9**(56):401–407, 1836. 49

[22] T. J. Suleski. **Generation of Lohmann images from binary-phase Talbot array illuminators**. *Appl. Opt.*, **36**(20):4686–4691, Jul 1997. 49

[23] F. Pfeiffer, T. Weitkamp, O. Bunk, and C. David. **Phase retrieval and differential phase-contrast imaging with low-brilliance X-ray sources**. *Nature Physics*, **2**(4):258–261, 2006. 51

[24] T. Weitkamp, A. Diaz, C. David, F. Pfeiffer, M. Stampanoni, P. Cloetens, and E. Ziegler. **X-ray phase imaging with a grating interferometer**. *Opt. Express*, **13**(16):6296–6304, Aug 2005. 51

[25] M. Engelhardt, C. Kottler, O. Bunk, C. David, C. Schroer, J. Baumann, M. Schuster, and F. Pfeiffer. **The fractional Talbot effect in differential x-ray phase-contrast imaging for extended and polychromatic x-ray sources**. *Journal of Microscopy*, **232**(1):145–157, 2008. 51

[26] T. Thüring, M. Abis, Z. Wang, C. David, and M. Stampanoni. **X-ray phase-contrast imaging at 100 keV on a conventional source**. *Scientific reports*, **4**:5198, 06 2014. 51

[27] D. Chapman, W. Thomlinson, R. E. Johnston, D. Washburn, E. Pisano, N. Gmür, Z. Zhong, R. Menk, F. Arfelli, and D. Sayers. **Diffraction enhanced x-ray imaging**. *Physics in Medicine and Biology*, **42**(11):2015–2025, nov 1997. 53

[28] A. Olivo, F. Arfelli, G. Cantatore, R. Longo, R. H. Menk, S. Pani, M. Prest, P. Poropat, L. Rigon, G. Tromba, E. Vallazza, and E. Castelli. **An innovative digital imaging set-up allowing a low-dose approach to phase contrast applications in the medical field**. *Medical Physics*, **28**(8):1610, 2001. 54

[29] A. Olivo and R. D. Speller. **A coded-aperture technique allowing x-ray phase contrast imaging with conventional sources**. *Applied Physics Letters*, **91**(7), 2007. 55

[30] A. Olivo and R. D. Speller. **Modelling of a novel x-ray phase contrast imaging technique based on coded apertures.** *Physics in medicine and biology*, **52**(22):6555–73, 2007. 55, 58

[31] P. C. Diemoz, M. Endrizzi, C. E. Zapata, A. Bravin, R. D. Speller, I. K. Robinson, and A. Olivo. **Improved sensitivity at synchrotrons using edge illumination X-ray phase-contrast imaging**. *Journal of Instrumentation*, **8**(06):C06002–C06002, jun 2013. 55

[32] P. R. T. Munro, K. Ignatyev, R. D. Speller, and A. Olivo. **Phase and absorption retrieval using incoherent X-ray sources**. *Proceedings of the National Academy of Sciences*, **109**(35):13922–13927, 2012. 56

[33] M. Endrizzi, P. C. Diemoz, T. P. Millard, J. Louise Jones, R. D. Speller, I. K. Robinson, and A. Olivo. **Hard X-ray dark-field imaging with incoherent sample illumination**. *Applied Physics Letters*, **104**(2):3–6, 2014. 57, 77, 81

[34] P. C. Diemoz, F. A. Vittoria, and A. Olivo. **Spatial resolution of edge illumination X-ray phase-contrast imaging**. *Opt. Express*, **22**(13):15514–15529, Jun 2014. 57

[35] A. Olivo, K. Ignatyev, P. Munro, and R. D. Speller. **A coded-aperture based method allowing non-interferometric phase contrast imaging with incoherent X-ray sources**. *Nuclear Instruments and Methods in Physics Research Section A: Accelerators, Spectrometers, Detectors and Associated Equipment*, **648**:S28S31, 08 2011. 57

[36] P. C. Diemoz and A. Olivo. **On the origin of contrast in edge illumination X-ray phase-contrast imaging.** *Optics express*, **22**(23):28199–214, 2014. 57

[37] K. Ignatyev, P. R. T. Munro, D. Chana, R. D. Speller, and A. Olivo. **Coded apertures allow high-energy x-ray phase contrast imaging with laboratory sources**. *Journal of Applied Physics*, **110**(1):1–8, 2011. 57

[38] M. Endrizzi, F. A. Vittoria, G. Kallon, D. Basta, P. C. Diemoz, A. Vincenzi, P. Delogu, R. Bellazzini, and A. Olivo. **Achromatic approach to phase-based multi-modal imaging with conventional X-ray sources**. *Optics Express*, **23**(12):16473, 2015. 57

[39] P. C. Diemoz, C. K. Hagen, M. Endrizzi, and A. Olivo. **Sensitivity of laboratory based implementations of edge illumination X-ray phase-contrast imaging**. *Applied Physics Letters*, **103**(24):244104, 2013. 57

[40] A. Olivo, S. Gkoumas, M. Endrizzi, C. K. Hagen, M. B. Szafraniec, P. C. Diemoz, P. R. T. Munro, K. Ignatyev, B. Johnson, J. A. Horrocks, S. J. Vinnicombe, J. L. Jones, and R. D. Speller. **Low-dose phase contrast mammography with conventional x-ray sources**. *Medical Physics*, **40**(9):090701, 2013. 58

[41] D. Basta, M. Endrizzi, F. Vittoria, A. Astolfo, and A. Olivo. **Compact and cost effective lab-based edge-illumination X-ray phase contrast**

imaging with a structured focal spot. *Applied Physics Letters*, **108**, 06 2016. 59

[42] G. K. Kallon, M. Wesolowski, F. A. Vittoria, M. Endrizzi, D. Basta, T. P. Millard, P. C. Diemoz, and A. Olivo. **A laboratory based edge-illumination x-ray phase-contrast imaging setup with two-directional sensitivity**. *Applied Physics Letters*, **107**(20), 2015. 59

[43] G. K. Kallon, P. C. Diemoz, F. A. Vittoria, D. Basta, M. Endrizzi, and A. Olivo. **Comparing signal intensity and refraction sensitivity of double and single mask edge illumination lab-based x-ray phase contrast imaging set-ups**. *Journal of Physics D: Applied Physics*, **50**(41):415401, sep 2017. 59

[44] F. A. Vittoria, G. K. N. Kallon, D. Basta, P. C. Diemoz, I. K. Robinson, A. Olivo, and M. Endrizzi. **Beam tracking approach for single shot retrieval of absorption, refraction, and dark field signals with laboratory xray sources**. *Applied Physics Letters*, **106**(22):224102, 2015. 60

[45] A. Astolfo, M. Endrizzi, F. A. Vittoria, Diemoz, P. C., B. Price, I. Haig, and A. Olivo. **Large field of view, fast and low dose multimodal phase-contrast imaging at high x-ray energy**. *Scientific Reports*, **7**, 2017. 61

[46] C. K. Hagen, P. C. Diemoz, M. Endrizzi, L. Rigon, D. Dreossi, F. Arfelli, F. C. M. Lopez, R. Longo, and A. Olivo. **Theory and preliminary experimental verification of quantitative edge illumination x-ray phase contrast tomography**. *Opt. Express*, **22**(7):7989–8000, Apr 2014. 61

[47] C. K. Hagen, P. R. T. Munro, M. Endrizzi, P. C. Diemoz, and A. Olivo. **Low-dose phase contrast tomography with conventional x-ray sources**. *Medical Physics*, **41**(7):070701, 2014. 61

[48] A. Zamir, O. J. Arthurs, C. K. Hagen, P. C. Diemoz, T. Brochard, A. Bravin, N. J. Sebire, and A. Olivo. **X-ray phase contrast tomography;**

proof of principle for post-mortem imaging. *The British Journal of Radiology*, **89**(1058):20150565, 2016. 61

[49] R. F. Mould. **The early history of X-ray diagnosis with emphasis on the contributions of physics 1895-1915**. *Physics in Medicine and Biology*, **40**(11):1741, 1995. 62

[50] T. S. Curry, J. E. Dowdey, and R. C. Jr Murray. *Christensen's physics of diagnostic radiology 4th edition*. Lea and Febiger, United States, 1990. 62

[51] P. Allé, E. Wenger, S. Dahaoui, D. Schaniel, and C. Lecomte. **Comparison of CCD, CMOS and Hybrid Pixel x-ray detectors: detection principle and data quality**. *Physica Scripta*, **91**(6):063001, may 2016. 62

[52] E. Samei. **Advances in Digital Radiography, Performance of Digital Radiographic Detectors: Factors Affecting Sharpness and Noise**. *Radiological Society of North America (RSNA),, Oak Brook, IL*, 2003. 62

[53] G. P. Weckler. **Operation of p-n Junction Photodetectors in a Photon Flux Integrating Mode**. *IEEE Journal of Solid-State Circuits*, **2**(3):65–73, 1967. 64

[54] L. E. Antonuk, J. M. Boudry, C. Kim, M. Longo, E. J. Morton, J. Yorkston, and R. A. Street. **Signal, noise, and readout considerations in the development of amorphous silicon photodiode arrays for radiotherapy and diagnostic x-ray imaging**. **1443**, pages 108–119, 1991. 64

[55] W. Zhao and J. A. Rowlands. **X-ray imaging using amorphous selenium: Feasibility of a flat panel self-scanned detector for digital radiology**. *Medical Physics*, **22**(10):1595–1604, 1995. 64

[56] F. A. Vittoria, P. C. Diemoz, M. Endrizzi, L. Rigon, F. C. Lopez, D. Dreossi, P. R. T. Munro, and A. Olivo. **Strategies for efficient and fast wave optics simulation of coded-aperture and other x-ray phase-contrast imaging methods**. *Applied optics*, **52**:6940–6947, 2013. 67, 102

[57] P. Meyer and J. Schulz. **Chapter 16 - Deep X-ray Lithography**. In *Micromanufacturing Engineering and Technology (Second Edition)*, Micro and Nano Technologies, pages 365 – 391. William Andrew Publishing, Boston, second edition edition, 2015. 73

[58] P. Meyer, F. An, and J. Schulz. **X-ray gratings for grating-based x-ray DPCI fabricated using the deep x-ray lithography process: state of the art**. 2017. 73

[59] N. N. Le, T. C. Hue Phan, A. D. Le, T. M. Dung Dang, and M. C. Dang. **Optimization of copper electroplating process applied for microfabrication on flexible polyethylene terephthalate substrate**. *Advances in Natural Sciences: Nanoscience and Nanotechnology*, **6**(3):035007, 2015. 76

[60] T. P. Millard, M. Endrizzi, N. Everdell, L. Rigon, F. Arfelli, R. H. Menk, E. Stride, and A. Olivo. **Evaluation of microbubble contrast agents for dynamic imaging with x-ray phase contrast**. *Scientific Reports*, **5**, 2015. 77, 80

[61] P. C. Diemoz, F. A. Vittoria, C. K. Hagen, M. Endrizzi, P. Coan, E. Brun, U. H. Wagner, C. Rau, I. K. Robinson, A. Bravin, and A. Olivo. **Single-image phase retrieval using an edge illumination X-ray phase-contrast imaging setup**. *Journal of Synchrotron Radiation*, **22**:1072–1077, 2015. 77

[62] F. Pfeiffer, M. Bech, O. Bunk, P. Kraft, E. F. Eikenberry, Ch. Brönnimann, C. Grünzweig, and C. David. **Hard-X-ray dark-field imaging using a grating interferometer**. *Nature Materials*, **7**(2):134–137, 2008. 77

[63] H. H. Wen, E. E. Bennett, R. Kopace, A. F. Stein, and V. Pai. **Single-shot x-ray differential phase-contrast and diffraction imaging using two-dimensional transmission gratings**. *Opt. Lett.*, **35**(12):1932–1934, 2010. 77

[64] K. S. Morgan, P. Modregger, S. C. Irvine, S. Rutishauser, V. A. Guzenko, M. Stampanoni, and C. David. **A sensitive x-ray phase con-**

trast technique for rapid imaging using a single phase grid analyzer. *Opt. Lett.*, **38**(22):4605–4608, 2013. 77

[65] I. Zanette, T. Zhou, A. Burvall, U. Lundström, D. H. Larsson, M. Zdora, P. Thibault, F. Pfeiffer, and H. M. Hertz. **Speckle-Based X-Ray Phase-Contrast and Dark-Field Imaging with a Laboratory Source**. *Phys. Rev. Lett.*, **112**:253903, 2014. 77

[66] M. Stampanoni, F. Marone, P. Modregger, B. Pinzer, T. Thüring, J. Vi-laComamala, C. David, and R. Mokso. **Tomographic Hard Xray Phase Contrast Micro and Nanoimaging at TOMCAT**. *AIP Conference Proceedings*, **1266**(1):13–17, 2010. 77

[67] Paul Claude Diemoz, Paola Coan, Christian Glaser, and Alberto Bravin. **Absorption, refraction and scattering in analyzer-based imaging: comparison of different algorithms**. *Opt. Express*, **18**(4):3494–3509, Feb 2010. 77

[68] P. C. Diemoz, A. Bravin, and P. Coan. **Theoretical comparison of three X-ray phase-contrast imaging techniques: Propagation-based imaging, analyzer-based imaging and grating interferometry**. *Optics express*, **20**:2789–805, 01 2012. 77

[69] P. Suortti, S. Fiedler, A. Bravin, T. Brochard, M. Mattenet, M. Renier, P. Spanne, W. Thomlinson, A. M. Charvet, H. Elleaume, C. Schulze-Briese, and A. C. Thompson. **Fixed-exit monochromator for computed tomography with synchrotron radiation at energies 18–90keV**. *Journal of Synchrotron Radiation*, **7**(5):340–347, Sep 2000. 78

[70] A. Mittone, I. Manakov, L. Broche, C. Jarnias, P. Coan, and A. Bravin. **Characterization of a sCMOS-based high-resolution imaging system**. *Journal of Synchrotron Radiation*, **24**(6):1226–1236, Nov 2017. 78

[71] A. Mittone, F. Baldacci, A. Bravin, E. Brun, F. Delaire, C. Ferrero, S. Gasilov, N. Freud, J. Létang, D. Sarrut, F. Smekens, and P. Coan.

An efficient numerical tool for dose deposition prediction applied to synchrotron medical imaging and radiation therapy. *Journal of Synchrotron Radiation*, **20**(5):785–792, Sep 2013. 80

[72] P. Modregger, M. Kagias, S. C. Irvine, R. Brönnimann, K. Jefimovs, M. Endrizzi, and A. Olivo. **Interpretation and Utility of the Moments of Small-Angle X-Ray Scattering Distributions**. *Physical review letters*, **118**(26):265501–265501, Jun 2017. 82

[73] E. Knudsen, A. Prodi, J. Baltser, M. Thomsen, P. Willendrup, M. Sánchez del Ro, C. Ferrero, E. Farhi, K. Haldrup, A. Vickery, R. Feidenhans'l, K. Mortensen, M. Nielsen, H.F. Poulsen, S. Schmidt, and K. Lefmann. **McXtrace: A Monte Carlo software package for simulating X-ray optics, beamlines and experiments**. *Journal of Applied Crystallography*, **46**:679–696, 2013. 83

[74] T. P. Millard, M. Endrizzi, P. C. Diemoz, C. K. Hagen, and A. Olivo. **Monte Carlo model of a polychromatic laboratory based edge illumination x-ray phase contrast system**. *Review of Scientific Instruments*, **85**(5), 2014. 83, 138

[75] T. Schoonjans, A. Brunetti, B. Golosio, M. Sanchez Del Rio, V. A. Solé, C. Ferrero, and L. Vincze. **The xraylib library for X-ray-matter interactions. Recent developments**. *Spectrochimica Acta - Part B Atomic Spectroscopy*, **66**(11-12):776–784, 2011. 85

[76] A. Olivo, F. Arfelli, D. Dreossi, R. Longo, R. H. Menk, S. Pani, P. Poropat, L. Rigon, F. Zanconati, and E. Castelli. **Preliminary study on extremely small angle x-ray scatter imaging with synchrotron radiation**. *Physics in Medicine & Biology*, **47**(3):469, 2002. 88

[77] C. Martin. **The importance of radiation quality for optimisation in radiology**. *Biomedical imaging and intervention journal*, **3**:e38, 04 2007. 95

[78] P. Brosi, A. Stüssi Lobmaier, F. Verdun, P. Vock, and R. Wolf. **Copper filtration in pediatric digital X-ray imaging: Its impact on image quality and dose**. *Radiological physics and technology*, **4**:148–55, 03 2011. 95

[79] A. M. Hernandez and J. M. Boone. **Tungsten anode spectral model using interpolating cubic splines: unfiltered x-ray spectra from 20 kV to 640 kV.** *Medical physics*, **41**(4):042101, 2014. 102

[80] T. P. Millard, M. Endrizzi, L. Rigon, F. Arfelli, R. H. Menk, J. Owen, E. Stride, and A. Olivo. **Quantification of microbubble concentration through x-ray phase contrast imaging**. *Applied Physics Letters*, **103**(11), 2013. 112, 160, 168

[81] Z. H. Levine, A. P. Peskin, E. J. Garboczi, and A. D. Holmgren. **Multi-Energy X-Ray Tomography of an Optical Fiber: The Role of Spatial Averaging**. *Microscopy and microanalysis : the official journal of Microscopy Society of America, Microbeam Analysis Society, Microscopical Society of Canada*, **25**(1):70–76, Feb 2019. 118

[82] C. Fedon, C. Rabin, M. Caballo, O. Diaz, E. García, A. Rodríguez-Ruiz, G. A. González-Sprinberg, and I. Sechopoulos. **Monte Carlo study on optimal breast voxel resolution for dosimetry estimates in digital breast tomosynthesis**. *Physics in Medicine & Biology*, **64**(1):015003, dec 2018. 118

[83] A. Vincenzi, P.L. de Ruvo, P. Delogu, R. Bellazzini, A. Brez, M. Minuti, M. Pinchera, and G. Spandre. **Energy characterization of Pixirad-1 photon counting detector system**. *Journal of Instrumentation*, **10**(04):C04010–C04010, apr 2015. 143

[84] K. Iniewski, H. Chen, G. Bindley, I. Kuvvetli, and C. budtz jNørgensen. **Modeling charge-sharing effects in pixellated CZT detectors**. **6**, pages 4608 – 4611, 01 2007. 144

[85] A. Erko, V. Arkadiev, A. Bjeoumikhov, A. Antonov, B. Beckhoff, I. Grigorieva, habil. B. Kanngiesser, and B. Vidal. *X-Ray Optics*, pages 85–198. Springer Berlin Heidelberg, Berlin, Heidelberg, 2006. 152

[86] M. Busi, U. L. Olsen, E. B. Knudsen, J. R. Frisvad, J. Kehres, E. S. Dreier, M. Khalil, and K. Haldrup. **Simulation tools for scattering corrections in spectrally resolved x-ray computed tomography using McXtrace**. *Optical Engineering*, **57**(3):1 – 10, 2018. 153

[87] Mehrdad S. Beni, D. Krstic, D. Nikezic, and K. N. Yu. **Monte Carlo studies on photon interactions in radiobiological experiments**. *PLOS ONE*, **13**(3):1–24, 03 2018. 155

[88] K. S. Morgan, K. K. W. Siu, and D. M. Paganin. **The projection approximation and edge contrast for x-ray propagation-based phase contrast imaging of a cylindrical edge**. *Opt. Express*, **18**(10):9865–9878, May 2010. 158

[89] P. R. T. Munro. **Rigorous multi-slice wave optical simulation of x-ray propagation in inhomogeneous space**. *J. Opt. Soc. Am. A*, **36**(7):1197–1208, Jul 2019. 158

[90] A. Malecki, G. Potdevin, and F. Pfeiffer. **Quantitative wave-optical numerical analysis of the dark-field signal in grating-based X-ray interferometry**. *EPL (Europhysics Letters)*, **99**(4):48001, aug 2012. 160

[91] C. Maughan Jones, F. A. Vittoria, A. Olivo, M. Endrizzi, and P. R. T. Munro. **Retrieval of weak x-ray scattering using edge illumination**. *Opt. Lett.*, **43**(16):3874–3877, Aug 2018. 161